ABSTRACT

Title of Dissertation:	BURNING EMULATIONS OF CONDENSED PHASE FUELS ABOARD THE INTERNATIONAL SPACE STATION
	Parham Dehghani, Doctor of Philosophy, 2022
Dissertation directed by:	Professor Peter B. Sunderland, and Professor James G. Quintiere Department of Fire Protection Engineering

Little is known about the fire hazards of solids and liquids in microgravity. Ground-based tests are too short to overcome ignition transients and testing dozens of condensed fuels in orbit is prohibitively expensive. Burning rate emulation is one way to address this gap. It involves emulating condensed fuels with gases using a porous burner with embedded heat flux gages. This is a study of microgravity burning rate emulation aboard the International Space Station. The burner had porous round surfaces with diameter of 25 mm. The fuel mixture was gaseous ethylene, and it was diluted with various amounts of nitrogen. The resulting heats of combustion were 15 – 47.2 kJ/g. The flow rate, oxygen concentration in the ambient, and pressure were varied. Heat flux to the burner was measured with two embedded heat flux gages and a slug calorimeter. The effective heat of gasification was determined from the heat flux divided by the fuel flow rate. Radiometers provided the radiative loss fractions. A dimensional analysis based on radiation theory yielded a relationship for radiative loss fraction. RADCAL, a narrow-band radiation model,

yielded flame emissivities from the product concentrations, temperature, flame length, and pressure. Previously published analytical solutions to these flames allowed prediction of flame heights and radius, and when combined with the radiation empirical relationship led to corrections of total heat release rate from the flames due to radiative loss. Average convective and radiative heat flux were obtained from the analytical solution and a model based on the geometrical view factor of the burner surface with respect to the flame sheet, that were used to calculate heats of gasification. All flames burning in 21% by volume oxygen self-extinguished within 40 s. However, steady flames were observed at 26.5, 34, and 40% oxygen. The analytical solution was used to quantify flame steadiness just before extinction. The steadiest flames reached more than 94% of their steady-state heat fluxes and heights. A flammability map as a plot of heat of gasification versus heat of combustion was developed based on the measurement and theory for nominal ambient oxygen mole fractions of 0.265, 0.34, and 0.4.

BURNING EMULATIONS OF CONDENSED PHASE FUELS ABOARD THE INTERNATIONAL SPACE STATION

by

Parham Dehghani

Dissertation submitted to the Faculty of the Graduate School of the
University of Maryland, College Park, in partial fulfillment
of the requirements for the degree of
Doctor of Philosophy
2022

Advisory Committee:
Professor Peter B. Sunderland, Chair
Professor James G. Quintiere, Co-chair
Professor Christopher P. Cadou
Dr. John L. de Ris
Professor Reinhard Radermacher
Professor Arnaud Trouve

Dedication

This thesis is dedicated firstly to the love of my life, "*Roza*" for her support and love! To my mother and brother for being always helpful and supportive, to my father for teaching me how to live. I am grateful to the kind support of my entire family and friends specially, my father-in-law, mother-in-law, brother-in-law, my uncles, and aunts, and Jessi. I also give my special thanks to my senior friends Mr. Samsum Kashfi, and Pari S. Kashfi for their kind support.

No words can describe the love I have deep in my heart for my two adorable cats: Kopol and Lucy.

And . . . COVID-19; although it caused us so many hardships, it gave me the opportunity to re-unite with my family.

Acknowledgements

I wish to thank my academic advisors, Prof. Peter B. Sunderland, and Prof. James G. Quintiere for kindly helping and guiding me to pursue my ambitions I am also grateful to the members of my dissertation committee: Drs. Chris Cadou., John L deRis, Peter.B. Sunderland, Reinhard Radermacher, and Jame Quintiere for generously offering their time, support, guidance, and good will. Learning from Prof. Quintiere, Prof. Sunderland, and Dr. deRis was a "*once in a lifetime"* experience. Discussions with Dr. H.R. Baum (especially his rendition of the original diffusion flame solution), D. P. Stocker, and Prof. A. Snegirev are greatly appreciated. I appreciate the time, and support of my other committee members for my dissertation proposal defense, Prof. Stanislav Stoliarov, and Prof. Bao Yang.

This investigation is funded by NASA's ISS Research Program through agreement 80NSSC20M0119. I am also grateful to the NASA engineering and operations teams, especially Angela Adams, Operations Lead; Melani Smajdek, Planning Lead; Dennis Stocker, Project Scientist; and Uday Hegde, Deputy Project Scientist.

I am Thankful to the University of Maryland's, Clark's Foundation that recognized me as a Clark's Doctoral Fellow, and to the UMD, Mechanical Engineering dept. for granting me the Dean's fellowship for the Spring 2022. I also appreciate the travel fundings granted by the National Science Foundation (NSF), the Combustion Institute, the Clark's Fellowship Program, and the UMD Graduate School that covered part of my expenses for attending and presenting at conferences. Some of the flame photograph sequences are from the compilations by Aviv Kalai.

Table of Contents

List of Figures

List of Tables

List of Abbreviations

A	Surface area
b	Copper plate diameter measured at its half thickness
B	Spalding B number
c	Specific heat
c_p	Gas specific heat
D_∞	Ambient mass diffusivity
d_f	Radiometer distance to the flame volume centroid
d_n	Radiometer distance to the intersecting point between normal axis to the burner and radiometer surface
d_s	Radiometer distance to the center of the burner surface
e_b	Thermal effusivity
$F_{s\to r}$	View factor of the burner surface with respect to the radiometer
$F_{f\to s}$	AAA
$F_{s\to f}$	View factor of the flame sheet with respect to the burner surface
FT	Fuel Terminated
H	Thickness of the copper plate
h	The vertical distance from the burner surface to the radiometer elevation
h_0	effective heat transfer coefficient between semi-infinite back and plate
h_{rod}	effective heat transfer coefficient between the sensor rod and plate
K	Gas conversion factor
k	Thermal conductivity
L	Heat of gasification
$(mc)_{Cu}$	heat capacity of copper
$\dot{M}$	Total mass flow rate
$\dot{m}$	Mass flow rate
$\dot{m}''$	Mass flux
p	Ambient pressure
Pe_c	Peclet number
$\dot{Q}$	Heat loss rate
$\dot{q}''$	Heat flux
R	Burner surface radius
r	Radial location on the burner surface
r_f	Radius of the flame measured at its base
SE	Self-Extinguished
S	Stoichiometric molar air-fuel ratio
T	Temperature
t	time
t_b	burn-time
V	Sensor output voltage, and Volumetric flow rate
X	Mole fraction
X_r	Radiant fraction
x	vertical distance from burner center
Y	Mass fraction
Y_{Fb}	Fuel mass fraction at the burner surface

y_f Flame height
Z Mixture fraction

Greek

α Absorptivity or Fuel-ambient air mass ratio
β Radiative heat flux to the top surface divided by radiative heat flux to the Bevel edge of the burner
Δh_c Enthalpy of combustion
ϵ Emissivity
θ_f The angle between radiometer normal axis and radiometer-flame centroid line
θ_r Burner surface and radiometer connecting line angle WRT horizontal
κ Absorption coefficient
$\tilde{\kappa}$ Effective absorption coeficient
λ Dimensionless mass flux = $\frac{\dot{m}''}{\frac{4k}{\pi c_p R_b}}$
μ Radiative heat flux divided by convective heat flux to the top surface of the burner
ξ Ellipsoidal coordinate
ξ_f Ellipsoidal coordinate at flame sheet
ρ Density
σ Stephan-Boltzmann constant
τ Dimensionless time = $\frac{D_\infty t}{R^2}$
Ω Dimensionless radiation fraction variable

Subscripts

60	+60 radiometer
b	Back of the copper plate
$CO2$	Carbon-dioxide
c	Convective heat flux
cal	Average heat flux to the burner surface (Calorimeter)
crc	Corrected calorimeter
ctr	Center of the burner surface
$convection$	Convective heat flux
ext	external
f	flame sheet or fuel
g	Burner gas or combustion products gas
H	Heat flux sensors
$H2O$	Water vapor
mix	Fuel mixture
o	Without radiation loss
$O2$	Oxygen
off	Offset position on burner surface ($r = 9.5$ mm)
pr	predicted
r	Radiation
rr	re-radiation
rod	Heat flux sensor rod

s	Burner surface
st	Steady state
$sensor$	Heat flux sensor
∞	Ambient
$\in = 0$	Ellipsoid aspect ratio at the burner surface

1. Introduction

1.1 Motivation

Human-crew space missions presented the possibility of many hazards, notably fires. A significant amount of research has been carried out on the characteristics of fire in normal gravity. However, it has been observed that the behavior of microgravity fires might be quite different. Some experiments have suggested that it might be easier to burn condensed phase fuels in microgravity. This highlights the need for an in-depth analysis of condensed fuel flames in quiescent artificial atmosphere in microgravity condition i.e., aboard the International Space Station (ISS).

The recent urgency in fire control and safety is due to a fire on the Russian Mir space shuttle where an oxygen generator caused the blaze [1–3]. It was later found that the fire probably extinguished due to the depletion of oxygen supply. This sustained fire is a cause of concern, and the scenario calls for precautionary and preventive measures. To prevent a fire from starting in a spacecraft, it is necessary to study the conditions of flame development. The logical starting point is the case of a laminar diffusion flame in a quiescent environment.

There are a number of variables that alter the way a fire spreads in a space vehicle. The effect of buoyancy is seen on Earth as the surrounding air is entrained in by convection which gives the flame an upward pointed shape. The negligible buoyancy in microgravity causes the flames to have a more hemispherical or bubble-like shape. The presence of forced convection, which aides in the spread of fire, comes from the ventilation in the spacecraft. The hemispherical shape of the diffusion flame also affects the soot behavior and the release of gases, which in turn affects the radiation losses from the flame.

The flammability of various materials being transported into space is assessed through a series of normal gravity tests designed by NASA [4]. These tests aren’t sufficient to lay out the

characteristics of a flame in reduced gravity conditions [1]. The burning of numerous fuels has been tested in microgravity conditions and it is well documented [5–9]. The ideal scenario is to perform routine burn tests aboard the International Space Station (ISS) of potential materials, but this is not practical.

In the proposed study, an innovative technique is suggested to study the burning of condensed phase fuels. A gaseous burner known as the Burning Rate Emulator (BRE) has been developed to emulate the characteristics of a condensed fuel flame in a quiescent atmosphere. This emulation is theoretically achieved by matching four characteristic properties: heat of gasification, heat of combustion, surface temperature and smoke point for the same burner flow rate. BRE burner can provide a practical method to study the flammability of various materials aboard spacecraft.

1.2 Literature Review

Since the beginning of human aspirations for space flight, concerns and incidents have made the possibility of fire hazard a real concern [1–3]. Yet over the past decades, we still have limited knowledge of the full extent of fires in microgravity [4,10]. Extensive studies have been made on very small materials and burners, but these usually include flames with assisted ambient flows. We have long known that materials can burn in-place and spread by ambient flow with sufficient oxygen in all gravity conditions [6–9,11–30]. While spacecraft will have movement in its atmosphere, it is small and random. In microgravity, opposed flow flame spread provides its own flow in a quiescent atmosphere [18,26–28,31–33]. What has been deficient is the understanding of burning in-place on a surface in a quiescent atmosphere [10]. Anecdotal early Kimzey experiments showed that small items of plastics could burn, and controlled experiments of a candlewick flame could sustain burning for about an hour in microgravity [34,35]. Also, we have learned that liquid droplets can burn quasi-steadily, and steady burning theory is reasonably predictive although, the onset of cool flames can augment the burning[36–43].

Fire growth is a combination of three distinct processes: (1) ignition, (2) burning in-place, and (3) spread. In microgravity, we have a good understanding of opposed flow flame spread, and our knowledge of concurrent spread is also in good shape, as we have a good understanding of how items burn with a specified ambient flow. Ignition can also be adequately understood in microgravity given an insulting heat flux. In normal gravity, ignition time is reasonably predicted by theory that even neglects heat loss, so the process only depends on heat flux and material properties. The current study began based on the premise that material properties can be defined for fire growth computations, and they can be measured. Indeed, the NASA designated Test 2 is the Cone Calorimeter that allows for these property measurements. The NASA Test 1 [44], in regulatory use, considers the measure of upward spread in 1-g and at higher than normal oxygen mole fractions as the defining safety criterion for material use in spacecraft. Our work is aimed at employing Test 2 [45] with a procedure for measuring properties in conjunction with the theoretical prediction of burning in microgravity.

The current study was begun some years ago to investigate efficiently the possible burning of simulated flat surfaces using a burner [10,46–49]. The burner gases allow ease of ignition and the setting of a steady flow rate. It has been also learned that even starting with a steady flow rate, the corresponding flame in microgravity grows for some time before an apparent steady state is perceived. Early drop facility microgravity experiments for 5-second duration suggested steady flame heat flux might occur within that time, but the flame continued to grow [10]. It was suspected that the blue flames seen would increase radiation loss as they grew and lead to radiation extinction.

Our experiments in this document are all transient. But if a steady state is achieved, the data can be interpreted to represent a real material burning. The burner allows control of a fuel mixture that defines the heat of combustion per mixture mass (i.e., ethylene diluted with nitrogen can provide a range of heats of combustions up to 47.2 kJ/g which is the case of pure fuel). A measurement of the flame heat flux back to the burner allows computation of the heat of gasification, a key property appropriate to steady burning for an evaporative material. Even with

more complex pyrolysis and charring, an evaporative model leads to good estimates of time average burning in transient cases. The surface temperature of the burner relates to the material vaporization temperature, but this is a weak dependent parameter on the burning process, as it does not significantly affect ignition, and its associated radiative heat flux is usually relatively small compared to flame heat fluxes. We have hypothesized that the heats of combustion and gasification, both material properties, are key to defining flammability but as flame radiation is known to be significant in normal Earth gravity, we have added the smoke point. With these three parameters, our work has shown successful emulation of plastics and liquid pool fires of 25 and 50-mm diameters [4,10,46–54]. In microgravity radiation from soot does not appear to be important, but the fuel's products of water and carbon dioxide, as well as the fuel itself should be important for radiation. In short, the problem is to obtain the experimental flammability map (heats of gasification vs. fuel mixture mass flux, and eventually vs. heat of combustion) that allows obtaining the heat of combustion and heat of gasification to match with those of real materials [51,55,56].

Numerical simulations for 5 tests conducted at normal atmosphere was able to successfully predict, heat flux, flame existence duration, flame size and radiative heat loss. All these tests led to some instabilities, flame oscillation before self-extinguishment. Description of the extinction process including instabilities, was another the key achievements of this study [50,57]. The steady growth of a flame with mass flux of 3.09 g/m^{2}s (X_f = 1) ignited in atmospheric condition was numerically simulated and compared with experiments (DRM22 mechanism, time instants and peak temperatures are indicated) shown in Fig. 1.1. In the plots of each simulation, the color scale corresponds to the net radiative emission, and the lines were the iso-contours of the volumetric

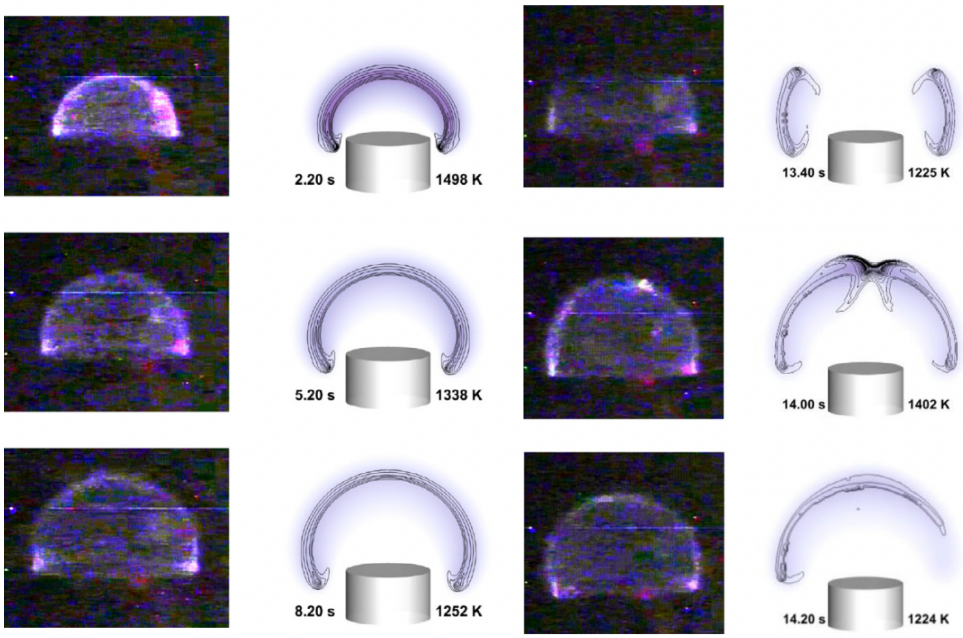

Figure 1.1. Numerical simulation of a flame ignited in atmospheric condition with mass flux of 3.09 g/m^{2}s (test 19039H2)

heat release rates 1, 2, 4, … MW/m^3. The first frame was taken 4.5 s after the igniter was retracted. Time increment between the frames (both experimental and numerical) is 3s. Spatial scale and location of the burner surface were also the same. The flame partial extinction and re-ignition (oscillations before self-extinction) was captured in the simulations. Analysis of transient dynamics of flame disintegration after the local extinction shows formation of the hook-like (bibrachial) structure of flame edge after the extinction onset. When the re-ignition occurs, a classical triple flame develops and propagates along the stoichiometric surface thereby recovering the original flame shape. The partial extinction-re-ignition was repeated for a number of times before the flame was self-extinguished completely.

The BRE experiments onboard the ISS allowed long duration flames in microgravity. The set of 122 ethylene mixture flames of ISS tests provided 49 flames that did not self-extinguish before the fuel flow was terminated intentionally. The constant fuel flow duration was set to 3 minutes for most of the cases and one flame was allowed to burn for 5 minutes. The surface heat flux and flame radiation measurements led to finding a correlation for *radiative heat loss fraction*

X_r. It will then be treated as lost energy and will be used to correct the heat of combustion used in the ellipsoidal model to analytically predict flame size, surface heat flux and steady state temperature. The other major finding was the flammability map that showed plastics can burn steadily in place in microgravity. The achievements of this study so far include analysis of the experimental results of round 1-ISS tests [50–52]. The major findings of this paper are correlation of radiative loss fraction with flame length, the flammability map and emulation of PMMA, and Nylon [51].

The steady data will be used to assess the predictive modeling. The experimental conditions range over mass fluxes from 1 to 12 g/m^{2}s, ethylene-nitrogen fuel mixtures of 15% and 100% ethylene, oxygen concentrations of 0.21 to 0.40, and pressures of 0.565 to 1 bar. The modeling is based on an analytic transient analysis developed with demonstrated numerical accuracy and good predictions with 5-s microgravity data. Here, that model will be modified by adjusting the heat of combustion, in that purely convective model, by its radiative heat loss. The flame radiative fraction is used to make this adjustment. It is shown that a model for the radiative fraction can be developed with dependence on an empirical constant. Given the radiative fraction, flame heat fluxes and flame temperature can be computed, while flame shape is independent of such. The flame temperature range of 1100 K to 1200 K with radiation loss will be used as a criterion for a stable flame or steady burning. The radiation code RADCAL is used to develop a model to predict flame emissivity and absorption coefficient. It is also shown that it is possible to predict the conditions for steady burning from known fuel properties, atmospheric conditions, and fuel diameter [52].

1.3 Objectives

A circular porous burner with gaseous fuel, called the Burning Rate Emulator (BRE), is developed to emulate the quiescent burning of condensed phase fuels. This
burner is based on the previous emulators that were used for normal gravity and the drop tower experiments [4,10,46–48,55,56]. The premise of the BRE technique is that the emulation is achieved by matching four properties of a diffusion flame, i.e., heat of combustion, heat of gasification, surface temperature and smoke point. The former two properties are of primary

significance while the other two are examined for normal gravity tests. The objectives of this study are as listed below.

- Characterize the burners before data gathering experiments to insure having a good understanding of the measurement techniques used onboard the ISS.
- Planning two rounds of microgravity tests to record data by changing different parameters, i.e., Fuel mixture mass flux, chamber ambient oxygen mole fraction, chamber pressure, fuel type and the burner size.
- Correlate the experimental results by employing relevant steady-state theory and analyze the burner as a condensed fuel emulator in microgravity to obtain the flammability map.
- Modify the slug calorimeter calibration constants [48] to account for the heat absorbed by the burner rim.
- Examine the dependency of the BRE slug calorimeter on the burn time.
- Convert all data recorded in each round of testing and analyze by segregation of data for identifying correlations.
- Modify the radiative fraction correlation, found by dimensional analysis, to account for several more independent factors, i.e., Chamber pressure and oxygen mole fraction. It requires a working knowledge of RADCAL[58,59] by Grosshandler, a narrow band model used for radiation calculation.
- Analyze flame temperature by utilizing ellipsoidal theory [49,60]
- Analyze and estimate the average emissivity associated with each flame.
- Obtaining a flammability map for microgravity condition to address fire safety of spacecrafts

1.4 Roadmap and Timeline for Completion of Dissertation

The first round of ISS tests preparation, data gathering, and data analysis led to publishing two journal papers and one other journal collaboration which are explained in sections 2-5.

The second round of ISS tests provided valuable set of data to analyzed. The remaining time until graduation is dedicated to objectives introduced in section 1.3. The new results will be

converted to engineering units. Average of the two measured heat fluxes are used to obtain heats of gasification. The radiative loss fraction is retrieved from radiometer's measured data and is defined as the ratio of total radiation loss rate to total heat release rate from the flame.

The ISS experiments provided enough data to publish the three journal papers, two presentations and one poster competition [50–54,60] as discussed in the literature review. Also, another paper has been accepted at the Proceeding of the Combustion Institute [60]. Another journal paper discussing the flammability map in microgravity is expected to be submitted.

2. Description of Experiments

The BRE experiments aboard the International Space Station (ISS) were conducted in the Combustion Integrated Rack (CIR) under the Advanced Combustion via Microgravity Experiments (ACME) program. Conducting the experiments required a collaboration between the UMD and NASA operations, and engineering team. The UMD team consisted of prominent faculty advisors (Dr. Quintiere, Dr. Sunderland, and Dr. de Ris), and students. The author of this thesis was the leading Ph. D. student for the BRE experiments aboard the ISS. Four undergraduate, and four graduate students collaborated with the analysis of this project under supervision of the faculty advisors and the leading student.

The NASA team was responsible for providing the experimental apparatus, sending the equipment to the ISS, and installation of the hardware required for each experiment. The experiments were performed automatically by using a software developed by NASA team. Some tasks required human interaction on the space station such as, changing the fuel and oxygen gas bottles, installation of burners and specific hardware required for each experiment. NASA team also supported the UMD team by reviewing, revising and providing information as needed.

The UMD team was responsible for:

1. Preprocessing of the experiments:
    a. Calibration of the heat flux sensors, radiometers, and slug calorimeter.
    b. Identifying the working conditions of the sensors, mass flow meters and burners to ensure successful ignition and data recording on the test point days
    c. Identifying design parameters and develop a test matrix that could provide enough data for the objectives of this study
    d. Submitting the test parameters sheet (Appendix D) to NASA operations team two business days before each test point day. The total number of parameters were 69 that included, volumetric flow rates of fuel and nitrogen, ambient conditions for each test, camera settings, igniter position, etc. The parameter sheet was effectively the test matrix for each test point day, but with significantly more detail that helped NASA operations team to run the tests on the test day.

2. There were two rounds of tests. Each round consisted of 8 test point days that took 12 hours per day. The NASA operations team was responsible for running the tests, record the imaging and non-imaging data, and uploading the data on a cloud-based drive. The UMD team was responsible for:
    a. Monitoring the tests and make changes to the parameters sheet as needed
    b. Performing an initial analysis of the data provided shortly after each test
3. Analysis of the data and publication

A gaseous fuel BRE burner, with top surface diameter of 25 mm, is used. The burner top surface is made of a perforated copper sheet with 125 holes with diameters of 1.2 mm. A ceramic flow straightener ensures uniform fuel mass over the surface. Figure 1 shows a photograph of the burner and a schematic of the burner top and two heat flux sensors.

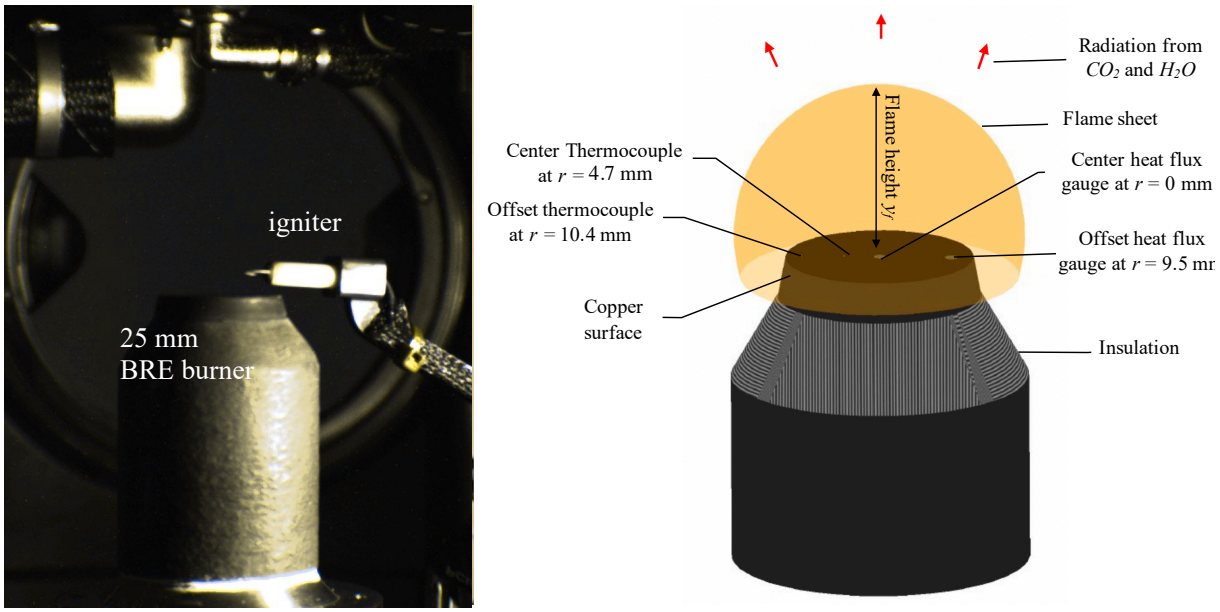

Figure 2.1 BRE burner image (left) and drawing (right).

2.1 Burner Surface Net Flame Heat Flux

Heat flux is measured locally by two Medtherm Schmidt-Boelter heat flux sensors flushed with the burner surface (at r = 0 and 9.5 mm) along with their surface temperatures, as they are not

water-cooled. The copper surface shown in Figure (2.1) schematic is designed to have a uniform temperature and to act as a calorimeter to measure the total average heat flux over the burner. (A fault in its design exposed the edges to the flame and caused significant uncertainty in directly measuring the heat flux over the projected burner face area. A correction procedure helped to improve this measurement.) Two K-type thermocouples located at r = 4.7 and 10.4 mm record the surface temperature of the copper top. The details of the burner surface and the location of the heat flux sensors and thermocouples are shown in Figure 2.1. The measurement objective is to obtain the average net heat flux to the burner surface from the calorimeter and the local sensor measurements.

The calorimeter was calibrated with a known radiant heat flux in the manner described previously by Markan et al [48]. The equation for its reduction to the net burner heat flux is given as in Eq. (2.1).

$$\dot{q}''_{cal} = \frac{\left[(m\,c)_{Cu} \left(\frac{dT_s}{dt} \right) + \epsilon\,\sigma\,A_s\,(T_s^4 - T_\infty^4) + h\,A_s\,(T_s - T_\infty) + \dot{Q}_g + \dot{Q}_{rod} + \dot{Q}_b \right]}{A_s} \quad (2.1)$$

Where the first three terms on the RHS represent absorbed by the copper plate, surface re-radiation, and free convection from copper plate (zero in micro-gravity). $A_s, A_{rod}\ and A_b$ are respectively, the burner face-area (573 mm^2), heat flux sensor side-wall area that transfers heat to the back of the burner (40 mm^2), and back-face of the copper plate (573 mm^2). $\dot{Q}_g\ , \dot{Q}_{rod}\ and \dot{Q}_b$ are heat absorbed by burner gaseous flow, heat conducted to the sensor rod (geometrical details shown in [48]), and heat transferred to the back of the burner face which are given by Eqns. (2.2 to 2.4).

$$\dot{Q}_g = \dot{m}_g\,c_g\,(T_s - T_b)\,, \quad (2.2)$$

$$\dot{Q}_{rod} = h_{rod}\,A_{rod}(T_s - T_{rod})\,, and \quad (2.3)$$

$$\dot{Q}_b = h_b\,A_b\,(T_s - T_b) \quad (2.4)$$

where T_b and h_b are back temperature calculated by Eq. (2.5), and heat transfer coefficient to the back of the copper surface. Equations (2.1 to 2.5) are derived in [49].

$$T_b = T_\infty + \frac{h_b}{e_b}\left[1.5\ (\ T_s - T_b\ ) \int_0^t (\ T_s - T_b\ )\ dt \right]^{0.5}. \tag{2.5}$$

h_b, h_{rod}, e_b and $(mc)_{Cu}$ are found by equating Eq. (2.1) to the average net heat flux which is determined by the two heat flux sensors during calibration of the calorimeter. The detailed calibration apparatus and procedure are described in [48]]. The root mean squared difference between RHS of Eq. (2.1) and known average heat flux is minimized by a commercial equation solver.; respectively found to be 386 W/m^2-K, 22 W/m^2-K, 5525 W-s$^{0.5}$/m^2-K, and 7.98 J/K. The $\dot{q}''_{cal}$ obtained here includes heat absorbed to the bevel edge of the top surface. That needs to be eliminated to account solely for the average absorbed face-area heat flux (see appendix A).

The two heat flux sensors are calibrated using a NIST standard [55,61]. The sensors have the original Medtherm paint while the copper burner top is painted with a more robust paint (Rustoleum). The sensor and copper painted surface emissivities were measured as unity and their corresponding absorptivities are 0.91 and 0.94 [61].

The desired net flux includes the radiation and convection from the flame minus the re-radiation of the burner surface. The corrections to the sensor heat flux have been derived previously and are presented in Eqns. (2.6, and 2.7) [10,46,47] .

$$\begin{aligned} \dot{q}''_{net} = \dot{q}''_{sensor} + (\ \alpha_s - \alpha_H\ )\ \dot{q}''_{f,r} - \epsilon_s\ \sigma\ (\ T_s^4 - T_\infty^4\ ) \\ + \epsilon_H\ \sigma\ (\ T_H^4 - T_\infty^4\ ) + h_b (\ T_H - T_s\ ) \end{aligned} \tag{2.6}$$

$$h_b = \left[\frac{\dot{q}''_{sensor} + \epsilon\ \sigma\ (\ T_H^4 - T_\infty^4\ )}{\dfrac{Y_{O2}\ \Delta h_{c,O2}}{c_p} - (\ T_H - T_\infty\ )} \right]. \tag{2.7}$$

The second term on the RHS contains the unknown incident flame radiation heat flux multiplied by the difference in absorptivities. It was to be eliminated by using the same paint on the sensor and burner, but that did not happen. The term is neglected in the equation, and it can be shown to be small accounting for less than 1% of the net heat flux as the $\dot{q}''_{f,r}$ ranges from 1.9 to 5.5 $\frac{kW}{m^2}$ and average absorbed heat flux ranges from 6.5 to 15.7 $\frac{kW}{m^2}$.

2.2 Flame Radiation

Several radiometers are oriented to view the burner flame and surface from distances of roughly 160 and 200 mm. The radiometers (Dexter Research Inc.) have a viewing window made of BaF_2 and the void volume between the sensing surface and the window is filled with argon [61]. The radiometers were calibrated by NASA using a black-body radiation source and varying temperature and aperture size. Two of the radiometers are used for radiation analysis and their calibration equations are $(0.00114V - 0.001481)W/cm^2$and $(0.001798V - 0.002307)W/cm^2$ [62,63]. There are two other radiometers available on BRE radiometer array, but for most of the cases their measured heat fluxes were out of range. The radiometers were used to determine the sensor normal radiant heat flux from both the flame and the burner. This could then be used to estimate the total radiation lost by the flame. The radiometry schematic is shown in Figure 2.

2.3 Fuel Mass Flux

The fuel nitrogen mixture mass flux simulates condensed phase burning. If the flame is steady, the net average flame heat flux divided by this mass flux gives the theoretical heat of gasification of the condensed phase burning material. The fuel mixture volumetric flow rate is measured by a Hastings instrument HFM-300 with maximum flow rate of 0.2 and 0.5 slpm nitrogen-based for low and high mass flux experiments respectively. The mass flow controllers are calibrated by nitrogen meaning that if other gases are used, an appropriate gas conversion factor must be used. The gas conversion factors used for these experiments are computed from Eqn. (2.9), and the volumetric flow rate of fuel mixture is calculated by using Eqn. (2.8) [64], where K_{N2} = 1, and $\dot{V}$represents volumetric flow rate.

$$\dot{V}_{mix} = \frac{K_{mix}}{K_{N2}} \dot{V}_{N2} \tag{2.8}$$

$$\frac{1}{K_{mix}} = \frac{X_f}{K_f} + \frac{1 - X_f}{K_{N_2}} \tag{2.9}$$

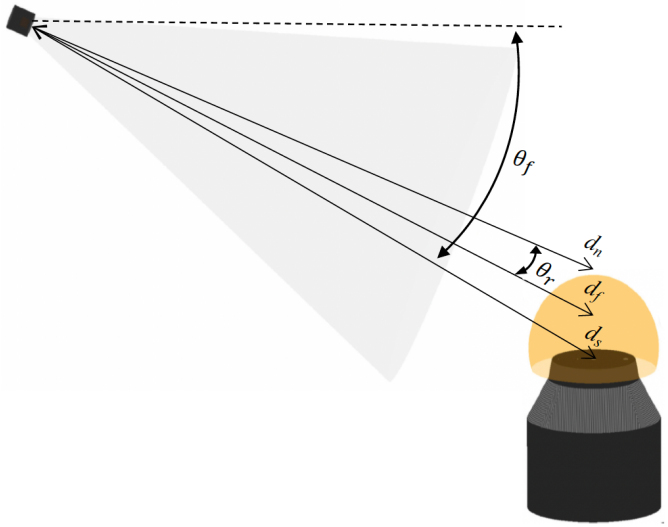

radiometer	d_n mm	d_f mm	d_s mm	θ_r deg.	θ_f deg.
+60	154	160 ± 1.5	160.5	5	21
offset	204	206 ± 2	208	2	55

Figure 2.2 Radiometer schematic

2.4 Images

Videos are recorded at 30 fps by the operations-camera that is placed inside the chamber. Still images are extracted from these frames to illustrate flame dynamics. The image sequences used here are created by using these images.

2.5 Experimental Design

Experiments were conducted onboard the international space station (ISS) to ensure possibility of long duration flames in microgravity condition. The g-level attained in ISS is less than μ-g [65]. A total of 149 successful ignitions were obtained. Twenty-nine of the flames lasted

for a perceived steady state of 120 seconds or more (up to 300 seconds). The rest of the cases started to develop instabilities followed by self-extinguishment.

The burner is installed in a quiescent chamber that is nominally 100-liter capsule before any hardware is installed where the hardware would fill about 15-liters of its volume. Ethylene, and nitrogen-diluted ethylene are used as fuel mixture that represent heats of combustion range of 15 and 47.2 kJ/g [66–68]. The ambient pressure, oxygen concentration and fuel mixture mass flow rate are changed to explore their effects on burning. Three of the atmospheres are nominal NASA selected atmospheres of pressure and oxygen for human habitat in space flight: 21 % oxygen and 1 bar, 26.5% and 0.7 bar and 34 % and 0.565 bar [69]. The mass flux settings and ambient conditions used for these experiments are summarized in Table 2

Table 2.1. Design parameters for BRE-ISS round 1 experiments.

Quantity	Values
$\dot{m}''_{mix}$	1 - 12 g / m^2-s
X_{O2}	0.21 - 0.4
X_f	0.15 to 1
p	0.56 - 1 bar

3 Experimental Results of Round 1 Tests

Burning experiments are analyzed for 59 successfully ignited tests using a gas burner (BRE) to emulate the steady burning of 25 mm diameter flat surface materials. More than half of the tests resulted in long burns of at least 2 and as long as 5 minutes. Mixtures of ethylene and nitrogen allow for 23.6 and 47.2 kJ/g heats of combustion (LHV). Ambient conditions range from 40 to 21 % oxygen and pressures of 1 to about 0.4 bar. NASA human habitat atmospheres have been used. Generally, it has been found that oxygen levels of 26 % and above can allow steady flames. The flames are thin blue in color and grow slowly over time for minutes. Some self-extinguish, some had periodic oscillations, and others appear to have become steady and were shut down. Theoretical analyses show the shutdown flames were steady in growth, and all of the test endpoints were more than 94 % of steady state in flame heat flux. Flame heat flux for set mass flux allowed the estimation of heats of gasification to relate to steady solid materials that might burn in microgravity. Radiometers allowed the computation of flame radiative fraction that appeared to correlate well with the measured flame height. Results are shown for heat flux, flame height and base radius, radiative fraction as a function of fuel mixture mass flux, and various oxygen and pressure atmospheres.

3.1 End Point Results

Table 3.1 gives a summary of the end-point conditions found. The most useful data in this table are the apparent steady results where the duration of the test was long, appeared steady and the fuel flow rate was shut down. The issue of their steadiness will be theoretically examined to provide some justification for further examining these data as steady. The usefulness of these steady data is in the determination of the derived heat of gasification (heat flux divided by mass flux) to relate to real solid fuels that could burn steadily in microgravity at this scale.

Table 3.1. Summary of the ISS tests.

test pt.	X_{O2}	X_f	p bar	$\dot{m}''$ g/m^{2}s	$\dot{q}''_{ctr}$ kW/m^2	$\dot{q}''_{off}$ kW/m^2	$\dot{q}''_{cal}$ kW/m^2	$\dot{q}''_{cal,crc}$ kW/m^2	y_f mm	r_f mm	$\dot{q}''_{r,60}$	$\dot{q}''_{r,off}$	X_r	t_b s	*end pt. condition*
39B3	0.38	1	1.01	2.55	6.52	3.51	14.41	-[1]	22.9	20	-	-	-	180	FT[2]
39A1	0.40	1	1.01	3.84	5.38	2.73	12.75	-	33.0	23.3	-	-	-	120	FT
56A1	0.40	0.5	1.03	4.46	6.27	3.75	14.4	5.89	22.3	17.7	-	60.86	0.58	180	FT
63A1	0.39	0.5	1.02	6.04	4.54	2.41	12.74	-	42.0	21.2	-	-	-	300	FT
56A2	0.39	0.5	1.04	6.39	4.54	2.36	11.65	-	34.9	25.5	-	-	-	180	FT
63B1	0.38	0.5	1.02	8.94	3.73	1.76	9.83	-	62.5	22.3	-	-	-	151	SE[3]
63C1	0.36	0.5	1.02	12.14	3.17	1.45	8.41	-	80.0	24	-	-	-	92	SE
51A1	0.34	1	1.02	2.55	5.18	2.9	11.1	-	24.5	20.9	-	-	-	180	FT
51B1	0.33	1	1.02	3.06	4.79	1.46	9.94	-	28.8	23.4	-	-	-	99	SE
51C3	0.32	1	1.02	3.83	4	2.27	9.04	-	41.8	25.7	-	-	-	66	SE
87D1	0.32	1	0.57	1.18	9.27	5.7	14.6	12.18	10.7	14.5	39.2	24.52	0.439	180	FT
87C1	0.33	1	0.57	1.47	7.51	4.46	14.6	8.37	15.5	17.3	-	40	0.59	180	FT
87B1	0.34	1	0.57	1.78	7.05	4.09	14.4	8.14	16.8	17.8	-	46.43	0.57	180	FT
87A1	0.36	1	0.57	2.07	6.6	3.58	14.7	11.19	19.8	19.4	-	56.32	0.605	180	FT
51D1	0.34	1	0.57	2.55	4.92	2.57	11.76	-	27.2	22.8	-	-	-	180	FT
51F1	0.32	1	0.57	3.07	4.08	2.15	9.44	-	37.6	28	-	-	-	131	SE
51G1	0.30	1	0.57	3.83	3.64	2.09	8.055	-	42.9	26.6	-	-	-	67	SE
94H1	0.35	1	0.57	5.43	3.15	1.66	7.28	-	59.1	34.6	-	-	-	47	SE
94J1	0.33	1	0.57	5.95	2.96	1.62	7.19	-	58.2	35.4	-	-	-	37	SE
94K1	0.30	1	0.57	6.95	2.92	1.67	6.75	-	74.0	34.6	-	-	-	36	SE
66D5	0.34	0.5	0.58	1.76	11.2	6.81	13.2	15.65	6.3	13	21.17	12.93	0.332	180	FT
66D4	0.35	0.5	0.58	1.79	8.21	5.39	13.9	10.83	11.3	14.1	38.9	24.55	0.575	180	FT
66D3	0.35	0.5	0.58	2.05	10.1	6.72	13.8	13.67	8.4	12.9	27.81	17.25	0.346	180	FT
66F1	0.36	0.5	0.57	2.18	9.64	6.39	14.2	13.69	9.1	13.4	29.54	18.46	0.345	180	FT
66G1	0.35	0.5	0.57	2.45	8.2	5.37	13.3	9.06	11.4	14.5	38.1	23.75	0.407	180	FT
66J1	0.33	0.5	0.57	3	6.61	4.11	13.2	8.1	15.2	16.4	-	32.5	0.48		FT
70A1	0.36	0.5	0.57	3.43	6.5	4.32	13.6	6.22	16.5	16.8	-	39.2	0.511	114	FT
70B1	0.35	0.5	0.57	3.95	5.52	3.35	12.5	5.62	20.9	18.4	-	49.51	0.563	120	FT
70C1	0.34	0.5	0.57	4.42	4.61	2.7	12	7.0	25.6	20.4	-	60.12	0.616	120	FT
56D2	0.34	0.5	0.57	4.5	4.54	2.5	12.05	-	41.8	20.2	-	58.61	0.605	180	FT
70D1	0.36	0.5	0.57	4.95	4.48	2.5	12	-	28.1	21	-	-	-	180	FT
56D3	0.33	0.5	0.57	6.38	3.32	1.66	9.03	-	42.6	38.6	-	-	-	137	SE
39C1	0.26	1	0.99	3.84	3.2	2.33	7.43	-	38.1	28.5	-	-	-	26	SE
39D1	0.25	1	0.99	2.54	3.8	2.75	8.65	-	43.5	28.2	-	62.23	0.56	14	SE
87K1	0.25	1	0.71	1.04	7.13	4.1	10.65	12.46	12.6	14.9	36.63	21.27	0.435	180	FT
94G1	0.26	1	0.71	1.17	6.7	3.8	10.1	11.56	15.25	16.6	38.95	24.63	0.455	180	FT
87J2	0.26	1	0.71	1.176	6.63	3.85	10.76	11.99	14.2	16	40.5	25.64	0.492	180	FT
87H1	0.27	1	0.71	1.48	5.95	3.27	10.49	10.56	17.7	18.4	-	36.36	0.567	180	FT
94F1	0.27	1	0.71	1.66	5.33	2.95	9.67	-	25.5	20.4	-	39.84	0.558	133	SE
87G1	0.28	1	0.71	1.79	5.05	2.93	10.04	-	29.9	22.4	-	46.82	0.6	160	SE
94D1	0.28	1	0.71	2.14	4.66	2.62	8.89	-	30.4	23.5	-	54.9	0.585	80	SE
51K1	0.25	1	0.69	3.83	3.17	2.11	6.8	-	44.6	27.2	-	-	-	25	SE
63F1	0.26	0.5	1.01	8.91	2.88	1.7	6.81	-	59.5	22.8	-	-	-	32	SE
63G1	0.25	0.5	1.02	12.13	2.92	1.57	6.62	-	72.7	23.4	-	-	-	28	SE
63D1	0.27	0.5	1.01	6.03	3.41	2.3	7.22	-	44.1	22	-	-	-	33	SE
56B1	0.25	0.5	1.01	4.46	3.71	2.58	7.62	-	27.3	21.1	-	49.06	0.504	38	SE
70L1	0.27	0.5	0.71	1.74	6.92	4.16	9.5	11.64	10.4	12.7	29.24	18.12	0.358	180	FT
70H1	0.27	0.5	0.71	1.94	7.22	4.16	9.8	11.71	11.9	13.8	29.25	18.13	0.425	180	FT
70K1	0.28	0.5	0.71	2.27	6.52	4.06	10.2	10.70	13.3	15.1	36.45	22.22	0.395	120	FT
56F1	0.25	0.5	0.69	4.45	3.48	1.88	8.62	-	28.9	23.4	-	51.73	0.53	42	SE
56G1	0.24	0.5	0.69	5.09	3.11	1.66	8.12	-	28.0	24.5	-	58.72	0.521	35	SE
94A4	0.21	1	1.02	1.156	6.8	4.58	7.38	-	18.7	15.8	29.72	18.52	0.365	37	SE
94A2	0.22	1	1.02	1.43	6.33	4.17	7.67	-	16.0	18	-	26.61	0.416	30	SE
94A1	0.22	1	1.02	1.861	5.3	3.58	7.97	-	21.6	21.1	-	40.89	0.499	21	SE
39H1	0.19	1	1.02	3.06	3.9	2.67	7.24	-	25.0	23.9	-	51.3	0.384	17	SE
39H2	0.18	1	1.02	3.06	4.06	2.7	7.1	-	25.5	24.7	-	50.83	0.38	17	SE
39F1	0.20	1	1.02	3.83	3.07	2.38	6.6	-	33.0	24.9	-	-	-	16	SE
39G1	0.20	1	1.02	5.128	2.31	1.42	7.42	-	60.0	28	-	-	-	13	SE
56C1	0.22	0.5	1.02	4.45	3.05	2.45	6.82	-	28.1	22	-	41.18	0.42	19	SE

1. Radiometer data not available
2. Flow-Terminated (considered as steady)
3. Self-Extinguished

3.2 Unsteady Results

Unsteady results help in illustration of transient behavior of flames as well as distinguishing between steady and self-extinguished flames by observation of transient data and flame images. Data on the heat flux devices and four video cameras recorded the flame images over the time of a test after ignition. Although steady data is the main objective of this work, it is revealing to examine these transient data. For illustration three tests will be discussed here: 87B1, 51D1 and 94K1 of Table 3.1. They have the same nominal atmospheres, 0.34 oxygen mole fraction and 0.56 bar pressure. As the mass flux is increased: 1.78, 2.55 and 6.95 g/m^{2}s, the flame grows taller and finally extinguishes at the highest flow rate. The self-extinguished flames occurred above 3 g/m^{2}s and they all showed periodic growth and decay before final flame cessation. The video frame sequences are shown in Figure 3.1. They have been edited to give the best images, but in all cases, the color of the flames after early ignition effects, are blue. In some cases, apparent soot particles are disgorged through the flame (see Figure 3.1c at 6 s). In Figures 3.1a, and 3.1b, the flames grow and reach steady state before they were intentionally shutdown at about 3 minutes. This had to be done to conserve fuel and maintain reasonably constant atmospheres. The flame grows both radially and vertically in the images, and as the flow rate is increased the flame overhangs below the burner surface around the exposed burner copper edge and similar trend were observed by Ban et. al. General shape of the flames were also observed in ref [70] where the experiments took place in 1-g and their general shape were similar to those observed in current study. Figure 3.1c shows these effects more strongly, but now at 20 s the flame begins to partially extinguish. It periodically moves from full to partial in existence until complete elimination at 34 s.

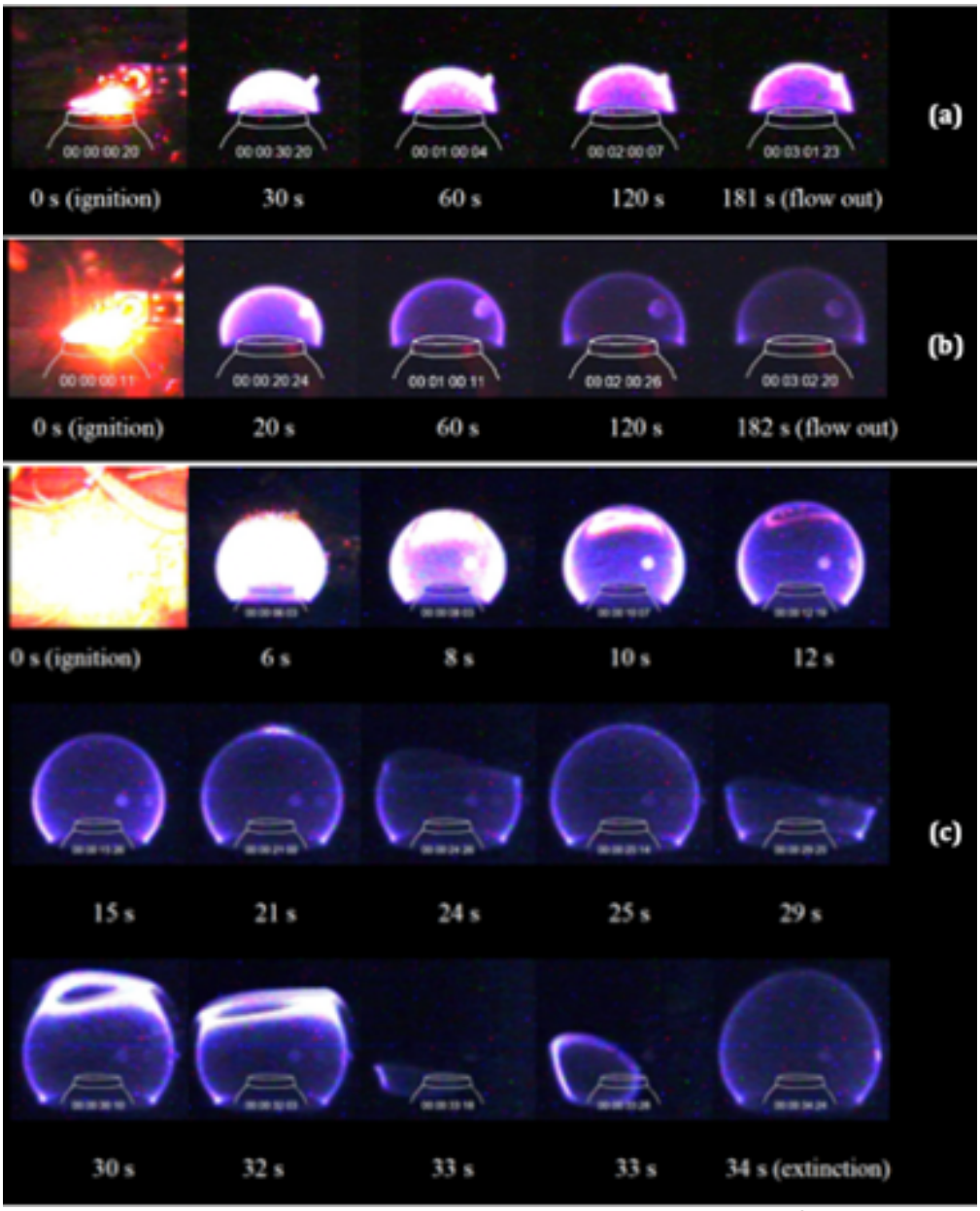

Figure 3.1. Color images of tests (a) 87B1($\dot{m}'' = 1.78\ g/m^2s$), (b) 51D1 ($\dot{m}'' = 2.55\ g/m^2s$), and (c) 94K1 ($\dot{m}'' = 6.95\ g/m^2s$). All are at nominal conditions of $X_{O2} = 0.34$, $X_f = 1$, and p = 0.56 bar.

The unsteady heat flux data are shown in the left plot of Figure 4, for the high flow rate, and the right plot of same figure, for the low flow rate case in Fig 3.1. The uncorrected transient calorimeter results are shown, as only the end points were corrected in Appendix A. These results reveal several unexpected characteristics. First, the center heat flux is higher than the "offset" sensor at 9.5 mm compared to the burner radius of 12.5 mm. One might expect the opposite based on the proximity of the flame to the surface; yet flame radiation from the product gases depends on on volume rather than distance. Second, the heat flux sensors and calorimeter net heat flux values all start very high and decrease to somewhat of an asymptote. In Figure 3.2 (Right), an effect prevalent in many tests, the two local gages drop sharply then gradually until an abrupt upward change occurs, followed by a smooth curve. This is believed to be due to early water condensation on the gages from the combustion products in contact with a relatively cool sensor. The small void space between the sensor and copper top can be a favorable condensation site. The liquid water acts as a barrier to conduction into the gage. The flame begins to evaporate water, further reducing the heat into the gage until it is dry. Then the dry gage suddenly senses the true flame heat flux. This effect was also demonstrated in our laboratory at 1-g. Third, after the water

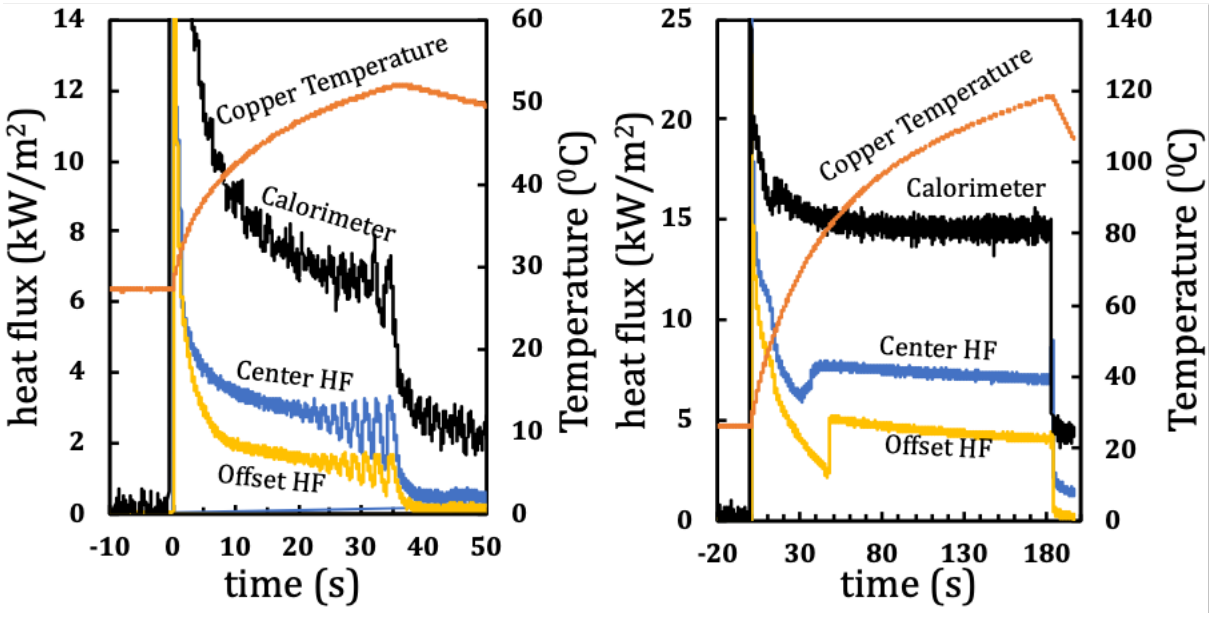

Figure 3.2. Heat flux and surface temperature for tests (Left) 94K1 and (Right) 87B1. Both are at nominal conditions of $X_{O2} = 0.34$, $X_f = 1$, and p = 0.56 bar.

effects, the measurements follow a smooth slow decay as we would expect. In Figure 3.2 (Left) at the high flow rate, it appears heading for an asymptote but becomes periodic before self-extinction, and in Figure 3.2 (Right) at the lower flow rate, the descent appears asymptotic. Fourth, the smooth curve heat flux values following their early descent, have values inversely related to the steady mass flux, e.g., 15 kW/m^2 for 1.78 g/m^2s and about 7 kW/m^2 for 6.95 g/m^2s; this is a typical trend. The transient copper temperature is measured by the two thermocouples on the surface (see Figure 2.1) and both measured values were almost equal. Therefore, the arithmetic average of the two local temperature measurement is used as the copper temperature in Figure 3.2. Moreover, The transient flame length, base radius and Photomultiplier Tube (PMT) with OH* filter assembly [71] for test point 66D5 are presented in appendix B which illustrates the asymptotic behavior of steady BRE flames.

Reexamining the flame behavior for an approximate constant mass flux, but with variations in the pressure, oxygen, and fuel concentration (or heat of combustion of the fuel mixture). According to Table 3.1 and by comparing Figures 3.3a, 3.3b and 3.4a, one could see the effect of nominal ambient oxygen mole fraction as it ranged from 0.4 to 0.265 with other parameters kept constant. In some tests that were shutdown, an apparent steady periodic behavior was demonstrated. This is shown in Figure 3.3b at 1 bar in which the periodic flame extinctions continue for nearly 1 minute before fuel shutdown, yet for the same of the conditions in Figure 3.3b except with an atmospheric pressure of 0.56 bar there was no periodic behavior observed. Perhaps this is a pressure effect indicating the flames are more stable at the lower pressure.

Finally, one could see the effect of fuel mole fraction by looking at Figures 3.3b and 6b. They show flames at nominal ambient oxygen mole fraction of 0.34 and decreasing ethylene mole fraction from 1 to 0.5. All these image sequences suggest that higher oxygen, lower pressure, and lower heats of combustion tend to generate more stable flames that could reach steady state or last longer. Higher ambient oxygen concentration and lower pressure will result in higher flame temperature and higher radiative heat loss respectively, while fuel dilution with an inert (here we used nitrogen) caused flames to get smaller in size and thus decreased radiative heat loss at same

fuel mixture mass flux. This is still under further investigation and will be discussed in more detail later.

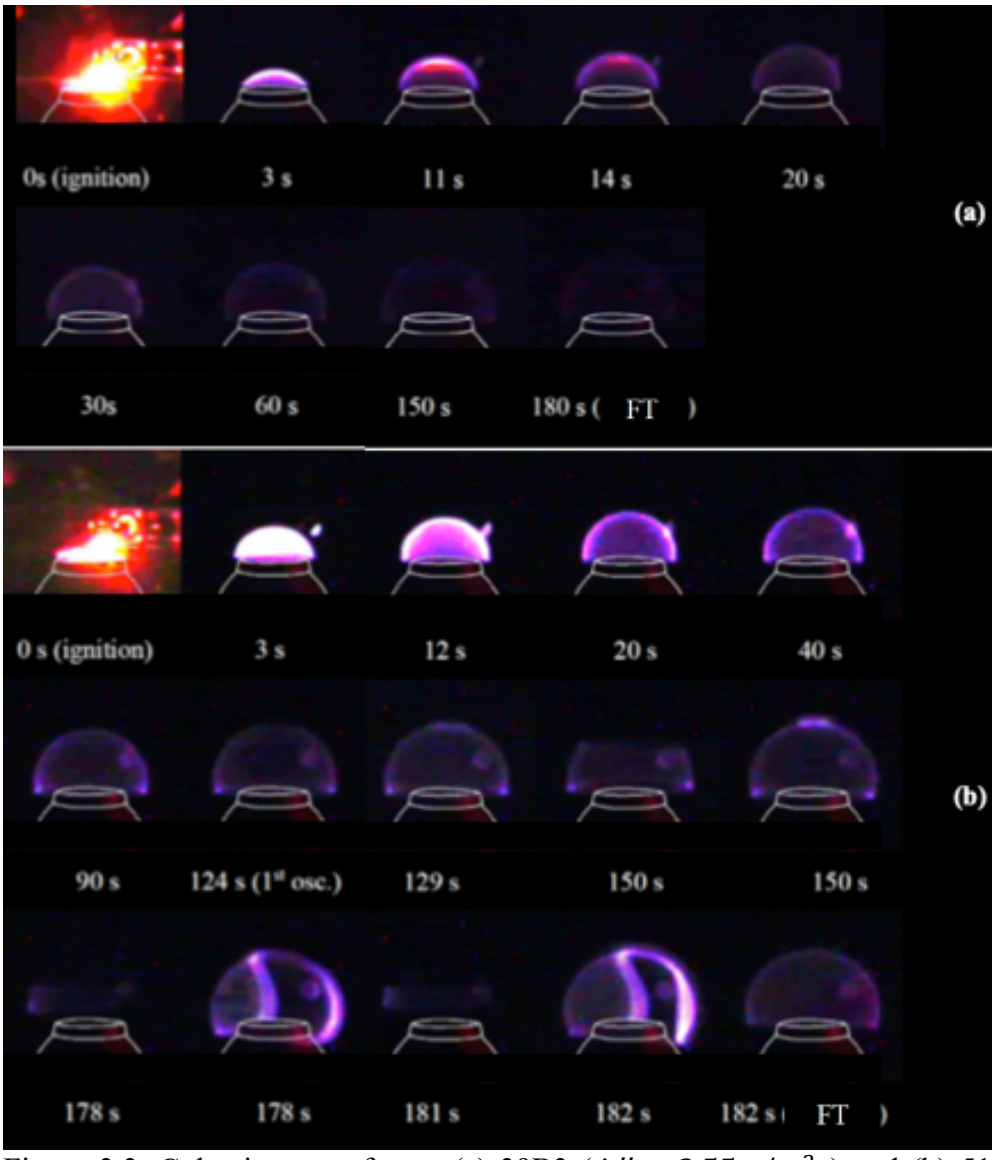

Figure 3.3. Color images of tests (a) 39B3 ($\dot{m}'' = 2.55\ g/m^2s$) and (b) 51A1 ($\dot{m}'' = 2.55\ g/m^2s$). Both are at nominal conditions of $X_f = 1$, p = 1 bar and X_{O2} = 0.4 and 0.34, respectively.

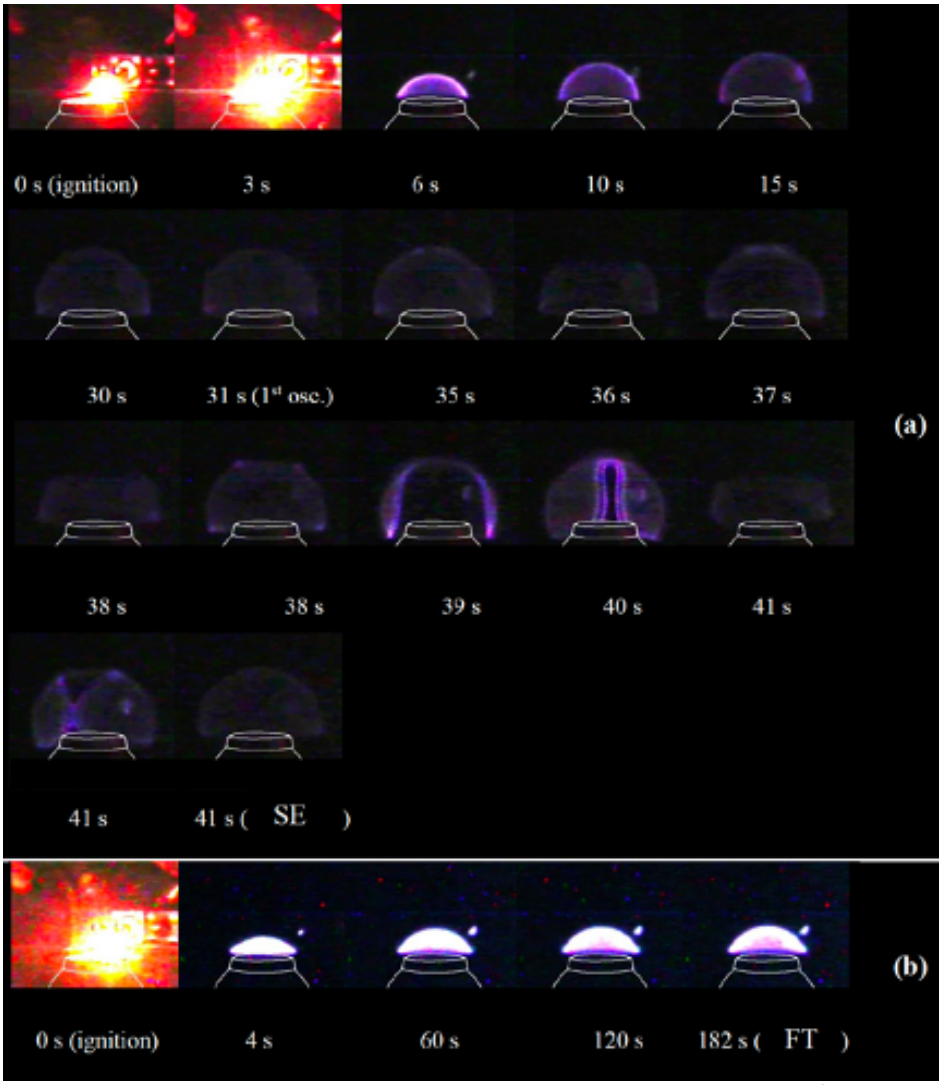

Figure 3.4. Color images of tests (a) 39D1 ($\dot{m}'' = 2.54\ g/m^2s$) and (b) 66G1 ($\dot{m}'' = 2.45\ g/m^2s$). Conditions are $X_{O2} = 0.265$ and 0.34, $X_f = 1$ and 0.5, and p = 1 and 0.56 bar, respectively.

3.3 Steady Results

Here the end point data that did not self-extinguish in the time of the test will be examined. In order to justify their use as "steady" or nearly steady, a theoretical analysis can be used as a measure. It has been previously shown that analytical

Unsteady theory has been a good predictor of tests [49]. The analytical solution to this theory gives the mixture fracture, *Z.* The solution is based on classical diffusion flame theory with the assumption of unity Lewis number for the steady problem. Then it is shown in [49] that a transient term can accurately be added to the steady solution. This gives the following approximate analytical solution for the mixture fraction in Eq. (3.1).

$$Z = \left\{ \frac{1 - \exp\left[\frac{2\,\lambda}{\pi} \tan^{-1}\left(\xi_f \right) - \lambda \right]}{1 - \exp\left(-\lambda \right)} \right\} \operatorname{erfc}\left(\frac{\xi_f}{2\sqrt{\tau}} \right), \tag{3.1}$$

where the complementary error function contains the unsteady term that reflects the transient behavior of mixture fraction in space where it approaches unity as burn-time is increased. Equations 3.2 to 3.4 represent dimensionless time, ambient mass diffusivity and dimensionless mass flux, respectively.

$$\tau = \frac{D_\infty t}{R^2}, \tag{3.2}$$

$$D_\infty = \frac{k}{\rho c_p}, and \tag{3.3}$$

$$\lambda = \frac{\dot{m}''}{\frac{4k}{\pi c_p R}}. \tag{3.4}$$

The dimensionless flame position, ξ_f, is found by the stoichiometric value of the mixture function, and this is also the dimensionless flame height. Therefore, from the experimental end point data, the value of *erfc* can be evaluated. Theoretically a value of 1 is steady. Figure 3.5 shows the results for all the end point data. It clearly shows that the data that did not self-extinguish have values of nearly unity, while those that self-extinguished, range from 0.2 to 0.9 monotonically as time increases. Constant properties of nitrogen at 1400 K are used to obtain steadiness (*erfc*) of the flame heights.

Comparing the heat flux growth illustrated in Figure 3.6, with the flame growth in Figure 3.5, it can be observed that the flame grows more slowly than changes in the heat flux. Theory shows that [49] the near surface effects approach steady conditions faster than those farther away.

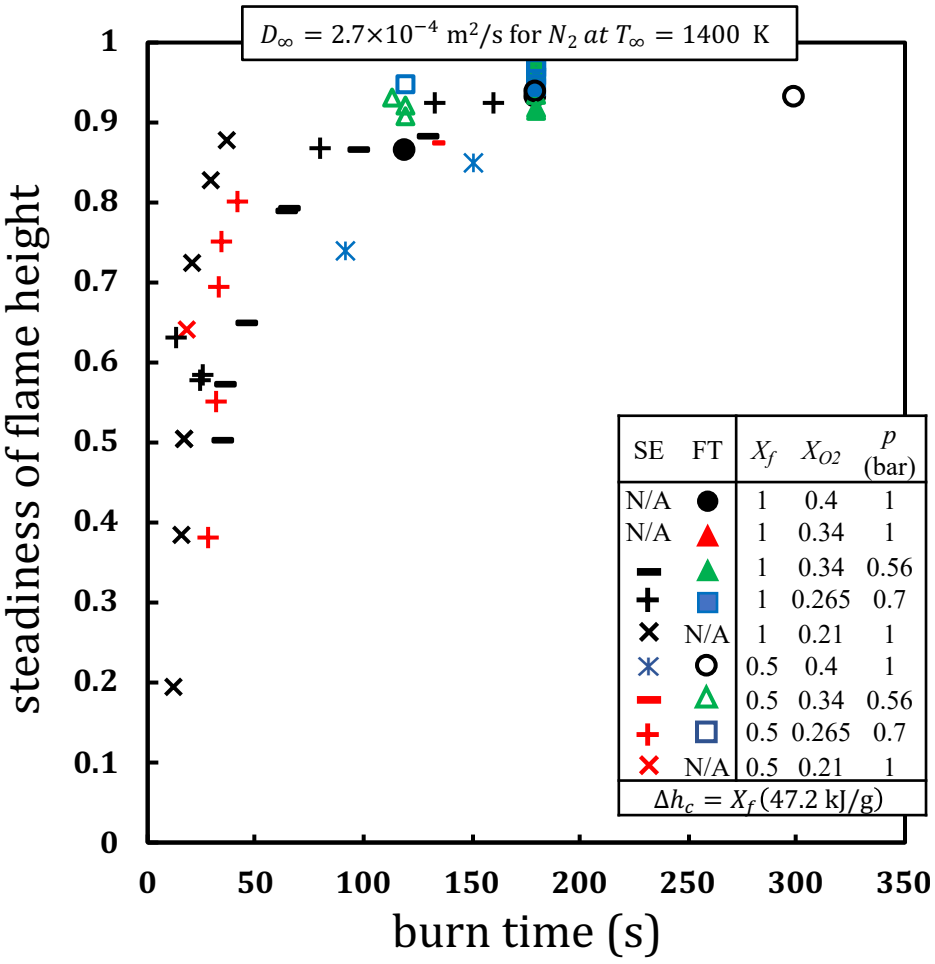

Figure 3.5. Steadiness of flame height for all the tests.

This can be assessed for the data in Table 3.1 by examining the unsteady solution for the convective heat flux at the center (see Eq. 3.5). Eq. 3.6 represent the unsteady part of the theoretical convective heat flux [49].

$$\dot{q}_s''(r=0) = -\frac{k}{R}\left[(T_s - T_\infty) - \frac{\Delta h_c\, Y_{ox}}{S\, c_p}\right] A_{\epsilon=0}\,. \tag{3.5}$$

The unsteady part of the theoretical convective heat flux [49] is expressed as

$$A_{\epsilon=0} = \frac{1}{\sqrt{\pi\,\tau}} + \frac{2\,\lambda}{\pi}\left[\frac{\exp(-\lambda)}{1-\exp(-\lambda)}\right]. \tag{3.6}$$

The steadiness factor, i.e., the ratio of the steady to unsteady values is expressed as

$$X_{q,st} = \frac{\frac{2\,\lambda}{\pi}\left[\frac{\exp(-\lambda)}{1-\exp(-\lambda)}\right]}{\frac{1}{\sqrt{\pi\,\tau}} + \frac{2\,\lambda}{\pi}\left[\frac{\exp(-\lambda)}{1-\exp(-\lambda)}\right]}\,. \tag{3.7}$$

The steadiness of the heat flux results is presented in Figure 3.6, with nitrogen properties at 850 K used to evaluate the constant property parameters. (The constant property solution requires judgment in selecting properties and near wall and near flame temperatures have been used relating the data to theory). The results clearly show that even for the unsteady self-extinguished data, the heat flux is 80% or more of its steady value. It is suggested that these self-extinguished heat flux values could be used to indicate materials that seek steady burning but die out as the flame grows. From here on let us just examine primarily the "steady" end points.

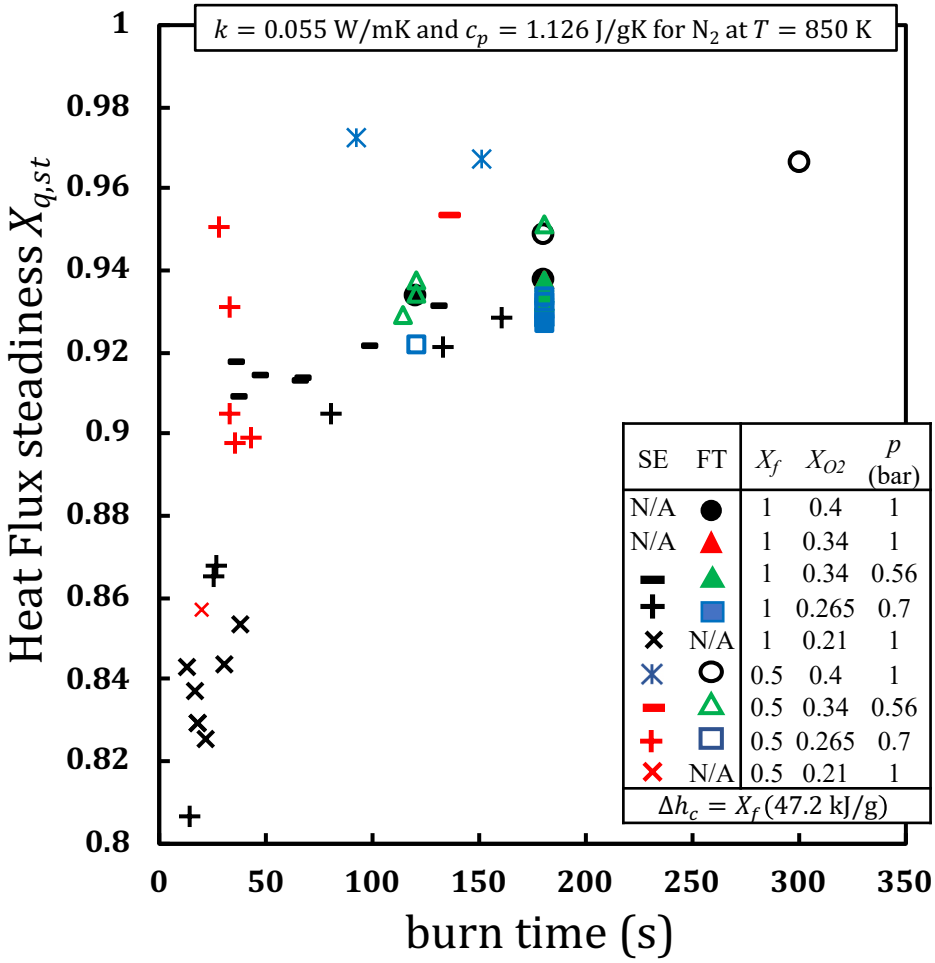

Figure 3.6. Steadiness of heat flux for all the tests.

A commercial equation solver was utilized to equate calculated flame height (Derived from Eq. 3.1), and surface heat flux (Eq. 3.5) with corresponding measured quantities which resulted in finding the "best" constant properties used for each case.

3.3.1 Heat Flux

The local sensor and average net heat flux results from Table 3.1 for the "quasi-steady" data are used. The calorimeter heat flux values have been corrected to eliminate the unwanted heating of the copper burner exposed edge non-flow portion. The details are shown in Appendix A. Here the steady data end points are plotted against mass flux in Figure 3.7 for the local sensors and the corrected average calorimeter net heat fluxes.

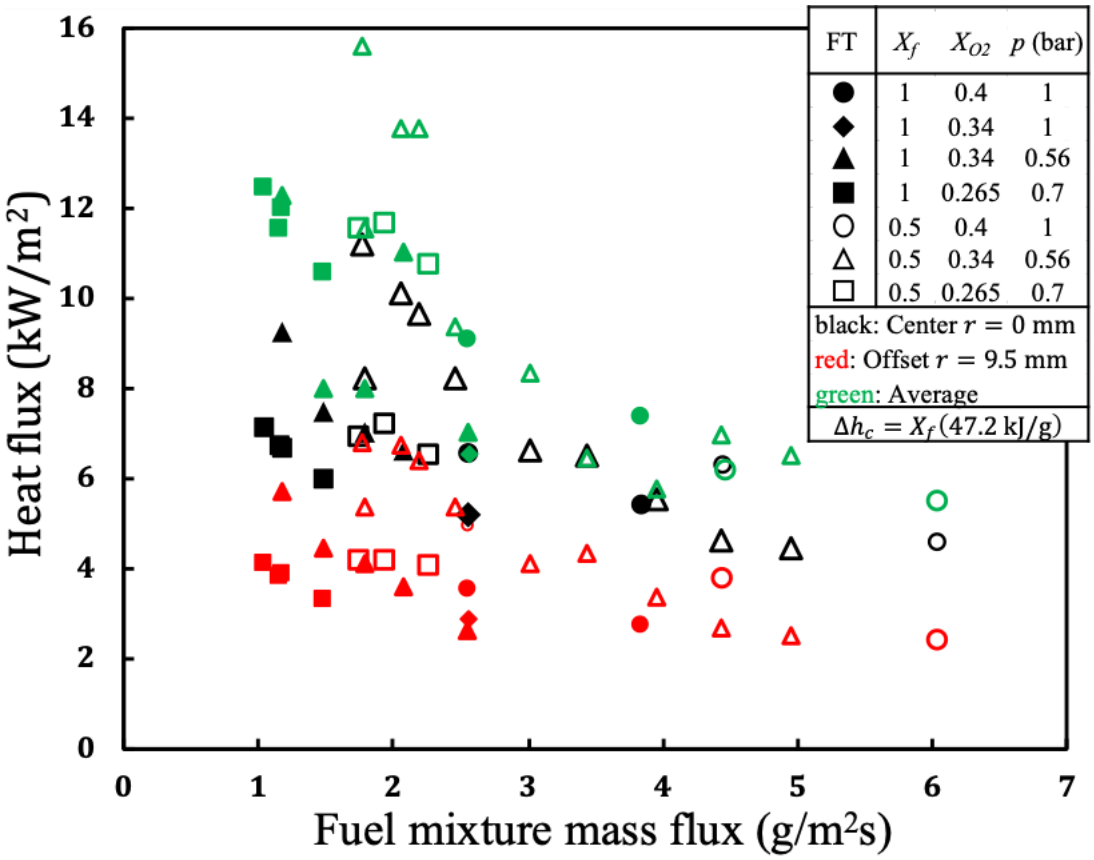

Figure 3.7. Measured local and average heat flux (measured by calorimeter [26], see appendix A) plotted with respect to fuel mixture mass flux for the FT tests.

Let us delineate the trends in the heat flux plots as a function of the mass flux, atmospheric oxygen and pressure, and fuel concentration in the fuel mixture stream. The latter represents the heat of combustion. First the local values will be examined. Center heat flux was about 50 % higher than offset located at r = 9.5 mm. Both heat fluxes decrease as the mass flux is increased. (This is associated with the flame located further from the surface). Heat fluxes increase nearly directly proportional to oxygen concentration. (But no steady data for 21 % oxygen). Heat fluxes increase as the heat of combustion decreases; nearly inversely related. (This is associated with flame height). Data at nominal 0.34 X_{O2}, pure fuel, and fixed mass flux 2.55 g/m^{2}s show a very slight increase in heat flux with pressure (This is insignificant and inconclusive).

Let us now examine the average heat flux from the calorimeter. Figure 3.7 shows only the corrected data, and those data are less than the total collected because needed radiation information was not available for all the tests. The corrected data generally reduced the original data by up to a factor of 3 in a few cases, but the trend of the corrected data is now consistent with the local data to give us confidence that the correction is sound. The trends for the average heat flux are similar to the local data. Corrected average heat flux can be 20 to 70 % higher than the local center heat flux. Heat flux decreases with mass flux, increases with X_{O2} and decreases with fuel mole fraction. Also, data at nominal 0.34 X_{O2}, pure fuel, and fixed mass flux 2.55 g/m^{2}s show a very slight decrease in heat flux with pressure. (This is insignificant and inconclusive).

3.3.2 Flame Radiation Fraction $\boldsymbol{X_r}$

Two radiometers (+60 and offset) were used to determine the radiation coming from the flame and the burner surface. The heat flux measured by each radiometer is presented in table 3.1. Saturation of the radiometers limited their use and therefore not all tests have results in Table 3.1. Figure 2.2 shows a schematic of the radiometer orientations as well as the details of the distances and angles elaborated.

The radiant rate of energy to the sensor is found from the radiometer's normal component of heat flux $\dot{q}_r''$ with respect to the vector from the flame centroid located at the half of the flame height, see Eq. (3.8). Optically thin flame sheet with a point source of radiation with uniform

radiant intensity is assumed. This is justified because the radiometer distance is large compared to the flame size. The energy recorded by the radiometer is composed of flame $\dot{q}''_{f,r}$ and burner surface re-radiation $\dot{q}''_{s,r}$ which is given by Eq. (3.10). The burner surface re-radiation is eliminated to give the flame radiant energy as shown by Eq. (3.9).

$$\dot{Q}_{f,r} = 4\pi d_f^2 \dot{q}''_{f,r} \tag{3.8}$$

$$\dot{q}''_{f,r} = \dot{q}''_r - \dot{q}''_{s,r} \tag{3.9}$$

$$\dot{q}''_{s,r} = \frac{\epsilon_s \sigma F_{s-r} A_s (T_s^4 - T_\infty^4) cos\theta_f}{cos\theta_r} \tag{3.10}$$

The view factor between the burner surface and radiometer is given by Eq. (3.11). *X* and *Y* are calculated from geometrical details of the radiometry setup [72,73], given as

$$F_{r\to s} = \frac{X}{2}\left[\frac{1 + X^2 + Y^2}{\sqrt{(1 + X^2 + Y^2)^2 - 4Y^2}} - 1\right], and \tag{3.11}$$

$$X = \frac{h}{b}, Y = \frac{a}{b}, \tag{3.12}$$

with *a* being the radius of the burner, *h* the vertical distance from the burner surface to the radiometer elevation, and *b* the horizontal distance to the radiometer. The radiant fraction is then computed from the known combustion energy as

$$X_r = \frac{\dot{Q}_{f,r}}{\dot{m}'' \Delta h_c \pi R^2} = \frac{4\pi d_f^2 (\dot{q}''_r - \dot{q}''_{s,r})}{\dot{m}'' \Delta h_c \pi R^2} . \tag{3.13}$$

The measured radiant fractions are given in Table 3.1 where radiometer data were useable. The end-point data were used just before fuel termination (FT) or self-extinction (SE) at the peak in oscillating flames.

The flame is blue in all these tests as shown in Figs. 3.1, 3.3 and 3.4. This is common for microgravity burning with little or no soot. Therefore, the radiation comes from the gases above and below the blue flame. Figures 3.8a and3.8b show the "steady" and self-extinguished end-point data where radiation fraction could be determined from the radiometers. The trends of Figure 3.8a show that the fuel mole fraction (or heat of combustion) dominates over X_{O2} and pressure. The radiant fraction is nearly directly related to the heat of combustion with the pure fuel nearly twice as high as the diluted fuel mixture. It might appear that "steady" flames cannot have a radiant fraction above about 60%. Extinction of microgravity flames has been associated with radiation loss and subsequent flame temperature drop. For now, this relationship is not examined.

It will be seen that flame height is also directly related to the heat of combustion. So, it suggests that radiant fraction might be more directly related to flame height. Moreover, there is a similarity between flame height and radius, so flame height might be a representation for volume and radiation losses from the aggregate of flame gases. Such a plot is presented in Figure 3.8b. Here a logarithmic correlation is given for the "steady" data only, but the figure includes the data just before extinction as well. The extinguished data somewhat follow the correlation, but we will interpret the correlation to hold for the "steady" end point flame, not for self-extinguished cases. The extinguished data range from about 0.5 – 0.8 for low X_{O2} (21 and 26.5%). While these are relatively high values of radiant loss fraction, there does not appear to be a critical value for extinction.

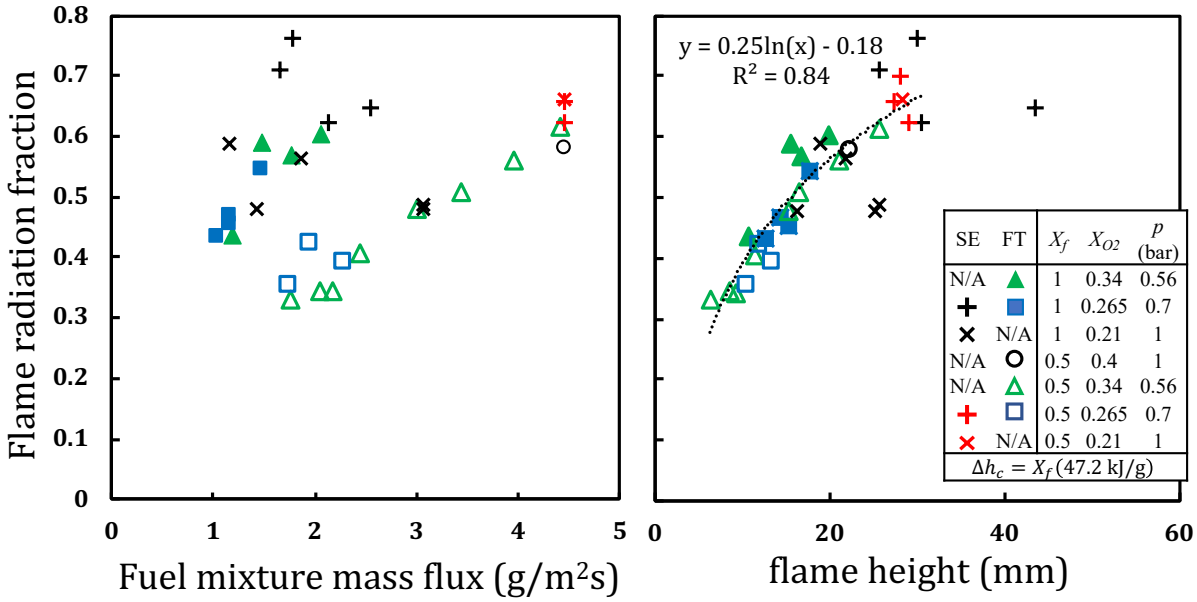

Figure 3.8. Flame radiant fraction vs. mass flux (a) and flame height (b) for all steady end-point results.

3.3.3 Flame Shape

The flame shape nearly follows the previous theory of half oblate ellipse as demonstrated by Markan et. al.[49]. Both the height and radius grow with time as shown in Figures 3.9 and 3.10. The flame radius pulls in at the edge of the burner, distorting it from the theoretical ellipse. It may either standoff or extend a small distance below the burner face. Here we plot the flame height, the distance vertically from the center of the burner, and the radius, the radial distance along the face of the burner. Figures 3.9 and 3.10, show the results for the steady flames as a function of mass flux. As with the radiant fraction, the flame height and radius at "steady" state are primarily grouped by heat of combustion and increase with mass flux and heat of combustion. It is known from theory that the flame radius is a singular function of its length. In spite of not perfectly following the elliptical theory, this similarity is shown for the "steady" data in Figure 3.11.

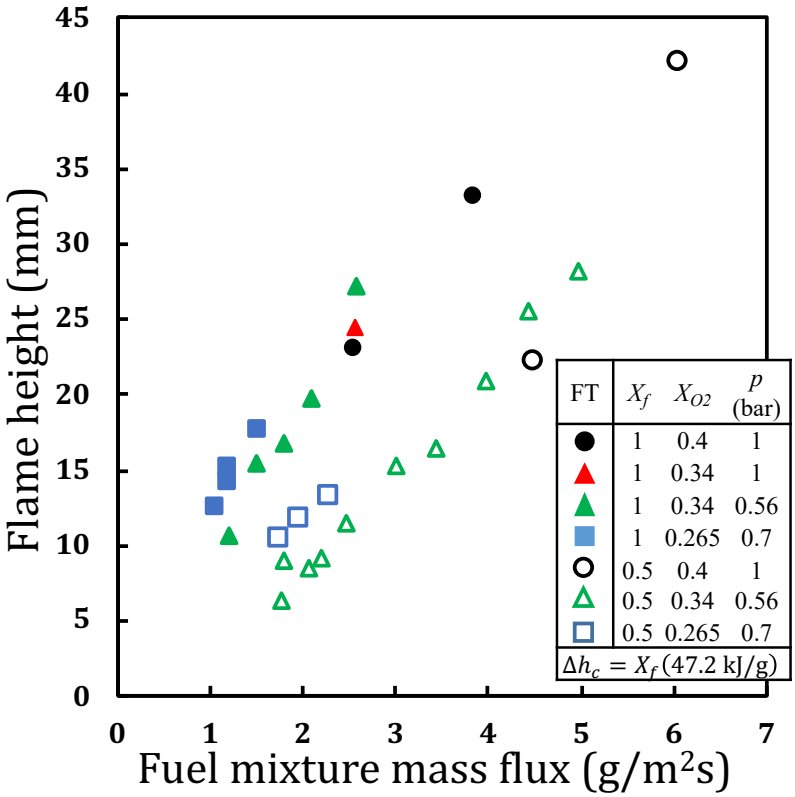

Figure 3.9. Flame height vs. mass flux.

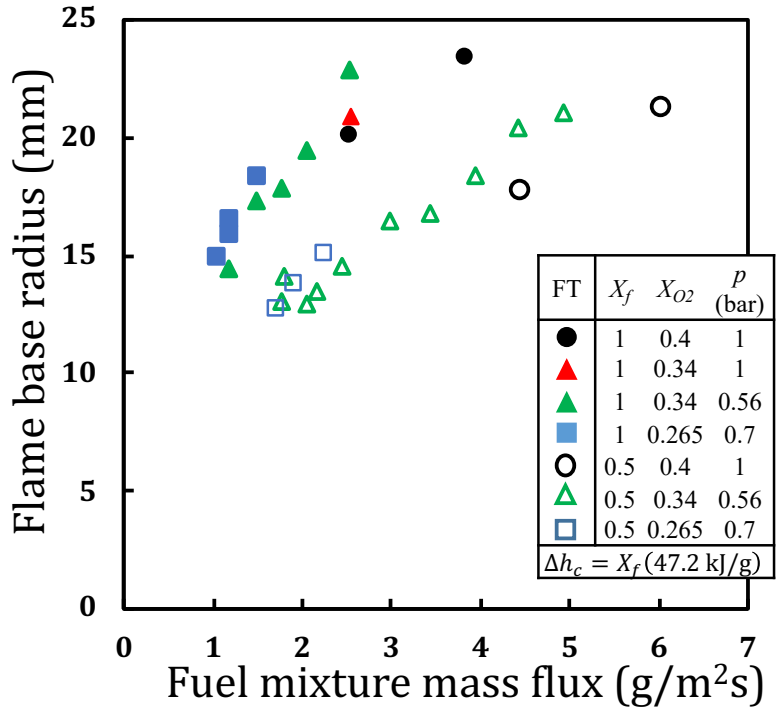

Figure 3.10. flame base radius vs. mass flux.

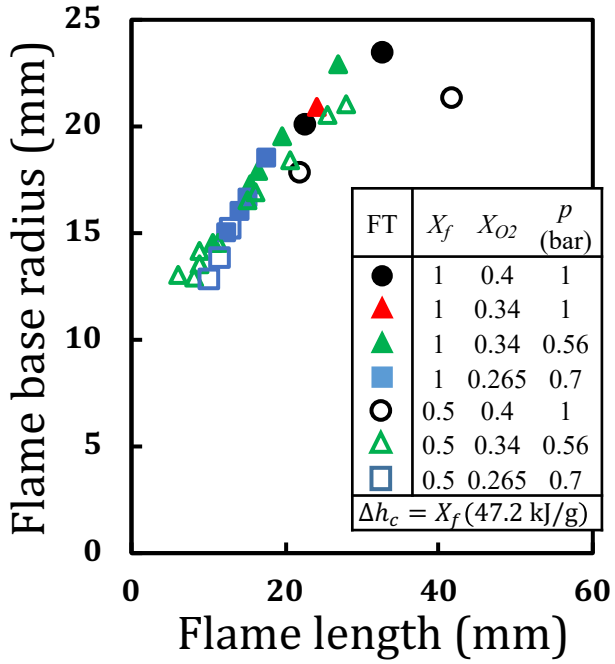

Figure 3.11. Flame height vs. flame base radius

3.4 Discussion of Results

In the previous section the results have been presented and their trends have been discussed. The measurements have been used to compute the local and average net heat fluxes to the burner and derive the flame radiant fractions. The primary objective of this study is to determine if, and under what conditions, steady flames can occur in microgravity. We believe this is the first-time steady burning has been observed for a flat surface of 25 mm diameter in a quiescent atmosphere. Previously a tiny cylindrical candlewick has been observed to burn steadily [34,35]. The significance here for the burner is that steady burning can be related to condensed fuel properties through the theory of steady burning. Our hypothesis in this work has been to demonstrate that four fuel properties control steady condensed phase burning. This has been demonstrated in 1-g experiments by showing that burning rate, flame shape and color could be matched between real condensed phase fuels and a burner as discussed herein [46,55,56]. The four fuel properties required for matching in the 1-g experiments are heat of combustion, heat of gasification (L), fuel surface temperature and smoke point respectively.

The burner steady endpoint surface temperatures ranged from 40 to 120 ^{0}C. These temperatures are relatively low for solid-phase fuels such as non-charring plastics that would apply directly here but, in the theory of steady burning the surface temperature is a relatively weak property compared to 1 and 2 above. In addition, the smoke point is likely irrelevant in microgravity, as it controls the radiation due to soot and that is not present in the microgravity flames seen. Consequently, the heat of combustion and the heat of gasification associated with the steady burner flames should represent the key solid fuel properties that can govern steadily burning in microgravity at 25 mm diameter. This has important safety implications.

The heat of combustion in these experiments varies from 23.6 kJ/g for $X_f = 0.5$ and 47.2 kJ/g for $X_f = 1$ based on ethylene. This is a range representative of many plastics. The question now is to evaluate the heat of gasification. Ideally the calorimeter net heat flux is the way to compute the heat of gasification, L. The theory of steady burning gives

$$L = \frac{\overline{\dot{q}''}_{convection} + \overline{\dot{q}''}_{f,r} - \overline{\dot{q}''}_{rr}}{\dot{m}''} \tag{3.14}$$

where the quantities shown in Eq. (3.14) are the average values of convective heat flux, flame radiative heat flux back to the surface and surface re-radiation over the burner, respectively. Not having a clean calorimeter average value due to edge heating, we resort to two ways to estimate the average net heat flux to the burner: first, calorimeter corrected value and second, arithmetic average of the two local net heat fluxes.

The results are shown in Figures 3.12 and 3.13. Both plots indicate a decreasing, somewhat inverse asymptotic-like curve, for heat of gasification with mass flux. It is surprising that the data cluster about a nearly singular trend. Also, both plots show the heat of gasification is up to 20 % higher for the lower heat of combustion 23.6 kJ/g. The results of Auth [55,56] who used the BRE in 1-g are added to Figures 3.12 and 3.13. The 1-g results for propane-nitrogen mixtures have the opposite behavior with heats of gasification decreasing with heat of combustion for the same mass flux. This could be due to the significance of soot radiation in the 1-g flames. But again, the data mostly cluster about one trend except for very low heat of combustion. The 1-g corresponding heat of combustion data shift far to the right and down from the microgravity data of Figures 3.12 and 3.13. For example, the 1-g data would indicate ($L, \dot{m}''$) points of about 2 kJ/g, 30 g/m^{2}s, and 0.5 and 10. Moreover our previous work in a 5- s drop facility suggested similar data trends but with an apparent vertical asymptote at about 3 g/m^{2}s, rather than 1 as shown here. Obviously, the current data at durations of minutes over 5- s are more accurate. Moreover, it has been shown that the ISS heat flux data even at self-extinction are theoretically nearly steady. Figures 3.12 and 3.13 include the heats of gasification derived from the self-extinguished endpoint data as well. Remarkably, the self-extinguished not data follow the same trend as the steady data.

Let us interpret Figures 3.12 and 3.13 in terms of the flammability of real materials in microgravity. Typical melting plastics have heats of gasification ranging from about 2 to 3 kJ/g, with effective heats of gasification for charring plastics above 4 kJ/g. Some selected literature

values for materials with heats of combustion in the BRE range are listed in Table 3.1 [67,74]. Figures 3.12 and 3.13. would suggest that polyethylene (PE) and polypropylene (PP) would burn in microgravity at about 3 g/m^{2}s. Nylon and PMMA would burn at about 2.5 g/m^{2}s, and the phenolic glass fiber composite would burn at about 1 g/m^{2}s. These are very low values and if they occurred in 1-g they would be near the critical conditions for burning [75,76]. Indeed, Auth [55,56] finds that at 25 mm diameter, PMMA burns steadily at 19 g/m^{2}s, and PE and PP both burn at about 6 g/m^{2}s. It is doubtful that the phenolic-glass composite could burn without extra external heating in 1-g. Yet, Figures 3.12 and 3.13 suggest it could burn in microgravity. The implication is that materials can burn more easily in microgravity than in normal gravity but with much lower burning rates.

Fires on Earth in normal gravity become big, sustained fires because of heating from the fire's surroundings. Fire on Earth is difficult generally to initiate in solids because of only 21 % oxygen in the atmosphere. In the current study it is seen that also in microgravity, this oxygen concentration did not favor 'steady" burning. Can we expect fires to grow in microgravity so that as they heat their surroundings they can be reinforced as on the earth? The key to that answer is what controls the microgravity fire as it increases in size? Will flame radiation extinguish it? These questions need to be fully answered before fire safety in microgravity is understood.

One important fire safety consideration, based on the findings of this study, is that solid materials with heats of combustion in the range 23.6 to 47.2 kJ/g and heats of gasification from about 1 to 10 kJ/g can burn in microgravity. The NASA alternative flammability Test 2 using the Cone Calorimeter can measure these material properties [77,78]. As this study develops a more complete understanding, NASA may wish to put more emphasis into Test 2.

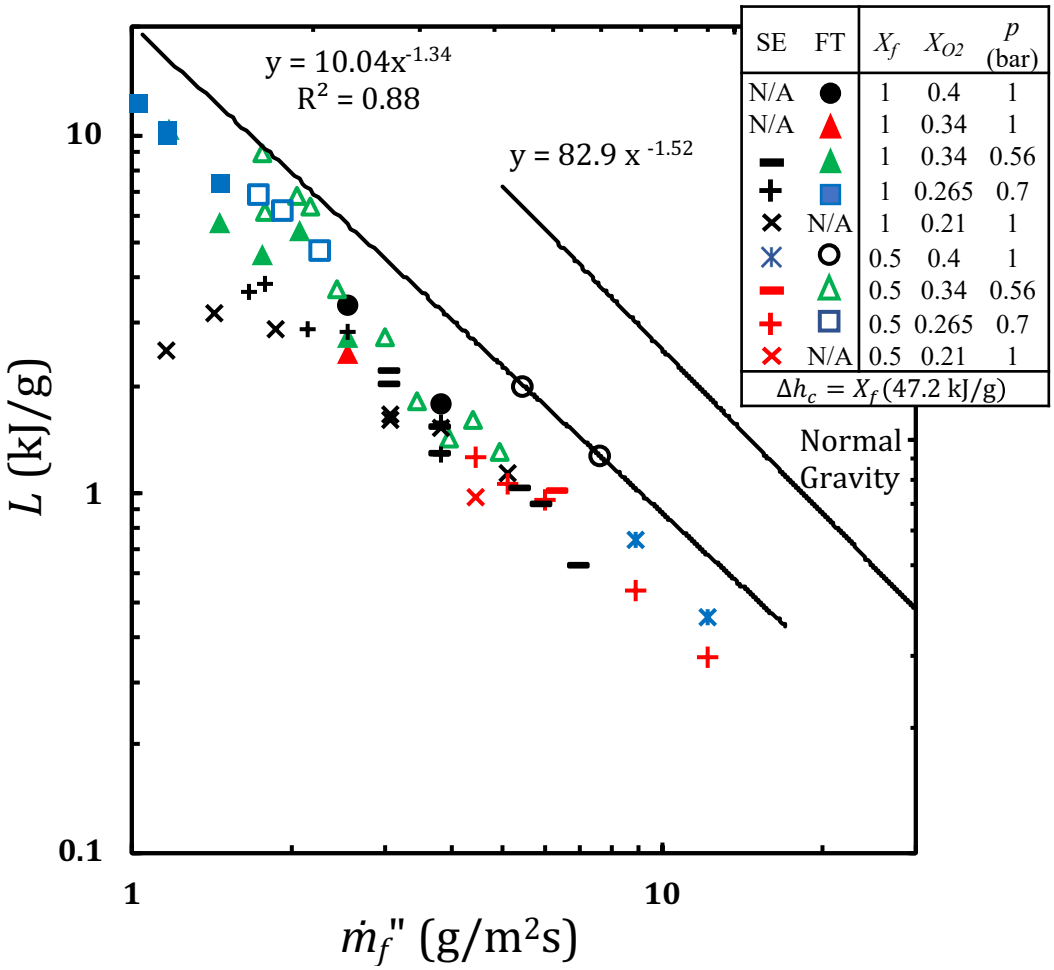

Figure 3.12. heats of gasification calculated from corrected calorimeter vs. mass flux

Table 3.2 . Materials close to BRE heats of combustion and corresponding heats of gasification

Material	*LHV*, kJ/g	*L*, kJ/g
PE	43.4	1.9
PP	44	2.0
Nylon	28.8	1.5, 2.4
PMMA	24.2	1.6, 2.3
Phenolic glass fibers	22.0	7.3

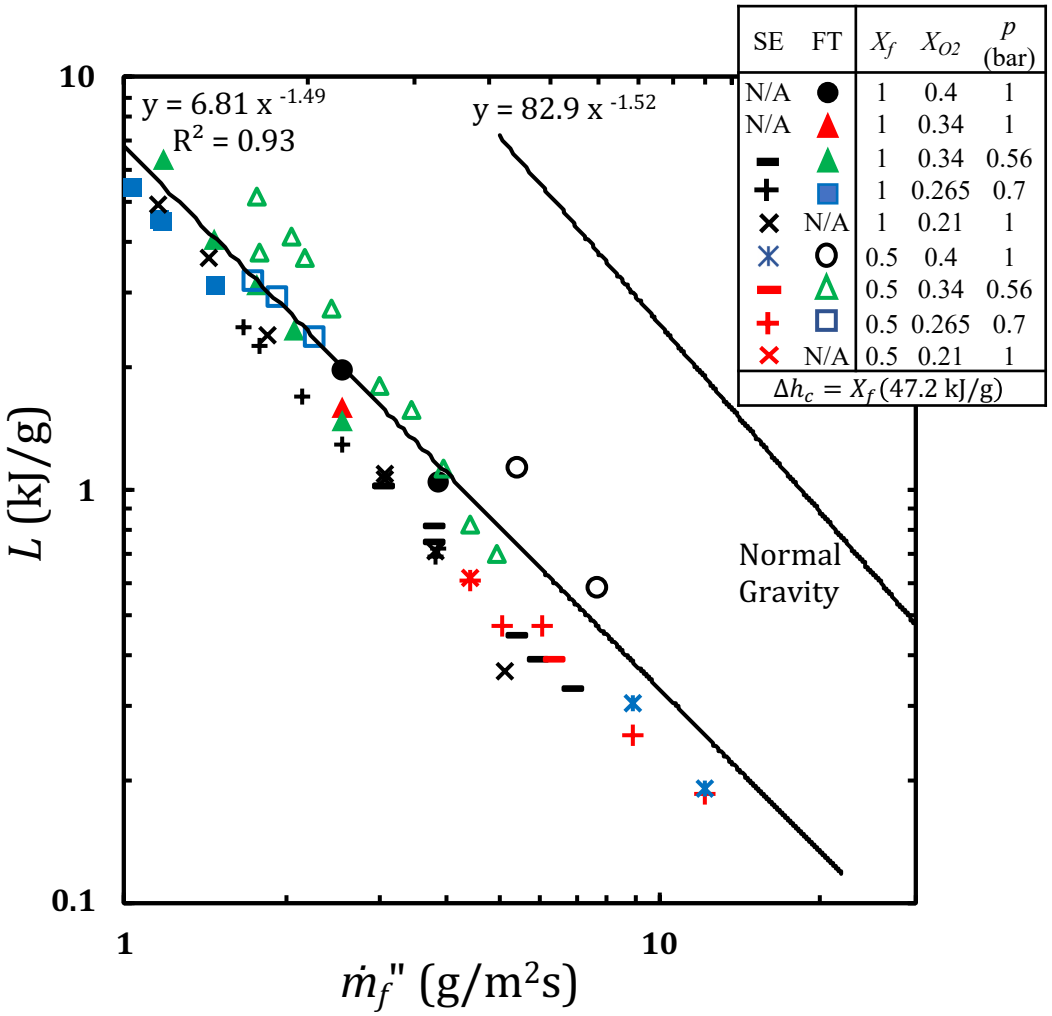

Figure 3.13. Heats of gasification calculated from the average of the two heat flux gauge measurements vs. fuel mixture mass flux

3.5 Chapter Summary

The primary conclusion from this study is that the BRE has indicated that steady burning can be achieved in microgravity for a flat surface of 25 mm diameter. Experiments have shown that burning could take place for more than 3 minutes with apparent steady blue hemispherical-like flames at atmospheres above 21 % oxygen. Theoretical analyses based on published work has corroborated that these long duration flames are nearly steady where it is shown that surface heat

flux tend to approach its steady value faster than flame size. Moreover, it is shown that lower fuel mole fractions (or heats of combustion) and higher ambient oxygen concentrations help flames burn for longer durations. Further analyses of the heat fluxes measured have allowed the estimation of the heat of gasification property associated with the steady tests. The findings suggest that solids of 25 mm diameter surfaces with heats of combustion from about 23.6 to 47.2 kJ/g, and heats of gasification of 1 to 10 kJ/g can steadily burn in microgravity. Many commercial materials have these properties. In microgravity, flames with lower heats of combustion, were closer to the burner surface which resulted in higher surface heat flux and larger heats of gasification accordingly which was a trend not seen in our 1-g experiments.

Flame radiation fractions are obtained by radiative heat fluxes measured at endpoints for steady and at the peak of oscillating flames prior to self-extinction for self-extinguished flames. It is observed that all steady flames radiation fractions remained below 0.6. In addition, it has been found that the flame radiation fraction for the steady flames correlates well with the flame height. Future work will develop this relationship further to include other parameters and utilize it with previously published theoretical models to predict the steady outcome in general. Hopefully, that analysis will give a more complete answer to the potential for fire growth in microgravity.

4. Analytical Transient Solution for Constant Mass Flux

Burning experiments are analyzed for 29 steady burning flames using a gas burner (BRE) to emulate condensed phase burning of 25 mm diameter flat surface. Mixtures of ethylene and nitrogen allow for 23.6 and 47.2 kJ/g heats of combustion (LHV). Ambient conditions range from 21 to 40 % oxygen and pressures of 0.56 to 1 bar. The results are compared to predictions from analytic models developed to determine the flame radiation fraction, flame convective and radiative heat fluxes, flame shape, and heats of gasification for steady burning. Steady burning is theoretically decided by ensuring the flame temperature is above a critical value of 1100 K. Good agreement is achieved between experiment and predicted steady results. Further computations are made to determine the effect of ambient pressure and oxygen on burning for heats of combustion of 23.6 and 47.2 kJ/g, diameters up to 100 mm, and vaporization temperatures of 80 and 350 ºC. It is found that for the range of analyzed conditions, heats of gasification of about 1 to 5 kJ/g, steady burning would result over a range of about 1 to 6 g/m2s. Low pressure appears to yield more stable flames. The results have implications on how the fire safety of materials in microgravity should be determined.

The complete solution for the unsteady purely diffusive burning of an oblate ellipsoidal surface with a uniform surface mass flux in time is given by Markan et al[49]. The results are summarized here because the formulas will be used throughout the paper as modified to include the heat of combustion reduced by a flame radiation loss fraction, X_r, the ratio of radiant energy lost by the flame to its combustion energy. The use of representing flame radiation effect by reducing the heat of combustion essentially assumes “a transparent flame” according to Jiang et al [79]. The original solution is based on thin flame theory with Schwab-Zeldovich variables giving the mixture fraction as given in Eq. (4.1)

$$Z = \frac{c_p(T - T_\infty) + \Delta h_c\ (Y_O - Y_{O,\infty})/S}{c_p(T_s - T_\infty) - \Delta h_c\ Y_{O,\infty}/S} \tag{4.1}$$

The temperature T and oxygen mass fraction Y_O are combined into this mixture fraction variable, where $Y_{O,\infty}$ is the ambient oxygen mass fraction, Δh_c is the heat of combustion per mass of the prescribed fuel-diluent stream, c_p is the specific heat of the gas and S is the stoichiometric ratio which denotes the mass of oxygen consumed per unit mass of fuel-diluent stream. It is

assumed that the Lewis number Le $\equiv k/\rho c_p \mathcal{D} = 1$. Also, the diffusivity, $\mathcal{D}$, is equal and replaced by the thermal diffusivity, $k / \rho c_p$. Properties are constant, but the numerical choice of properties will be based on a temperature judgment, as convective heat flux will depend on properties near the surface, and flame shape will depend on properties near the flame. In the original work, a convective Peclet number (Pe_c) is defined in terms of the total mass flow rate ($\dot{M}$) over the entire ellipsoidal surface (*top and bottom*) which is given by Eq. (4.2) and (4.3).

$$Pe_c = \frac{\dot{M}}{4\pi c \rho \mathcal{D}} \tag{4.2}$$

$$Pe_c = \frac{\dot{M}}{4\pi R \rho \mathcal{D}} = \frac{2\dot{m}'' \pi R^2}{4\pi R k/c_p} = \frac{\dot{m}'' c_p R}{2k} \tag{4.3}$$

In the current paper we replace the Peclet number by the dimensionless mass flux (λ) from one side of flattened ellipsoid to define the burner surface (see Eq. (4.4)).

$$\lambda = \frac{\dot{m}''}{\left(\frac{4k}{\pi c_p R}\right)} \tag{4.4}$$

Here λ is a prescribed constant, however, in the steady state burning theory, the corresponding burning eigenvalue is equivalently found in terms of the solid fuel properties and *B* number as given by Eq. (4.5)

$$\lambda = \ln(1 + B) \tag{4.5}$$

where Eq. (4.6)

$$B \stackrel{\text{def}}{=} \frac{(Y_{O,\infty}\,(1 - X_r)\Delta h_c/S - c_p(T_s - T_\infty)}{L_m} \tag{4.6}$$

is the effective *B* number and Eq. (4.7)

$$L_m \stackrel{\text{def}}{=} L - \frac{\dot{q}''_{f,r} + \dot{q}''_e - \dot{q}''_{rr}}{\dot{m}''} \tag{4.7}$$

is the effective heat of gasification. In typical solutions for steady burning problems, the results are given in terms of the fuel properties: heat of combustion, heat of gasification, vaporization temperature; and in term of ambient conditions: oxygen, pressure and temperature. Here, for the burner, the solution is given in terms of λ over *L*. This is a subtle, but distinct difference. In steady state, the substitution of Eq. (5) makes the two forms identical. But in the BRE experiments

we do not know L appriori. In BRE and in steady burning of an evaporating liquid or solid, the heat of gasification, L, (a material property) is found by Eq. (4.8)

$$L = \frac{\dot{q}''_{net}}{\dot{m}''} \tag{4.8}$$

where $\dot{q}''_{net}$ is measured; it is generally composed of

$$\dot{q}''_{net} = \dot{q}''_{f,c} + \dot{q}''_{f,r} - \dot{q}''_{rr} + \dot{q}''_{ext,r} \tag{4.9}$$

Where each component is defined as:

$\dot{q}''_{f,c}$: Flame convective heat flux

$\dot{q}''_{f,r}$: Flame incident radiative heat flux

$\dot{q}''_{rr}$: Surface radiative loss heat flux

$\dot{q}''_{ext,r}$: Incident external radiative heat flux

The external radiative heat flux is not present in the experiments but could be included in the theory to follow. It is well known that external radiation in room fires on Earth plays an important and perhaps essential role in the fire development. In the theoretical development herein, the net heat flux will be decomposed into two predictive components: one for radiation and one for convection or pure diffusion.

4.1 Flame position

The solution for the transient mixture fraction is given as in Eq. (4.10)

$$Z = \left\{ \frac{1 - \exp\left[\frac{2\lambda}{\pi}\arctan(\xi) - \lambda\right]}{1 - \exp[-\lambda]} \right\} \operatorname{erfc}\left(\frac{\xi}{2\sqrt{\tau}}\right) \tag{4.10}$$

with τ being the dimensionless time $\left(\tau = \frac{D_\infty t}{R^2}\right)$ and D_∞, the mass diffusivity of ambient air $\left(D_\infty = \frac{k}{\rho c_p}\right)$. In terms of the ellipsoidal coordinate, ξ that can be expressed in cylindrical coordinates (x, r) as

$$\xi = \frac{1}{\sqrt{2}R}\left[x^2 + r^2 - R^2 + \sqrt{(x^2 + r^2 - R^2)^2 + (2xR)^2}\right]^{\frac{1}{2}} \tag{4.11}$$

It can be shown that at $r = 0$, $\xi(x, 0) = \frac{x}{R}$.

The fuel and oxygen are separated by the infinitesimally thin flame sheet that is located where oxygen and fuel become zero by equating the mixture fraction to its stoichiometric value which is shown by Eq. (4.12)

$$Z = Z_f = \frac{Y_{O,\infty}}{SY_{Fb} + Y_{O,\infty}} \tag{4.12}$$

With fuel mass fraction at surface given by Eq. (4.13)

$$Y_{Fb} = 1 - \frac{(1 + \alpha)}{\alpha} e^{-\lambda} \tag{4.13}$$

where $\alpha = S/Y_{O,\infty}$.

By setting the mixture fraction equal to its value at the flame, the flame position is given for a given value of ξ in time.

It is important to observe that the solution for the flame position is primarily controlled by diffusion, $\rho D = k/c_p$, and stoichiometry, S. This follows as $\Delta h_c/S = \Delta h_O$, the heat of combustion per unit mass of oxygen consumed, is generally almost constant, and taken in this analysis for the experimental fuel, ethylene as 13.76 kJ/g. The flame position has no dependence on flame radiation because it is governed solely by diffusive effects. This will prove extremely advantageous as it was found that the measured flame radiative fraction is a strong function of the flame height for steady burning [51]. Explicitly the complete transient flame position, in terms of the mixture fraction on the flame sheet, can be computed from Eq. (4.14)

$$Z_f = \frac{Y_{O,\infty}}{SY_{Fb} + Y_{O,\infty}} = \left\{\frac{1 - \exp\left[\frac{2\lambda}{\pi}\arctan(\xi_f) - \lambda\right]}{1 - \exp[-\lambda]}\right\} \operatorname{erfc}\left(\frac{\xi_f}{2\sqrt{\tau}}\right) \tag{4.14}$$

Let us complete listing of the theoretical steady solutions for flame temperature and convective heat flux. These now depend on the flame radiative fraction.

4.2 Flame Temperature

The theoretical flame temperature can be calculated by Eq. (4.15) with T_f representing the flame temperature

$$c_p(T_f - T_\infty) = \left(\frac{1}{\alpha Y_{Fb} + 1}\right)\left[c_p(T_s - T_\infty) + Y_{Fb}(1 - X_r)\Delta h_c\right] \tag{4.15}$$

Based on Eq. (13), note the flame temperature dependence on λ.

4.3 Convective heat flux

The average steady convective heat flux is given as shown by Eq. (4.16)

$$\overline{\dot{q}_c''} = \left(\frac{4k}{\pi R c_p}\right)\left\{\frac{\lambda}{e^\lambda - 1}\right\}\left[\frac{\Delta h_c(1 - X_r)Y_{O,\infty}}{S} - c_p(T_s - T_\infty)\right] \tag{4.16}$$

The average convective heat flux is one term needed to derive L in Eq. (4.8). But to illustrate the nature of the transient effect on the convective heat flux, the transient local value is given by Eq. (17)

$$\dot{q}_c''(r,t) = \frac{\left(\frac{k}{R}\right)\left[(T_s - T_\infty) - \frac{\Delta h_c(1 - X_r)Y_{O,\infty}}{S c_p}\right]\left[\frac{1}{\sqrt{\pi\tau}} + \left(\frac{2\lambda}{\pi}\right)\left\{\frac{\exp[-\lambda]}{1 - \exp[-\lambda]}\right\}\right]}{\sqrt{1 - \left(\frac{r}{R}\right)^2}} \tag{4.17}$$

In Reference [49] it was shown that the transient toward steady conditions is relatively fast for the heat flux, but slower for the flame growth. In the following, these solutions will be examined against the steady data of reference [51]. To complete the solution for all quantities except flame position, a means is necessary to allow the prediction of the flame radiative fraction. This will be empirically developed shortly in section 4.

4.4 Steady flame position: experiments compared to theory

The flame height along the axis normal to the burner at $r = 0$ is given by Eq. (4.18)

$$\frac{x_f}{R} = \tan\left\{\frac{\pi}{2}\left(1 + \frac{\ln\left(\frac{\alpha}{\alpha + 1}\right)}{\lambda}\right)\right\} \tag{4.18}$$

For a given mass flux, value of $\rho D = k/c_p$ taken at nitrogen properties of 1400 K, and stoichiometry, S found from $S = \Delta h_c/\Delta h_O$, the steady axis flame height can be calculated. For the experimental conditions the steady values are compared to those measured.

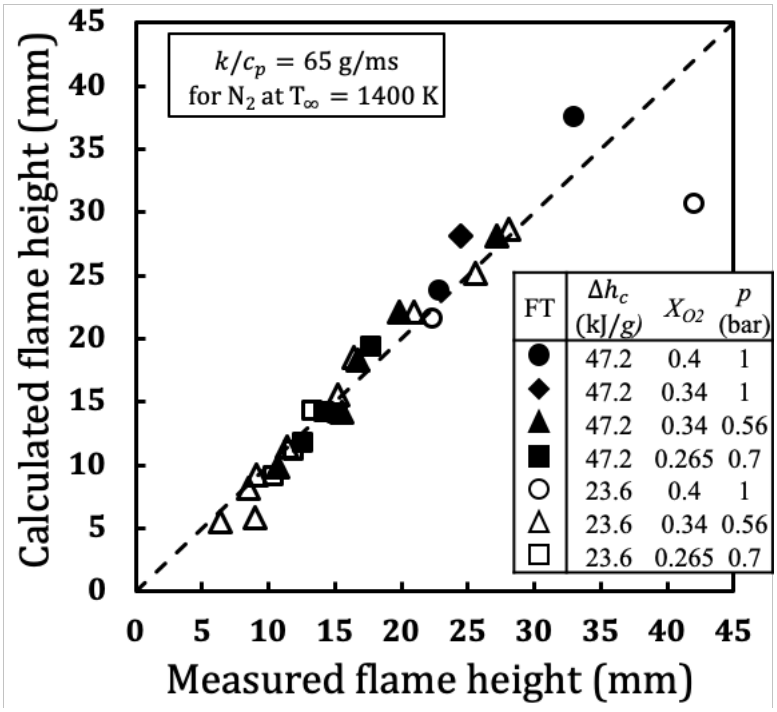

Figure 4.1. Measured vs. calculated flame height

Figure 4.1 shows a direct comparison between the measured *steady* and predicted flame heights. The properties were evaluated at 1400 K for nitrogen based on optimizing the results. As the choice of properties in a constant property solution requires judgment, we justify this choice since the flame position is in a domain of the flame temperature and select this high value with some justification. It can be seen from the figure, that for a wide range of mass flux, oxygen and pressure conditions, the results show good accuracy for the predictions. It should be emphasized that the prediction holds for fuels with heats of combustion of 23.6 and 47.2 kJ/g. The effect of oxygen is also accounted for over a range of mole fractions of 0.265 to 0.40, realizing that at 0.21 the flames tended to extinguishment before any steady state could be reached.

Limited theoretical results have been examined to show that the theoretical oblate ellipsoidal flame shape is not completely satisfied in the experiments. As experimental images

show the flames growing to ellipsoidal and even spherical shapes away from the base, but the measured flame radius at the burner surface ($x = 0$) is over-predicted [49]. So, the ellipsoidal shape is not satisfied near the base. The formula for the base flame radius is given by Eq. (4.19)

$$\frac{r_f}{R} = \sqrt{1 + \left(\frac{x_f}{R}\right)^2} \tag{4.19}$$

The similarity of the dimensionless base radius with the flame height is shown for the data. The prediction can be assessed in Figure 4.2. The theory clearly under-predicts, but the similarity is evident. A modification of the formula in Eq. (4.20) gives an improved result and clearly shows the similarity. The value of the constant c is 0.35.

$$\frac{r_f}{R} = \sqrt{1 + c\left(\frac{x_f}{R}\right)^2} \tag{4.20}$$

It may depart from the theoretical ellipsoidal solution as for that case the problem is symmetric about the long axis while for the burner this is not the case, and only one side applies.

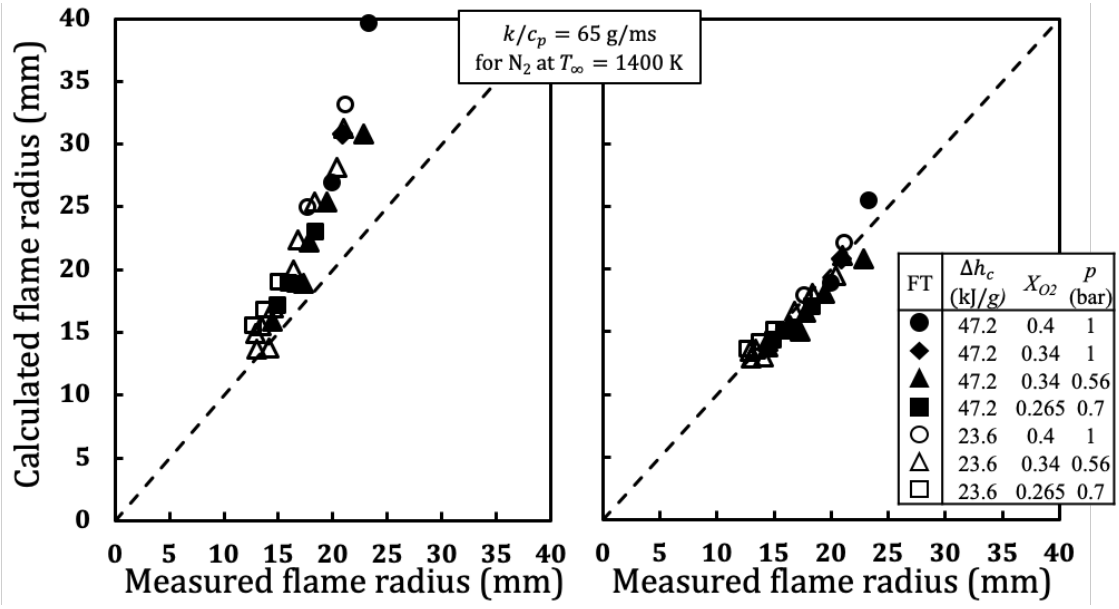

Figure 4.2. measured vs. predicted flame base radius, c =1 (Left) and c = 0.35 (Right)

4.5 Prediction of flame radiation fraction

It was observed in the analysis of the data that the measured flame radiant fraction of the steady flames was a primary function of the flame height [51]. This prompted us to examine herein a theoretical basis for the radiant fraction cast in dimensionless terms. It will be shown that this exploration leads to a much more general correlation for the flame radiant fraction in terms of more variables than just flame height. Providing a prediction of X_r will then allow us to theoretically compute flame temperature at steady state, flame convective heat flux and model flame radiative heat flux from the initial information. This is how we will develop an approximant complete steady solution.

4.6 Radiant fraction model formulation

The radiation lost by the flame, with no visible soot, can be attributed to the products of combustion and their distributed temperature within a volume around the flame. The combustion products radiative heat flux is distributed through a surface area enclosing this volume. The rate of radiation lost by the flame can be represented in terms of a temperature, the gas emissivity, and

its enveloping area. A dimensionless formulation is made based on homogeneous grey gas radiation for a representative path height. The flame radiative fraction is defined as the ratio of the rate of radiant energy lost from the flame with the rate of energy released by combustion (see Eq. (4.21)).

$$X_r = \frac{\dot{Q}_r}{\dot{Q}_c} \tag{4.21}$$

The combustion energy rate is straightforward and represented in terms of the mass flux and heat of combustion as shown by Eq. (4.22):

$$\dot{Q}_c = \dot{m}'' \pi R^2 \, \Delta h_c \tag{4.22}$$

The rate of heat by radiation given off from the flame can be roughly written as Eq. (4.23) [80–82]

$$\dot{Q}_r \approx \varepsilon_f \sigma T_f^4 A_f \tag{4.23}$$

where ε_f is emissivity of the radiating gas, T_f is a representative flame temperature, A_f is the flame enclosing surface area. The emissivity is given in terms of the absorption coefficient computed from the gas partial pressures and temperature. It is clear Eq. (4.23) is approximate but should be considered as representing the maximum temperature and gas concentrations over the scale of the region around the flame, to be taken as the flame length. An integrated form of Eq. (4.23) will have these terms with some distribution and stretching of geometry. With a hope of similarities in distributions, the final results might be considered general for the fuel used here. An examination of this theoretical framework will be assessed when empirically related to the current experimental measurements for X_r.

The following scale approximations are made, anticipating the derivation of an empirical dimensionless formula to be derived from data. The path length is taken as the flame height, and the flame area is taken as its square:

$l = x_f$, the flame height, and Eq. (4.24) is used to estimated flame surface area.

$$A_f \approx x_f^2 \tag{4.24}$$

Let these terms be selected to best represent the problem with the intention to identify the controlling dimensionless groups for X_r.

Consider our *ethylene flames* at various fuel mole fractions, X_f, in a nitrogen mixture; various ambient oxygen mole fractions, X_O, and atmospheric pressure, p. Stoichiometry for complete combustion is justified, as no soot is observed and the chemical reaction is shown by Eq. (4.25):

$$\left(C_2H_4 + \frac{(1-X_{C_2H_4})}{X_{C_2H_4}}N_2\right) + 3\left(O_2 + \frac{1-X_O}{X_O}N_2\right) \rightarrow 2CO_2 + 2H_2O + \left(3\frac{1-X_O}{X_O} + \frac{(1-X_{C_2H_4})}{X_{C_2H_4}}\right)N_2 \quad (4.25)$$

The partial pressure for water vapor and carbon dioxide, are to be equal, and given as shown by Eq. (4.26).

$$p_{H_2O} = p_{C_{O_2}} = \left\{\frac{2}{2+2+3\left(\frac{1-\chi_{O_2}}{X_{O_2}}\right)+\frac{1-X_{C_2H_4}}{X_{C_2H_4}}}\right\}p \quad (4.26)$$

In general, the partial pressures of the radiating species considered, water vapor and carbon dioxide, can be expressed in terms of total pressure, the mole fractions of pure fuel in the supply mixture, and the oxygen in the ambient. Here we just consider ethylene as that was the fuel used in the BRE experiments. Therefore, in the following there is an implicit fuel effect implied. Moreover, the fuel itself can be a radiation participant and that fuel effect is assumed to be contained in any correlation with the BRE ethylene data here.

The radiation from the flame will be represented here in terms of the stoichiometry values of the water vapor and carbon dioxide associated with a path length. The pathlength is taken as the flame height, x_f. These might be considered extremes but should be representative scales given similarity for these particular flames by theory.

The emissivity of the flame gases is then represented as given by Eq. (4.27)

$$\varepsilon_f = 1 - e^{-\kappa_f x_f} \quad (4.27)$$

The total combustion energy release rate is written as shown by Eq. (4.28)

$$\dot{Q}_c = \dot{m}'' \pi R^2 \, \Delta h_c \quad (4.28)$$

Then the radiation fraction becomes (see Eq. (4.29))

$$X_r \approx \frac{\sigma T_f^4 (1 - e^{\kappa_f x_f}) x_f^2}{\dot{m}'' \pi R^2 \, \Delta h_c} \quad (4.29)$$

where the temperature can be evaluated from the theory as given in Eq. (4.15) or

$$\frac{T_f}{T_\infty} = 1 + \frac{\left[\left(\frac{T_s}{T_\infty} - 1\right) + Y_{F,b}\left(\frac{\Delta h_c}{c_p T_\infty}\right)(1 - X_r)\right]}{(\alpha Y_{Fb} + 1)} \tag{4.30}$$

and is a function of X_r.

Arranging as dimensionless quantities to represent X_r gives an implicit relationship (g is an unknown function) for X_r, as the flame temperature depends on it (see Eq. (4.31)).

$$X_r = g\left[\frac{1}{\pi}\left(\frac{\sigma T_\infty^4}{\dot{m}''\,\Delta h_c}\right)(1 - e^{\kappa_f x_f})\left(\frac{x_f}{R}\right)^2\left(\frac{T_f}{T_\infty}\right)^4\right] \tag{4.31}$$

We could make the substitution for the flame temperature and obtain an implicit theoretical solution for X_r. This would be tedious and may not be accurate in the end. As an alternative, let us make the RHS of Eq. (30) as a known quantity by defining a known *characteristic temperature*, $T_{f,o}$, with no radiation loss as given by Eq. (4.32)

$$\frac{T_{f,o}}{T_\infty} = 1 + \frac{\left[\left(\frac{T_s}{T_\infty} - 1\right) + Y_{F,b}\left(\frac{\Delta h_c}{c_p T_\infty}\right)\right]}{\left(\alpha Y_{F,b} + 1\right)} \tag{4.32}$$

Now a dimensionless flame radiation parameter Ω in terms of known quantities that also are dimensionless is found from Eq. (4.33). In other words, X_r is a function of $\Omega, X_r = f(\Omega)$ with

$$\Omega = \left(\frac{\sigma T_\infty^4}{\dot{m}''\,\Delta h_c}\right)(1 - e^{-\kappa_f x_f})\left(\frac{x_f}{R}\right)^2\left(\frac{T_{f,o}}{T_\infty}\right)^4 \tag{4.33}$$

The emissivity or absorption coefficient now needs to be determined as all other terms are known or can be computed, i.e., Eq. (4.18).

4.6.1 Model for emissivity and absorption coefficient

A common way to evaluate emissivity for CO_2 and H_2O gases is to use Hottel's charts [82,83]. In doing so, one must select a path length for a given partial pressure and temperature. The absorption coefficient can then be found from Eq. (4.27). It is pointed out by deRis [84] that for flames without soot, the absorption coefficient will depend on path length, approaching the Planck value in the small limit. The Planck absorption coefficient for CO_2 is about 10 $(\text{m-bar})^{-1}$ and 2 $(\text{m-bar})^{-1}$ for H_2O at 1400 K [74,83]. Note the absorption coefficient of Eq. (4.27) can be

determined from the Planck value by multiplying it by the partial pressure of the gas. Ultimately, we would like to have a relationship for the absorption coefficient in terms of the partial pressures of CO_2 and H_2O

Following encouraging estimations from the Hottel charts, we sought a more easily used computational method and used RADCAL [58,59] to calculate the gas mixture emissivity. RADCAL is a narrow-band model often used to estimate emissivity and absorption coefficient for these gases. The absorption coefficient of RADCAL is found by calculating the received intensity at a point located at a distance l by taking into account the emission from the participating gas at temperature T_g with the surroundings at a fixed blackbody temperature of 300 K. The total emissivity calculated by RADCAL yields an also effective absorption coefficient defined in the same way as Eq. (4.27) for a given path length, l.

RADCAL was run for partial pressures of water vapor and carbon dioxide from Eq. (4.26), ambient temperature (300 K), radiating gas temperature selected at 1400 K, no soot, and path length, l. Operating with the RADCAL code for the set of fuel and ambient pressure and oxygen conditions as our ISS experimental data, a general relationship is found for the absorption coefficient. Specifically, this was put in terms of $\tilde{\kappa}$ as a function principally of path length. Here a *modified absorption coefficient*, $\tilde{\kappa}$ is defined as

$$\tilde{\kappa} \stackrel{\text{def}}{=} \frac{\kappa}{p_{CO2} + p_{H2O}} \tag{4.34}$$

This parameter is similar in form but not identical to the Planck mean absorption coefficient and is motivated because the absorption coefficient tends to be dependent on the gas partial pressure. Figure 4.3 shows that for the steady data set with 9 conditions examined in this way by using RADCAL. As indicated by deRis [84], a singular relationship results for the modified absorption coefficient as a function of path length. The optically thin mean Planck value for CO_2 is about 10 $(\text{m-bar})^{-1}$ and 2 $(\text{m-bar})^{-1}$ for H_2O at 1400 K, respectively [83]. It can be observed that these numbers compare in order of magnitude to the 8.5 $(\text{m-bar})^{-1}$ for a path length of 10^{-6} m in Figure 4.3. The result of this singular graph is empirical and only holds for the BRE data examined here for ethylene, but it can be computed for other fuels, and we have shown singular curves hold,

$\tilde{\kappa}(l)$. It should be mentioned that multiple data points overlap in the figure, and do not obviously reveal the results of the collapsed data curve.

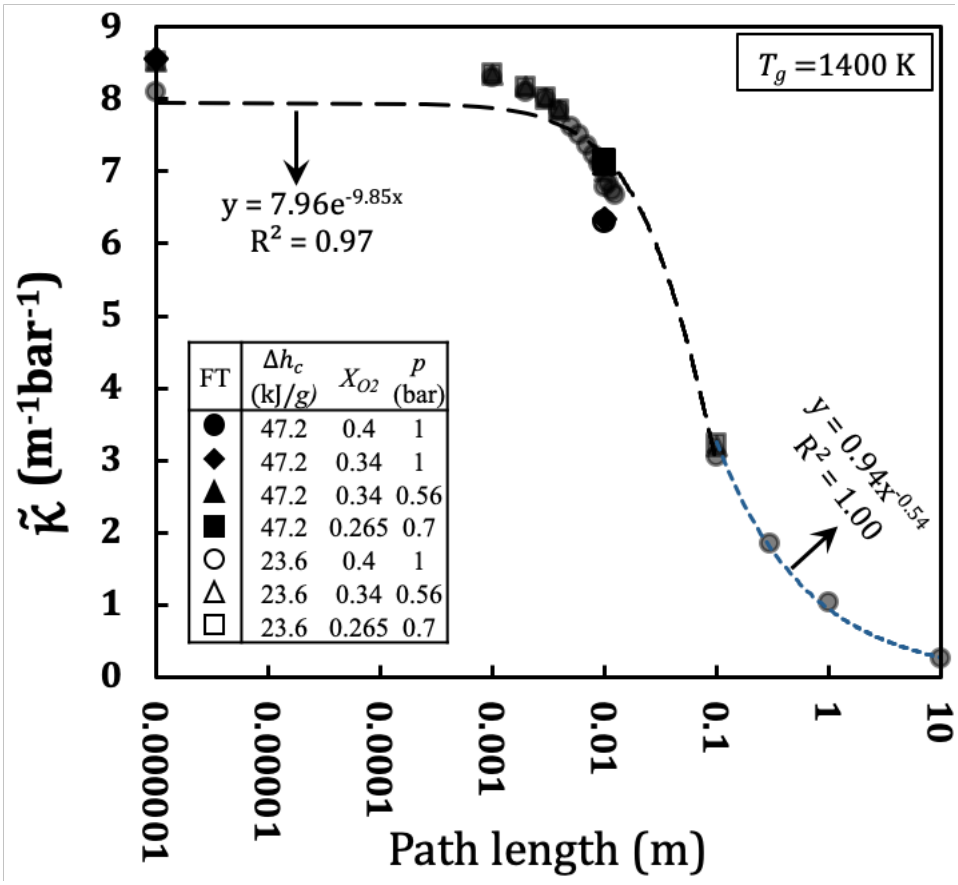

Figure 4.3. Absorption coefficients normalized by partial pressures of combustion products of ethylene

From Figure 4.3 we now have an empirical and convenient way to compute the needed emissivity term in Eq. (4.23). It should be pointed out that the path height used in this analysis was the flame height. It varies for the BRE data from about 5 to 50 mm, indicating a modified absorption coefficient of about 7.5 to 4.5 $(\text{m-bar})^{-1}$, respectively. This corresponds to emissivity in the range of 0.01 to 0.1, as shown in Figure 4.4 for the steady BRE data. Also Figure 4.4 reveals all of the steady data used in Figure 4.3 but is not evident due to overlapping symbols. If the experimental data of Figure 4.3 are used to compute the emissivity from the correlation of Figure 4.3, then those data are presented as shown in Figure 4.4. For high oxygen and pressures the flames

can survive with emissivities as high as 0.09 and flame heights of 40 mm, but for lower oxygen and pressures the emissivities are lower: 0.01 to 0.04.

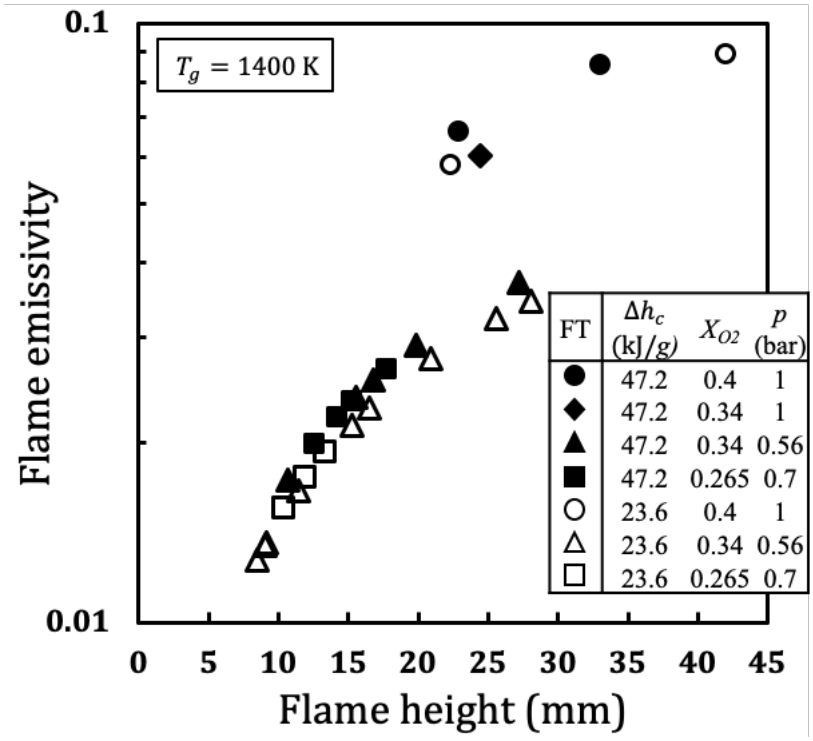

Figure 4.4. BRE flames emissivity vs. fuel mixture mass flux

The absorption coefficient can be computed from the fitted Eqns. (4.35 and 4.36)

$$\begin{cases} \tilde{\kappa}(\mathrm{m^{-1}bar^{-1}}) = 7.96e^{-9.85x_f} \; for \; x_f \leq 0.1 \; \mathrm{m} \\ \tilde{\kappa}(\mathrm{m^{-1}bar^{-1}}) = 0.94x_f^{-0.54} \; for \; x_f > 0.1 \; \mathrm{m} \end{cases} \tag{4.35}$$

$$\kappa(m^{-1}) = \left\{ \frac{4}{2 + 2 + 3\left(\frac{1 - X_O}{X_O}\right) + \frac{1 - X_{C_2H_4}}{X_{C_2H_4}}} \right\} p(bar).\tilde{\kappa}(m^{-1}bar^{-1}) \tag{4.36}$$

4.7 Correlation result

All the terms in Eq. (33) for Ω can now be computed as known quantities. The accuracy of the correlation is now explicitly demonstrated in the plot for steady experimental data as shown in Figure 4.5 where the flame radiation fraction is shown to approximate a singular function of Ω. A best-fit equation for the steady data is given as

$$X_r = 0.0633 \ln(\Omega) + 0.452 \tag{4.37}$$

This result together with Figure 4.3, now allow a full prediction of the microgravity steady burning. Let us examine this process and its accuracy.

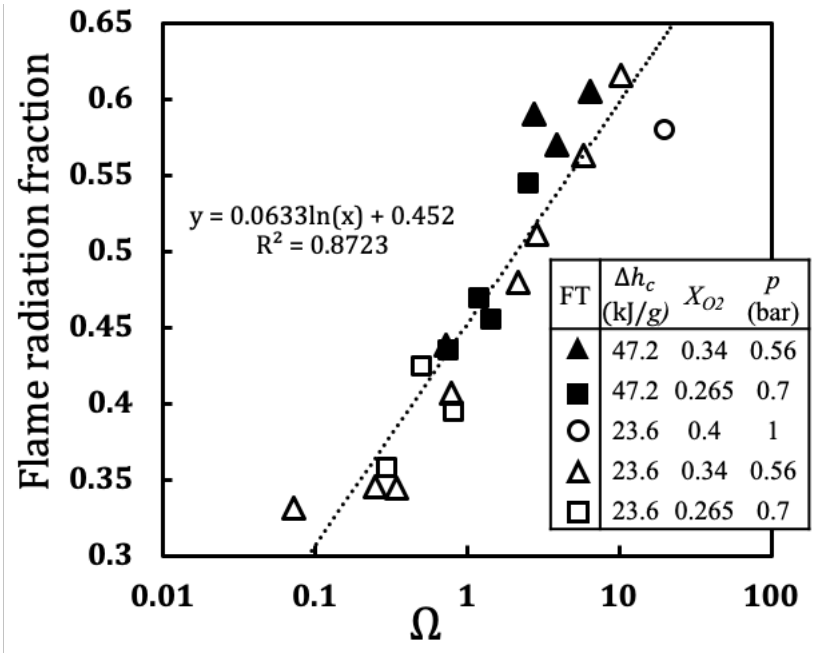

Figure 4.5. Radiant fraction correlation

The steady theory [49], Eq. (4.18), allows the computation of flame height for a given burner radius in terms of k/c_p, S and oxygen mass fraction of the atmosphere. This is done for properties of nitrogen at 1400 K. Figure 4.3 and Eq. (4.37) allow the computation of the flame radiation fraction for steady flames. Figure 4.6 shows the prediction of the flame radiation fraction with the experimental measurements. The prediction is within 10 % of the experiment.

Now additional quantities can be computed; namely, the flame temperature Eq. (4.15) and the convective flame heat flux Eqns. (4.16, 4.17). An estimation of the flame radiative heat flux is also needed to complete the theoretical determination of the heats of gasification that correspond to steady microgravity burning.

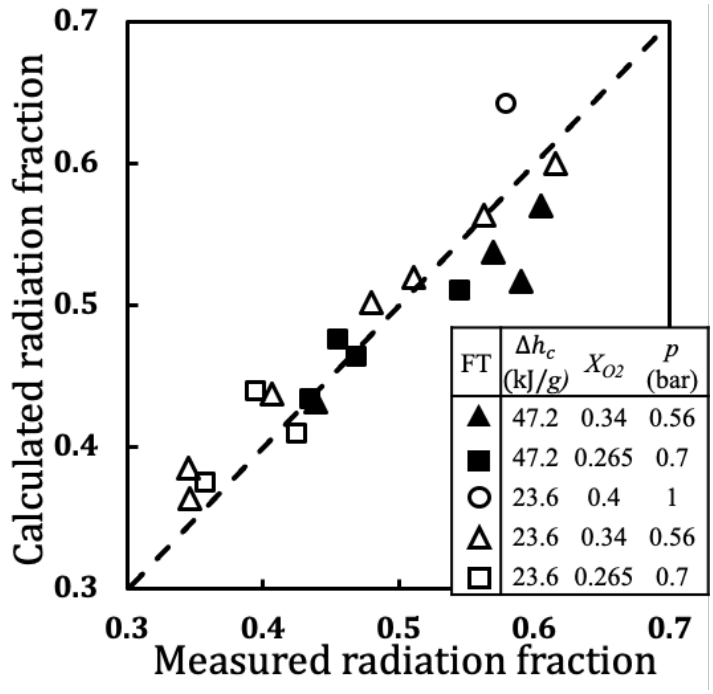

Figure 4.6. Calculated vs. measured radiant fraction

4.8 Flame temperature as a measure of extinction

Given now the flame radiative fraction, the flame temperature can be computed from Eq. (4.15). This is key to determining if the flame can survive. The extinction of a diffusion flame is commonly governed by the Damkohler number, as the ratio of the time for diffusion divided by the time for the chemical reaction. More completely it is controlled by the energy release of the chemical reaction and the heat loss from the system by both diffusion and radiation. In all cases the flame temperature is most critical as it governs all of these processes. The flame temperature can be computed from Eq. (4.15). It is well known that the flame cannot survive below a critical temperature [67,75,76,85–91]. This has been examined in References [75,76] using the same type

of burner in normal gravity for a variety of gaseous fuels relying on flame temperature to predict extinction. The flame temperature becomes a surrogate for the Damkohler number, and in this case addresses both diffusive and radiative heat losses as described by Eq. (4.13). In normal gravity for buoyancy driven flames a critical temperature of 1600 K is accepted in the literature [67,75,76]. It is known that the critical flame temperature is a function of the local flame strain rate [85,90,91] where 1600 K corresponds to about a strain rate of 10 s^{-1}, and 1100 K to a strain rate of 1 s^{-1}. The former is used for purely buoyant flames in 1-g, and the latter is commonly used in microgravity as an extinction criterion [85–91]. Figure 4.7 shows the computed values of flame temperature for the ISS steady data [51] where the radiation fraction is predicted for all of the steady data (Figure 4.6). The data points with lower heats of combustion have higher flame temperature because the flames radiation fraction varies inversely with the heat of combustion. We will examine these trends more carefully later using the predictive model in a more appropriate display. For now, it is clear from Figure 4.7 that all the steady results theoretically correspond to flame temperatures above 1100 K. This is now a straightforward predictive tool to assess whether steady burning in microgravity can occur.

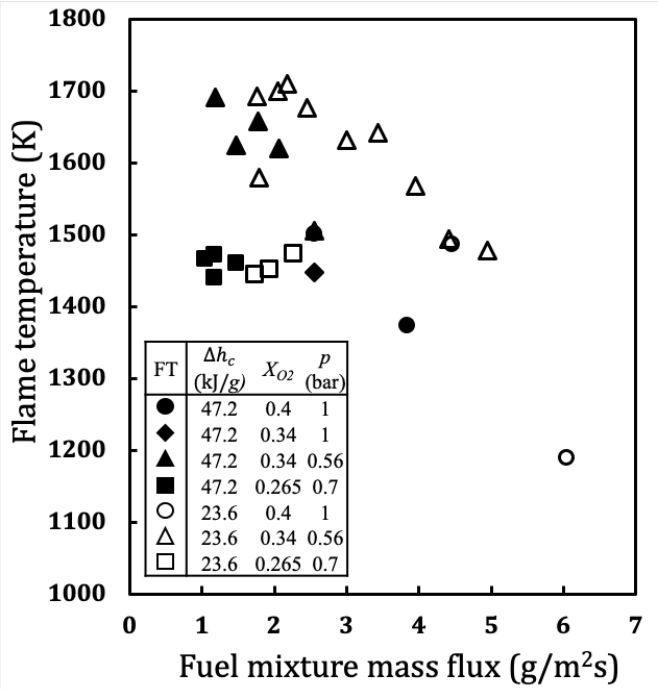

Figure 4.7. Flame temperature as a measure of extinction based on calculated radiant fraction

4.9 Prediction of heat flux

Now that we can compute the flame radiation fraction from known quantities with respect to the fuel and atmosphere, the convective and radiative components of the flame hat flux can be estimated.

4.9.1 Convective heat flux

The convective heat flux follows from the purely diffusive solution, but with the radiation loss accounted for now by reducing the heat of combustion according to the fraction of energy remaining in the flame system. The equation is repeated here for continuity.

$$\overline{\dot{q}_c''} = \left(\frac{4k}{\pi R c_p}\right)\left\{\frac{\lambda}{e^{\lambda}-1}\right\}\left[\frac{\Delta h_c(1-X_r)Y_{O,\infty}}{S} - c_p(T_s - T_\infty)\right] \tag{4.38}$$

It depends primarily on the properties k/c_p, the radiant fraction, the mass flux, and the atmospheric oxygen concentration. It also depends on pressure through X_r. The properties here are evaluated for nitrogen at 350 K. Again, this choice is by optimization and judgment, and might be justified as the convective heat flux is due to the gradient of temperature at the relatively cold wall of the burner. Figure 4.8 shows this computed convective heat flux compared to the net flame heat flux measured for the steady data set. The experimental data are the arithmetic average of two-point measurements on the burner surface as described for the experimental apparatus in ref [51]. The difference with the computed convection could be attributed to the flame's radiative component. Most of the convective prediction is about 50 % lower than the total measured net heat flux.

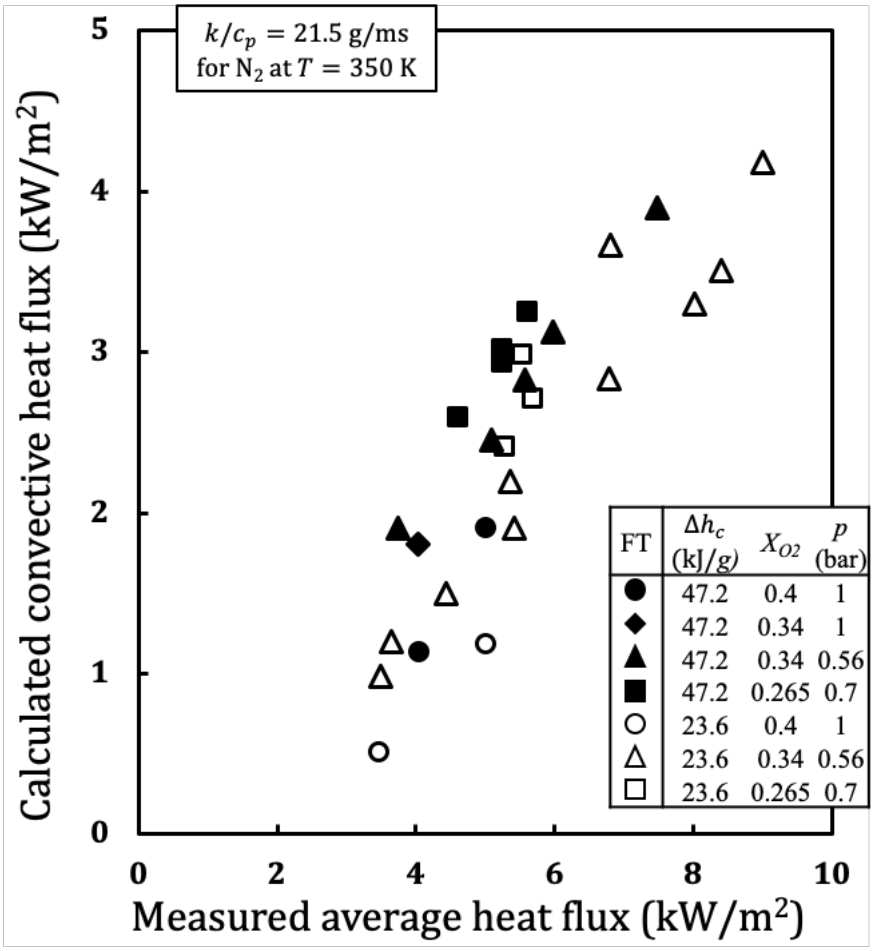

Figure 4.8. Calculated convective heat flux compared to the average net flame heat flux based on calculated radiant fraction

4.9.2 Flame incident radiative heat flux

We now construct a model for the flame radiative heat flux consistent with the flame radiation fraction predictable to us. Half of the radiation leaving the gases engulfing the flame goes either towards or away from the burner surface. Although the radiation comes from a gas volume region around the flame, the exchange with the burner surface is assumed to act on view factor principles, as if the radiation comes only from the flame surface (optically thin flame sheet is assumed). Consider the thin flame sheet and estimate the flame sheet surface area and utilizing the radiation view factor algebra with the reciprocity rule. Then one can obtain an estimation of the average radiative heat flux that impinges onto the burner surface. The view factor of the flame (*f*) with respect to the burner surface (*s*), $F_{s\to f}$,is close to unity because the flame mostly covers over the surface. In some cases, the flame stands off a distance δ_f from the surface reducing this view factor slightly. The approximate view factor is estimated from Eq. (4.39).

$$F_{s\to f} = 1 - \frac{\arctan\left(\delta_f / r_f\right)}{\pi} \tag{4.39}$$

We will consider δ_f small and negligible. The view factor from the flame to the burner is now given by reciprocity rule (Eq. (4.40)):

$$F_{f\to s} = \frac{F_{s\to f}\, A_s}{A_f} \tag{4.40}$$

And the flame sheet surface area, A_f, is estimated by assuming a half ellipsoid shape for the flame and that area is calculated by Eq. (4.41).

$$A_f = \left(\frac{2\pi\left(r_f^{3.2} + 2\left(r_f x_f\right)^{1.6}\right)}{3}\right)^{\frac{1}{1.6}} \tag{4.41}$$

The flame incident radiative heat rate to the burner surface is now given as the view factor to the surface times ½ the energy radiated away from the flame. The corresponding heat flux over the circular burner surface of radius, *R*, is then found as shown by Eq. (4.42).

$$\overline{\dot{q}''_{f,r}} = \frac{F_{f\to s}\dot{Q}_r/2}{\pi R^2} = \frac{F_{f\to s} X_r \dot{m}'' \Delta h_c}{2} \tag{4.42}$$

The results for the computed radiation heat flux are compared to the average of the measured heat flux by two heat flux sensors in Figure 4.9. The computed radiation flux to the burner surface is seen to be nearly equal to the measured total heat flux for low heat flux but as low as 1/3 for higher overall heat fluxes. Next, we can now see how the computed net heat flux compares to that measured.

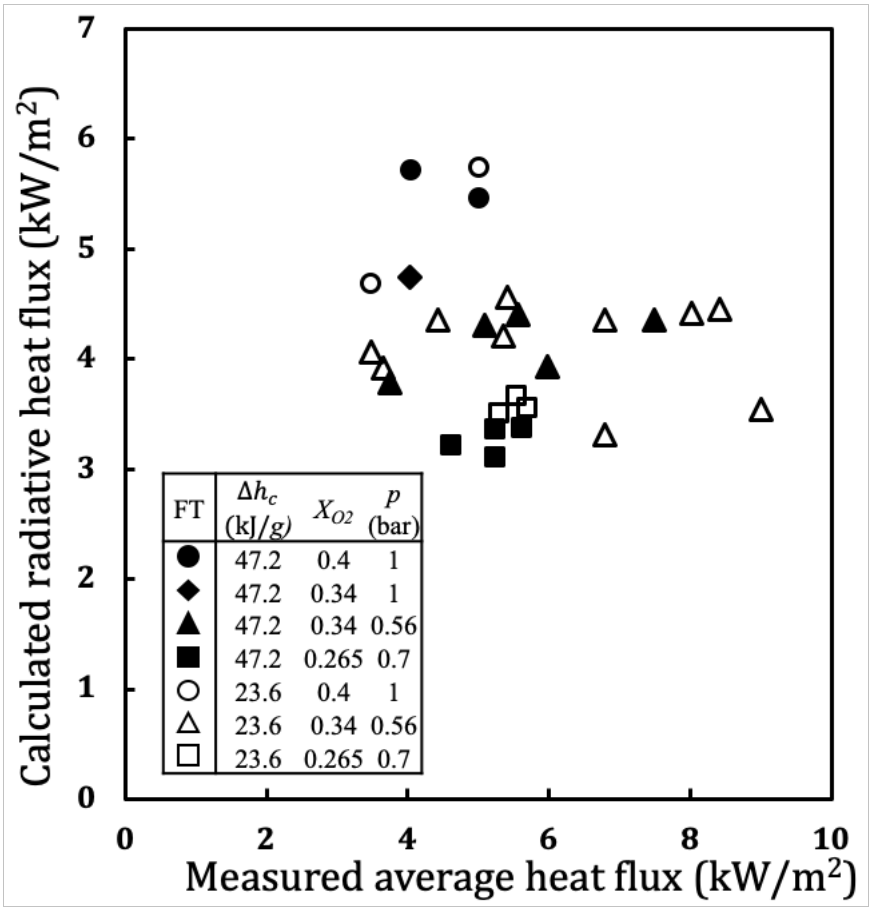

Figure 4.9. Calculated flame radiative heat flux compared to the average net flame heat flux based on calculated radiant fraction

4.9.3 Net heat flux to the burner

The net flame heat flux to the burner can be computed from Eq. (4.9) with the re-radiation component given as

$$\dot{q}''_{rr} = \varepsilon_s \sigma (T_s^4 - T_\infty^4) \tag{4.43}$$

where $\varepsilon_s = 1$ [61] and $\dot{q}''_{rr}$ varies from 0.14 to 1 kW/m^2 for all of the experimental data based on the direct measurement of the surface temperature. The measured surfaces temperatures are generally below 100 ºC.

The net heat flux depends primarily on flame height, mass flux and heat of combustion. There is a pressure effect through the flame emissivity. The results for the steady net heat flux data are shown in Figures 4.10 and 4.11 that are based on measured calorimeter net heat flux [48] and arithmetic average of the two local sensors on the burner surface [51], respectively. As one sees the calorimeter values are higher than the average of the two-point values [51]. We have high confidence in the point values, but recognize an arithmetic average is assumed. The calorimeter measure was supposed to capture the true integrated average of the heat transfer, but its operation was compromised, and a theoretical correction had to be imposed. Its confidence is lower than point sensor result. In Figure 4.11 the prediction is within about 20 % for most of the averaged point data. We think we have the essence of the flame radiative and convective components understood based on this result.

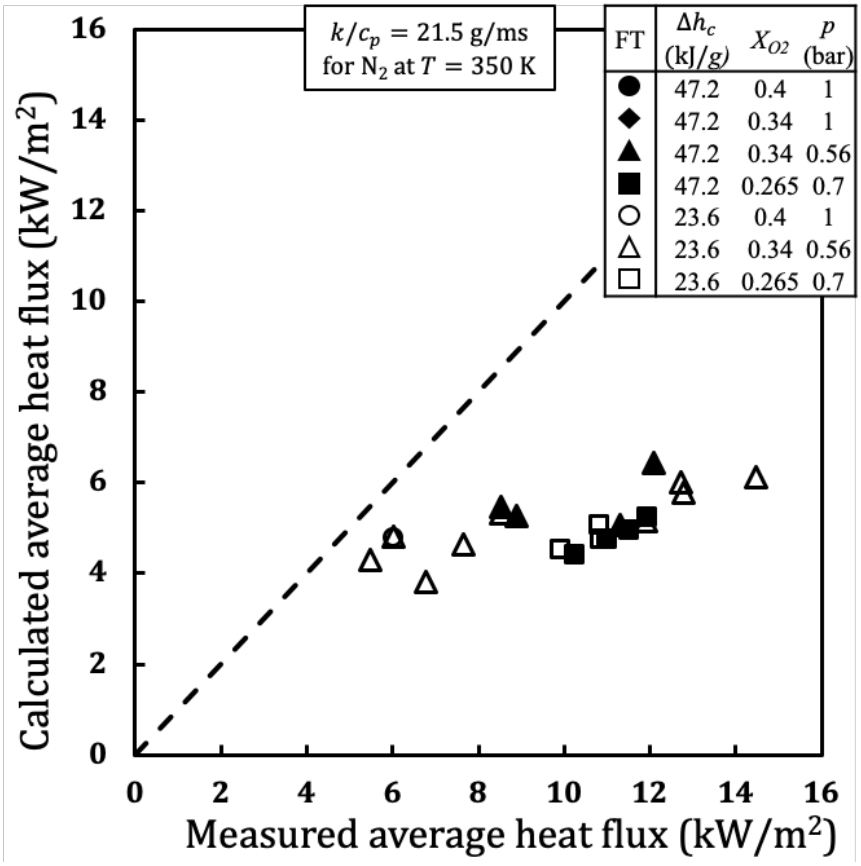

Figure 4.10. calculated average heat flux vs. measured average heat flux from calorimeter $\left(\overline{\dot{q}''_{conv}} + \overline{\dot{q}''_{f,r}} - \dot{q}''_{rr}\right)$

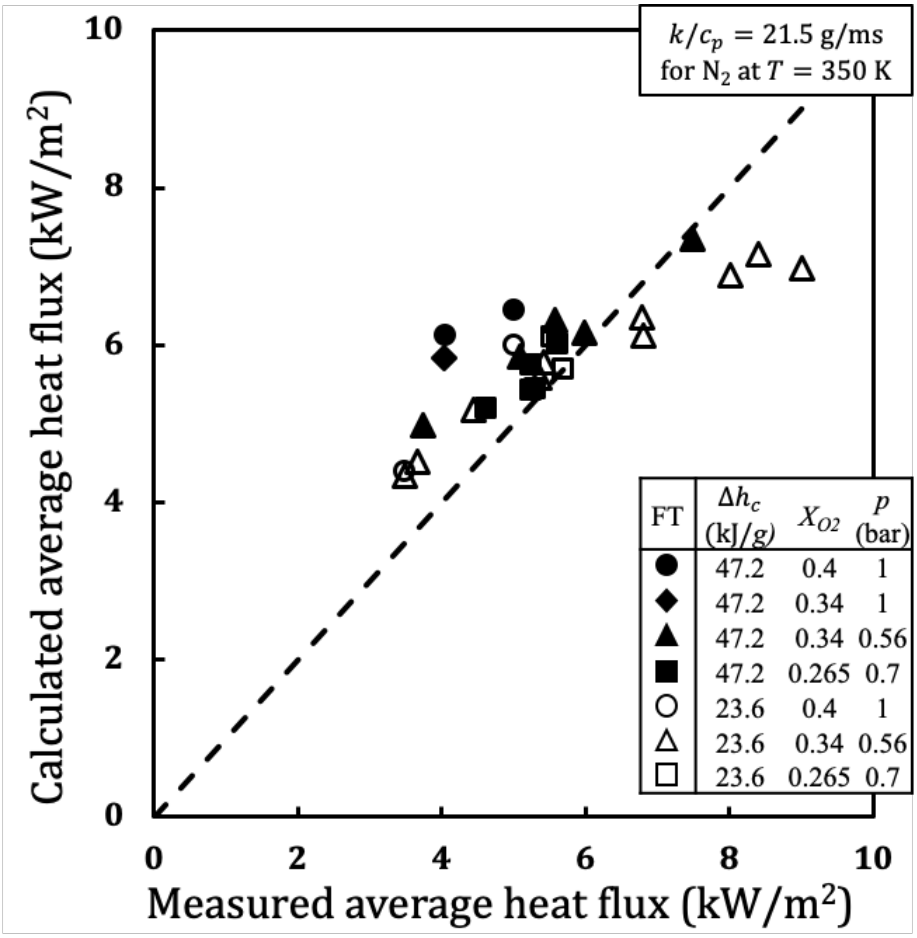

Figure 4.11. calculated average heat flux vs. measured average heat flux from arithmetic average of the two heat flux sensors $\left(\overline{\dot{q}''_{conv}} + \overline{\dot{q}''_{f,r}} - \dot{q}''_{rr}\right)$

4.10 Overall general predictive process and illustration

In this section the solution computations will be explored to show the effect of pressure, oxygen concentration, and heat of combustion. Values chosen are motivated by the experimental conditions. In summary, the following conditions are selected:

- Atmospheric pressure: 0.56 and 1 bar
- Atmospheric oxygen mole fraction: 021, 0.265 0.34 and 0.40, representing NASA considered atmospheres [65,92].
- Material heat of combustion: 23.6 and 47.2 kJ/g, representing a wide range of plastics.

- Material vaporization temperature: 80 ºC (Later 350 ºC is considered.)
- Also, properties are chosen for nitrogen at 1400 K in computing flame size, k/c_p = 65 g/s-m: and 350 K in computing convective heat flux, k/c_p = 21.5 g/s-m.

The computation process proceeds as follows:

1. The atmospheric conditions are specified for a given fuel-nitrogen mixture. This will fix the mass flux and heat of combustion.
2. The flame height is computed, Eq. (4.18), then the absorption coefficient, Eqns. (4.35, 4.36), non-dimensional radiation term "Ω" from Eq. (4.33) and the flame radiation fraction, Eq. (4.37).
3. The flame temperature is then computed from Eq. (4.15). If it is above 1100 K, then the flame is considered as a stable steady flame.
4. The convective and radiative heat fluxes can then be computed by Eqn. (4.16 and 4.42).

4.11 Flame Temperature

Flame temperature is key, as it will theoretically indicate cases above 1100 K that are expected to be steady [85–91]. This allows a flammability mapping to be made to ultimately consider real solid fuel ranges for heat of combustion and heat of gasification properties that indicate the possibility of steady burning in microgravity at specific atmospheric conditions of oxygen concentration and pressure. (Of course, the solid fuel's vaporization temperature needs to also be accounted for, but as its effect is relatively small, it will be fixed at a small value of 80 ºC, representative of the experiments.) Figure 12 shows the results. Actually, the flame radiative fraction must be computed first, before the flame temperature is computed. In doing so, all the values of radiation fraction are used in computing the flame temperature, but the results in Figure 12 are terminated at 1100 K. In subsequent computations the results will reflect those conditions above 1100 K.

It is striking in Figure 12 that the lower atmospheric pressure yields a wider range of burning conditions. This suggests that lower pressure favors burning. Some overall observations follow flame temperature, greater than 1100 K and indicates steady burning

- Happens more likely at low pressure
- Happens more likely at lower heats of combustion (because X_r increases)
- Happens more likely at higher oxygen concentrations
- Happens more likely at higher surface temperatures (But we might explore this effect later).

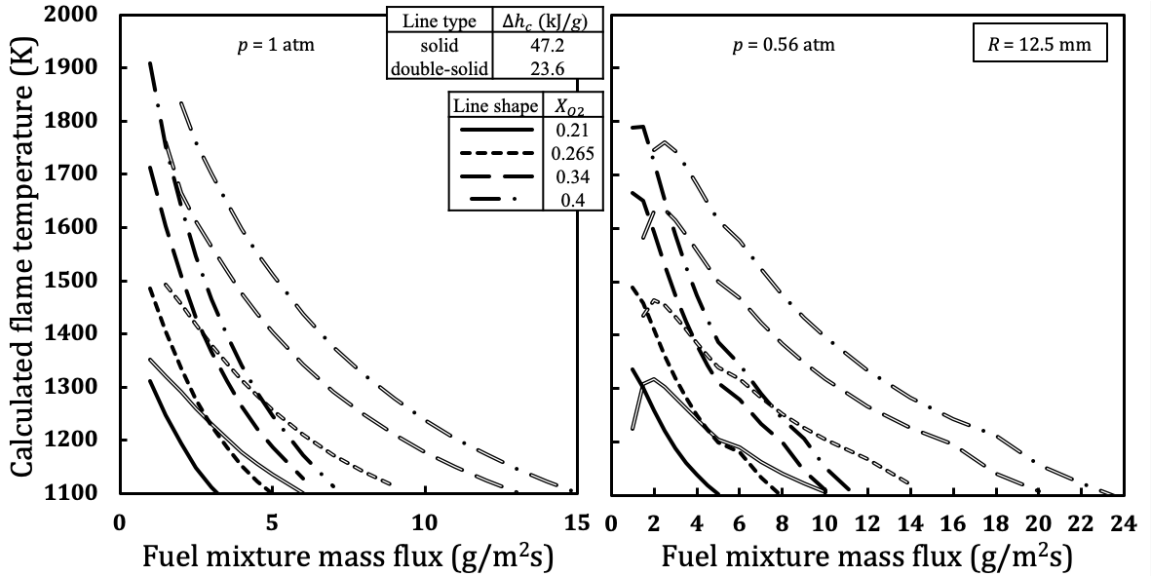

Figure 4.12. Calculated flame temperature vs. mass flux for 25 mm burner and different oxygen mole fractions and p = 1 atm (Left) p = 0.5 atm (Right)

4.12 Flame Radiation Fraction

The flame radiation fraction can be computed from the given parameters and the results are shown in Figure 4.13. Steady experimental data are also included in the figure. Here the results are shown only for the stable flames with flame temperatures above 1100 K. Also, the experimental results are included to show the trends are in harmony with the theory, and the theory is extrapolated to higher steady mass fluxes. The complete set of experimental data points are shown in Figure 4.14 [51]. The trends are similar in magnitude for the low mass flux, but the data do not show the theoretical leveling off at higher mass fluxes The lower pressure atmosphere can support much higher burning rates. The results even show burning can exist at 21 % oxygen for very low mass flux values.

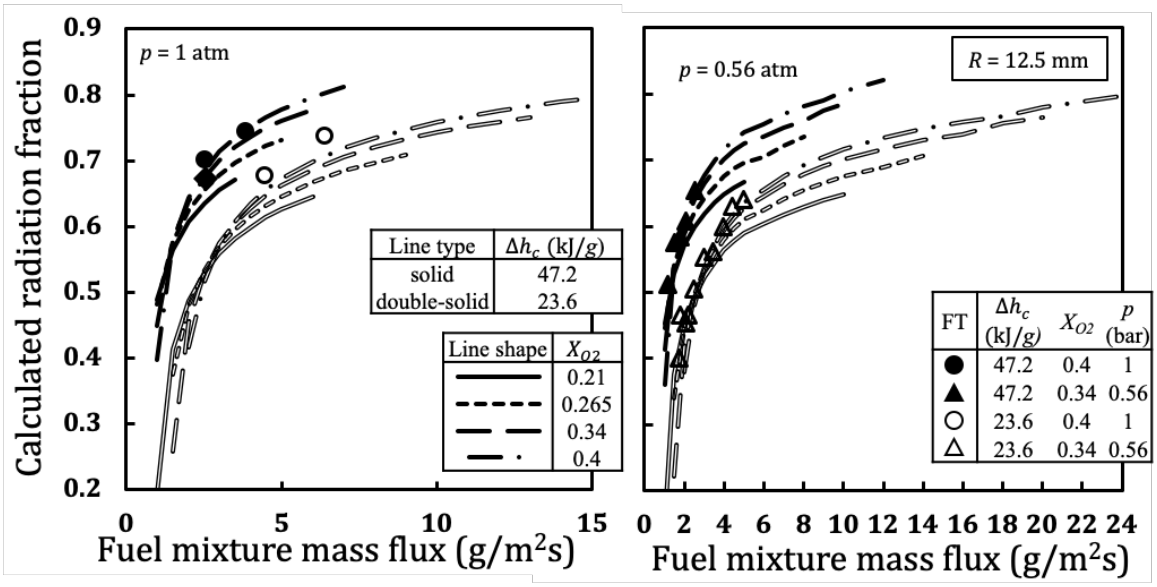

Figure 4.13. Calculated flame radiant fraction vs. mass flux for 25 mm burner and different oxygen mole fractions and p = 1 atm (Left) p = 0.56 atm (Right)

Some qualitative results can be discerned.

Flame Radiative Fraction:

- Increases sharply with mass flux, then levels off
- Can support higher burning mass flux at the lower pressure
- Increases with oxygen mole fraction except for very low mass flux
- Decreases with heat of combustion by about 50 % to 15 % as the burning mass flux increases where the heat of combustion drops by from about 47.2 to 23.6 kJ/g.

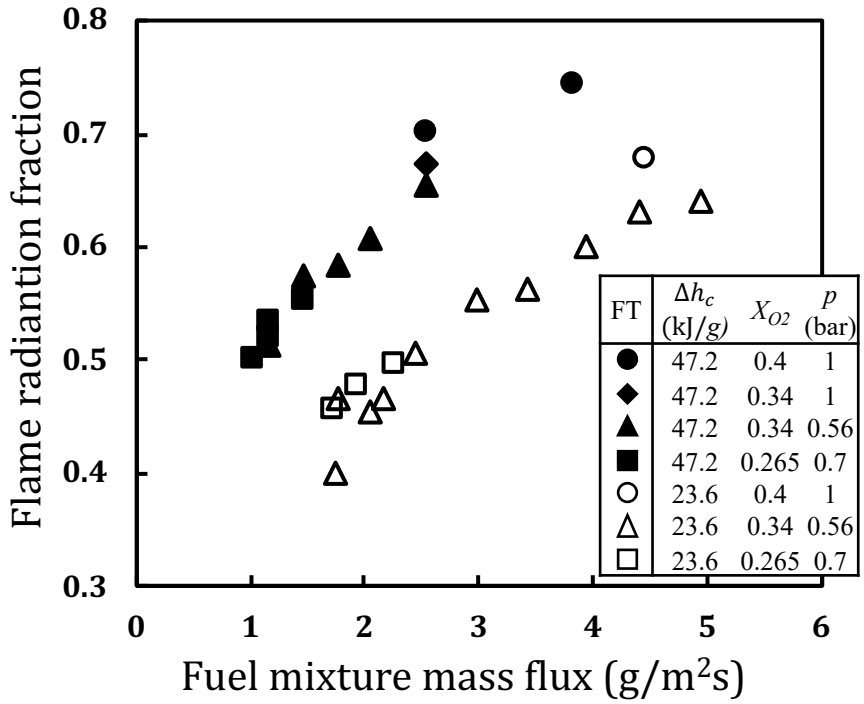

Figure 4.14. Measured radiant fraction vs. fuel mixture mass flux for 25 mm burner

4.13 Flame size

Here the flame height on the burner central-axis and the flame base radius are computed. The "*c*-correction" is used for the radius. The results are shown in Figure 4.15 along with some limited data. So, there is a pressure effect here as well, as bigger flames can exist at lower pressures. Figure 16 shows the complete steady flame height data over a similar range of conditions but note that it only ranges over 1 to 6 g/m^{2}s. The theory and the data are in harmony, but the theoretical plot reveals many more steady flame possibilities. It should be noted that experimental flames had a maximum flame height of about 40 mm, but theoretical flames at low pressure and high oxygen could extend to 120 mm. Some observations:

Flame size

- Increases with mass flux
- Decreases with oxygen concentration
- Increases with $S = \Delta h_c/\Delta h_{ox}$ or heat of combustion

- Bigger flames possible at lower pressure

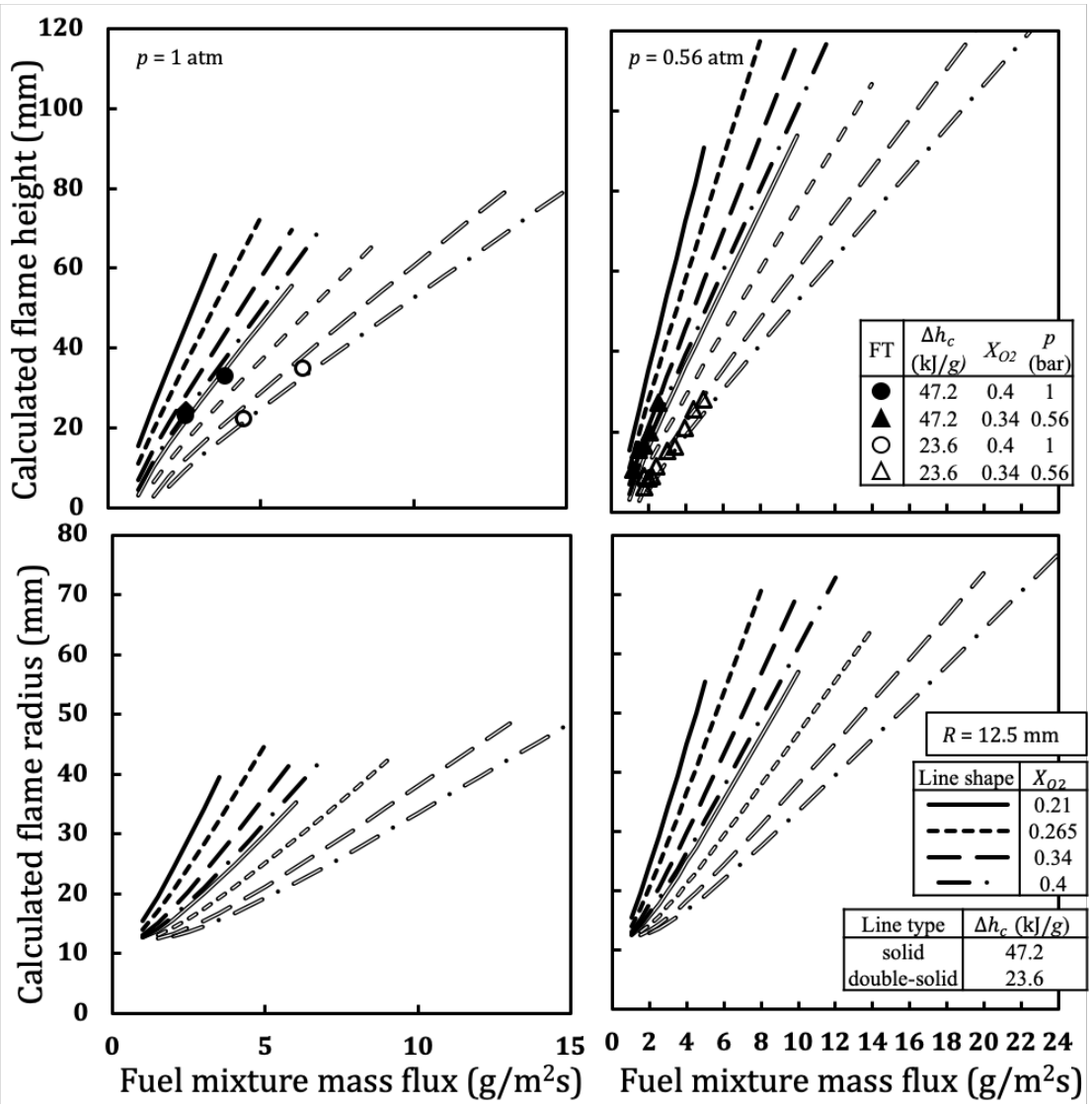

Figure 4.15. Calculated flame height vs. mass flux for 25 mm burner and different oxygen mole fractions (Top) Calculated flame radius vs. mass flux for different oxygen mole fractions (Bottom)

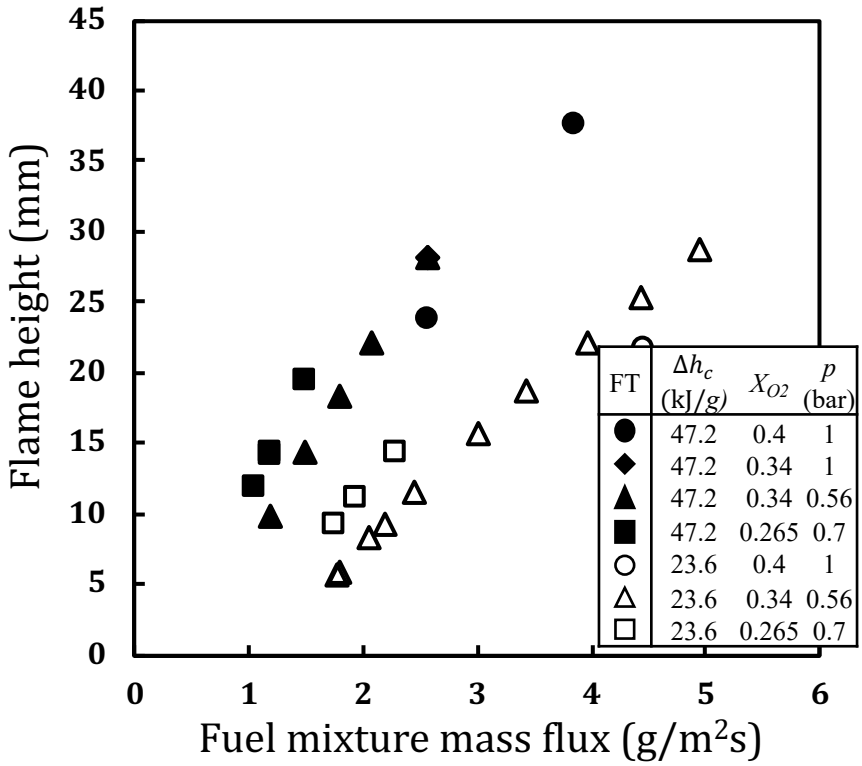

Figure 4.16. Measured flame height vs. fuel mixture mass flux for 25 mm burner

4.14 Calculated convective heat flux

The calculated convective heat flux is primarily affected by the radiation fraction, and thus through pressure. Figure 4.17 shows the theoretical results. The low-pressure flames can survive to higher mass fluxes. They decrease with mass burning rate and range from 10 to 0.1 kW/m^2, a very low value for Earth flames. Some observations:

Convective heat flux:

- Decreases with mass flux
- Increases with ambient oxygen mole fraction
- Decreases with heat of combustion

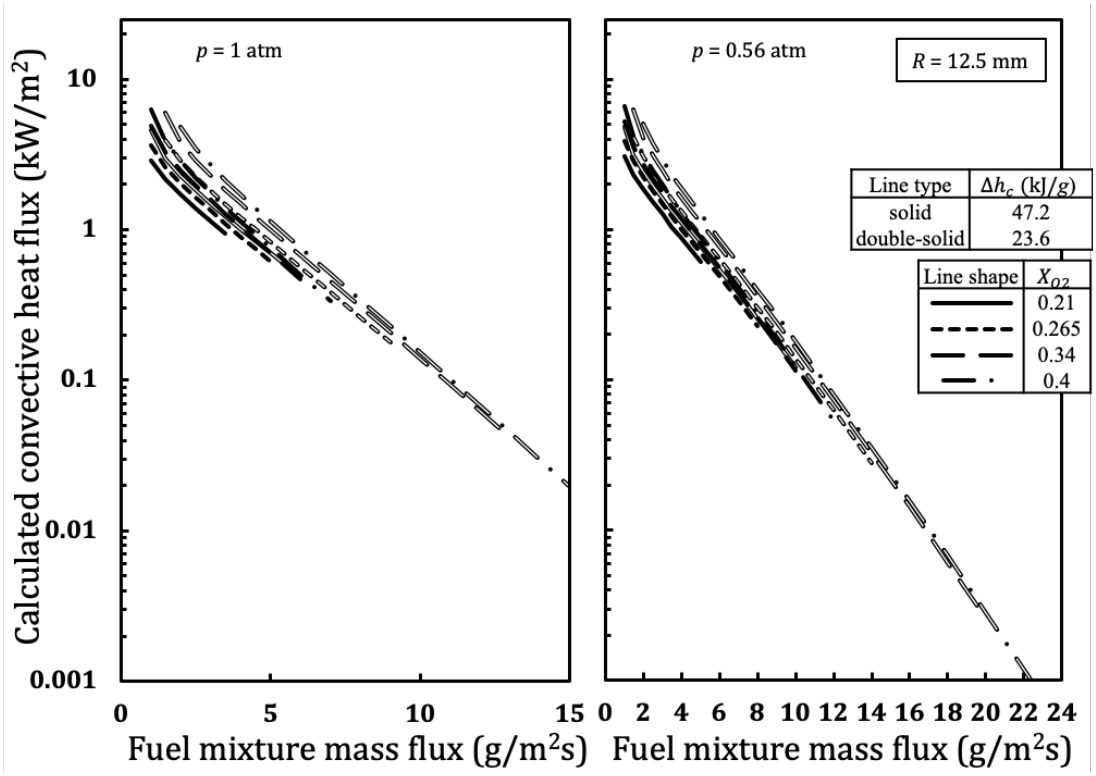

Figure 4.17. Calculated flame convective heat flux vs. mass flux for 25 mm burner and different oxygen mole fractions and p = 1 atm (Left) p = 0.56 atm (Right)

4.15 Calculated radiative heat flux

The radiative heat flux depends primarily on the flame radiative fraction and the flame size. Figure 4.18 shows the theoretical results. The radiation drops rapidly with burning rate.

Some observations similar to convection:

Radiative heat flux:

- Decreases with mass flux
- Increases with ambient oxygen mole fraction
- Decreases with heat of combustion
- Has similar pressure dependence, except lower ambient pressure allows longer burn time

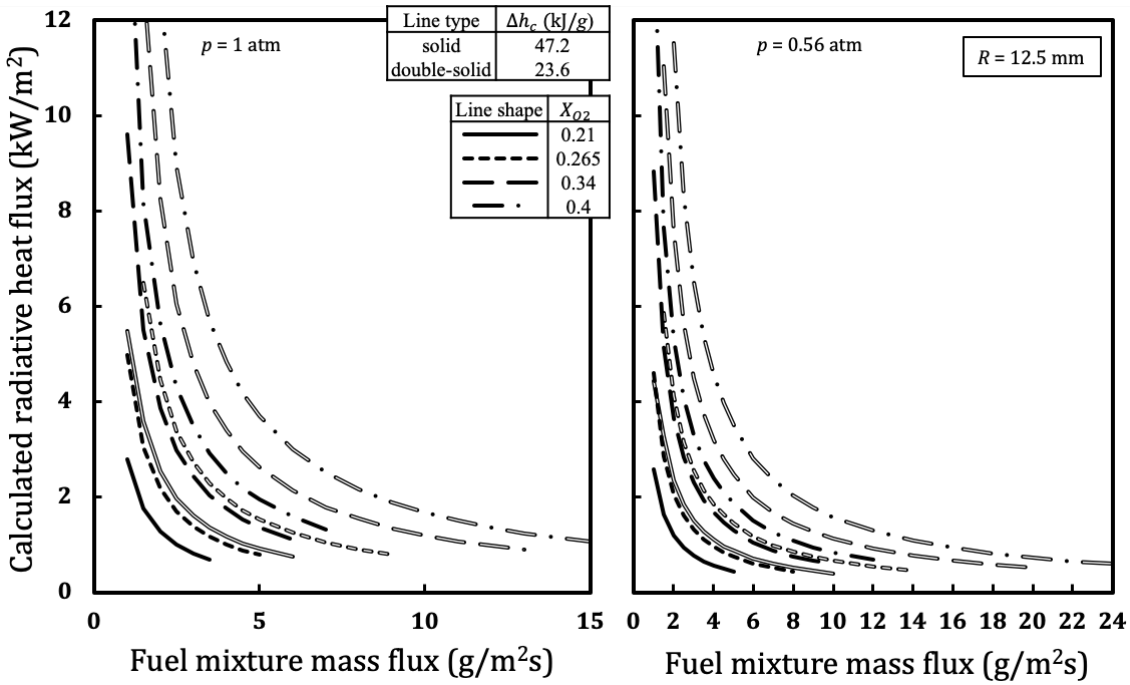

Figure 4.18. Calculated radiative heat flux vs. mass flux for 25 mm burner and different oxygen mole fractions and p = 1 atm (Left) p = 0.56 atm (Right)

4.16 Heat of gasification, *L*

The key parameter after all this analysis is the heat of gasification. While an ideal quantity for the steady burning of thick solids with evaporative pyrolysis characteristic, it serves as an approximate property that indicates the ability of a material to release flammable gases upon heating. It is computed from Eq. (4.8) where the burning mass lux is specified, and the heat fluxes can be computed from the steady flame theory. Typical non-charring plastics have *L* values of 2 to 3, with charring materials effectively higher. So applicable realistic solids might range from 1 to 5 [67,74].

4.16.1 Heat of Gasification dependence on burning rate

Figure 4.19 gives results where the surface vaporization temperature was representative of the experimental burner emulator, 80 ºC with some representative experimental data. Here *L* increases with oxygen and decreases with heat of combustion. A plot of heat of combustion vs

heat of gasification for the various atmospheric conditions over the range L: 1 to 5 kJ/g and Δh_c: 23.6 to 47.2 kJ /g would give a flammability mapping of what solids could burn in microgravity. Figure 20 shows how the complete steady data yielded the L plot. The data generally follow the theoretical trends for the effect of pressure, oxygen, and heat of combustion.

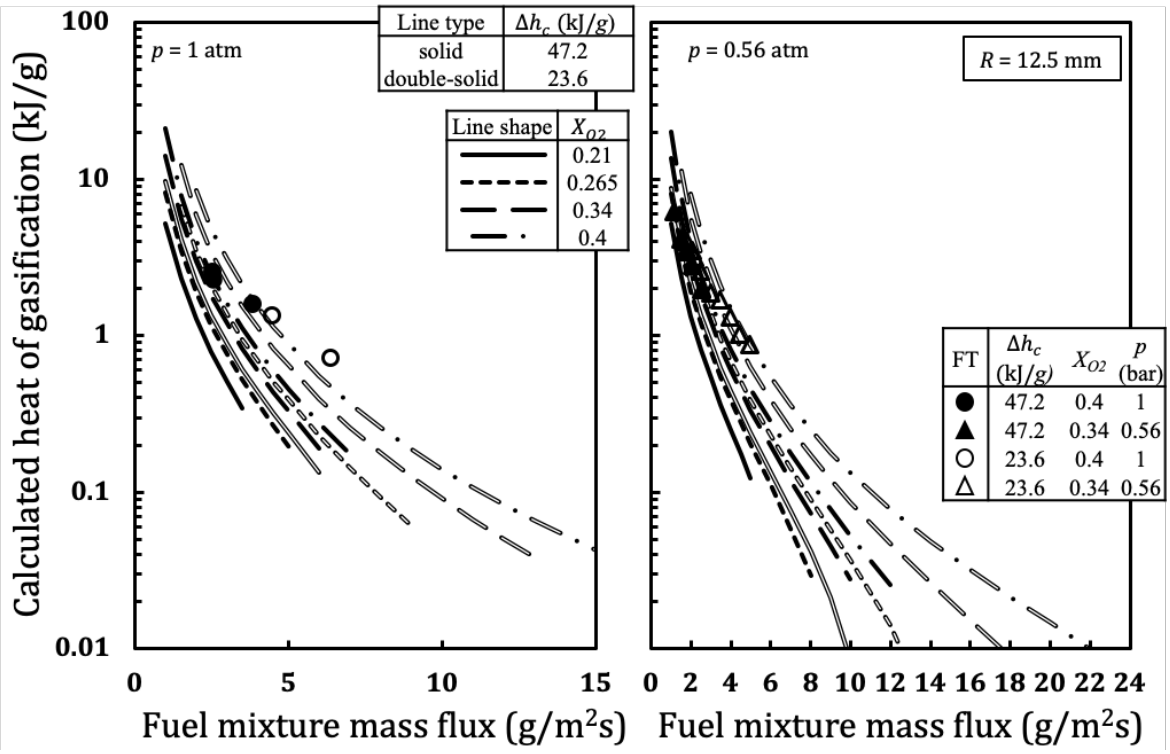

Figure 4.19. Calculated heats of gasification vs. mass flux for different oxygen mole fractions and p = 1 atm (Left) p = 0.56 atm (Right)

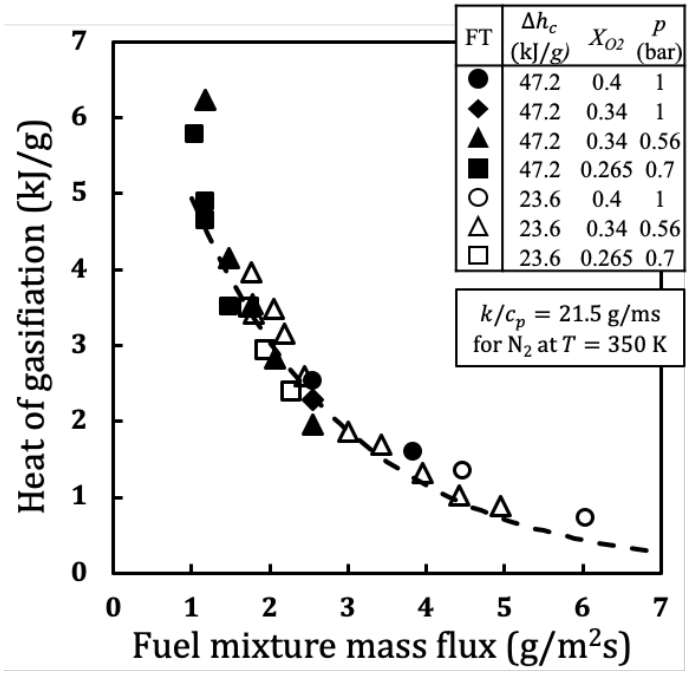

Figure 4.20. Heats of gasification based on calculated total average surface heat flux vs. experimental fuel mixture mass flux and ambient conditions (Dashed line indicates experimental results trend-line for steady flames)

4.16.2 Heat of Gasification dependence on surface burning temperature

Let us examine how a more realistic vaporization temperature might affect these results. A temperature representative of burning plastics is selected as 350 ºC for illustration. The surface temperature affects surface re-radiation heat flux and the net heat flux accordingly. Heat of gasification is decreased when surface temperature is increased for a given mass flux. Figure 4.21 gives these results. They are similar to Figure 4.19, but only are steady for a lower range of burning rates.

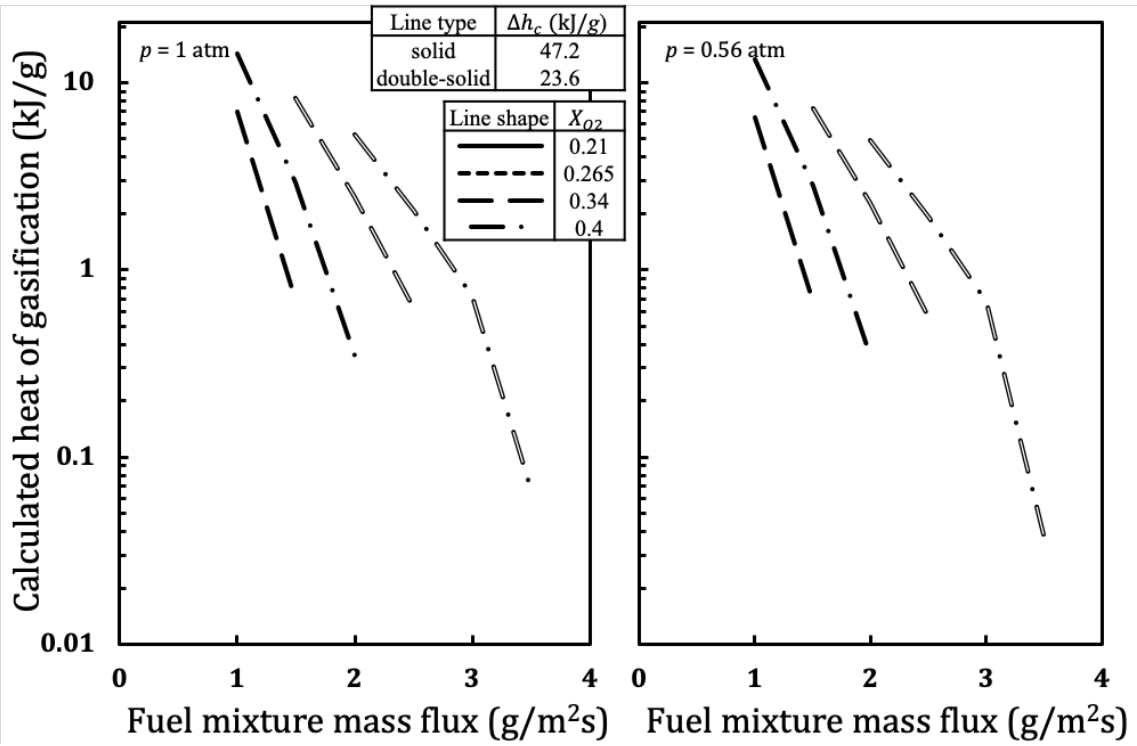

Figure 4.21. Calculated heats of gasification vs. mass flux for different oxygen mole fractions and p = 1 atm (Left) p = 0.5 atm (Right) for surface temperature of 350 ºC and surface diameter of 25 mm

4.16.3 Heat of Gasification dependence on fire diameter

Now examine the effect of the diameter of the burning material. The diameter is doubled twice from 25 mm to 50 mm to 100 mm. Figures 4.22 and 4.23 show the results. For the range of realistic L values, the effect of size does not significantly change the results. Indeed, a careful examination over the 25 to 100 mm range shows nearly the same results of L for mass flux over 1 to 5 g/m^{2}s. For a wide range of plastics, L values of 1 to 5 kJ/g and heats of combustion of 23.6 and 47.2 kJ/g can be representative.

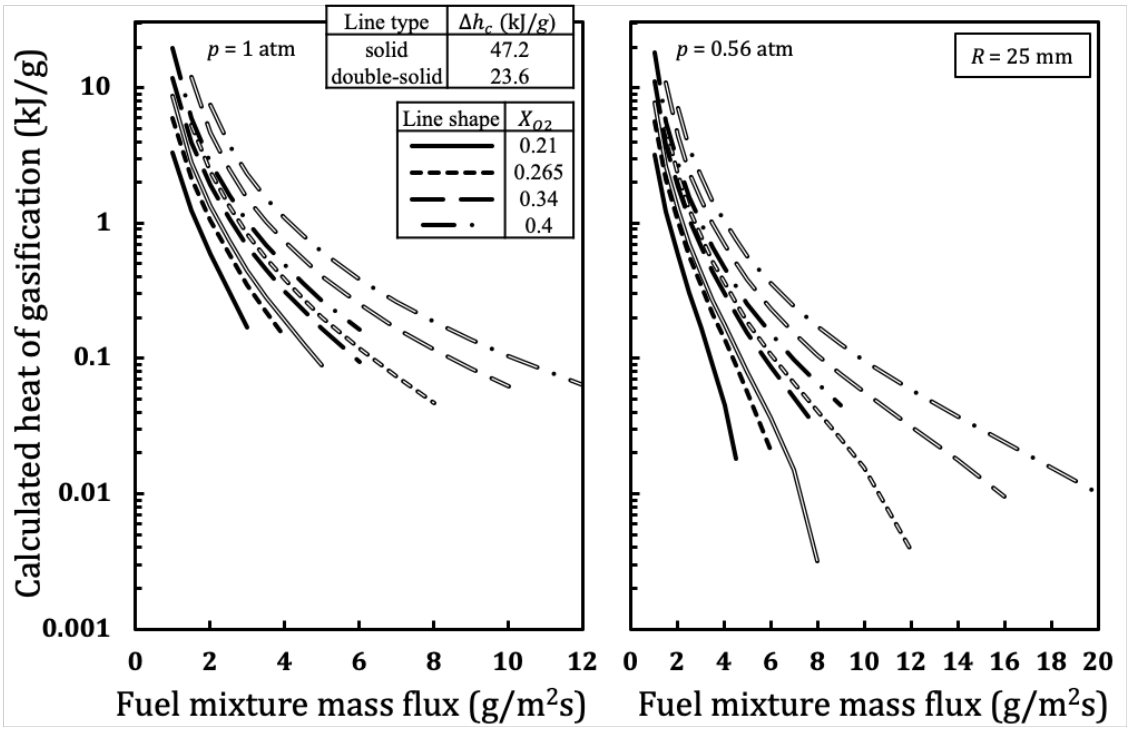

Figure 4.22. Calculated heats of gasification vs. mass flux for different oxygen mole fractions and p = 1 atm (Left) p = 0.5 atm (Right) for a burner of 50 mm in diameter

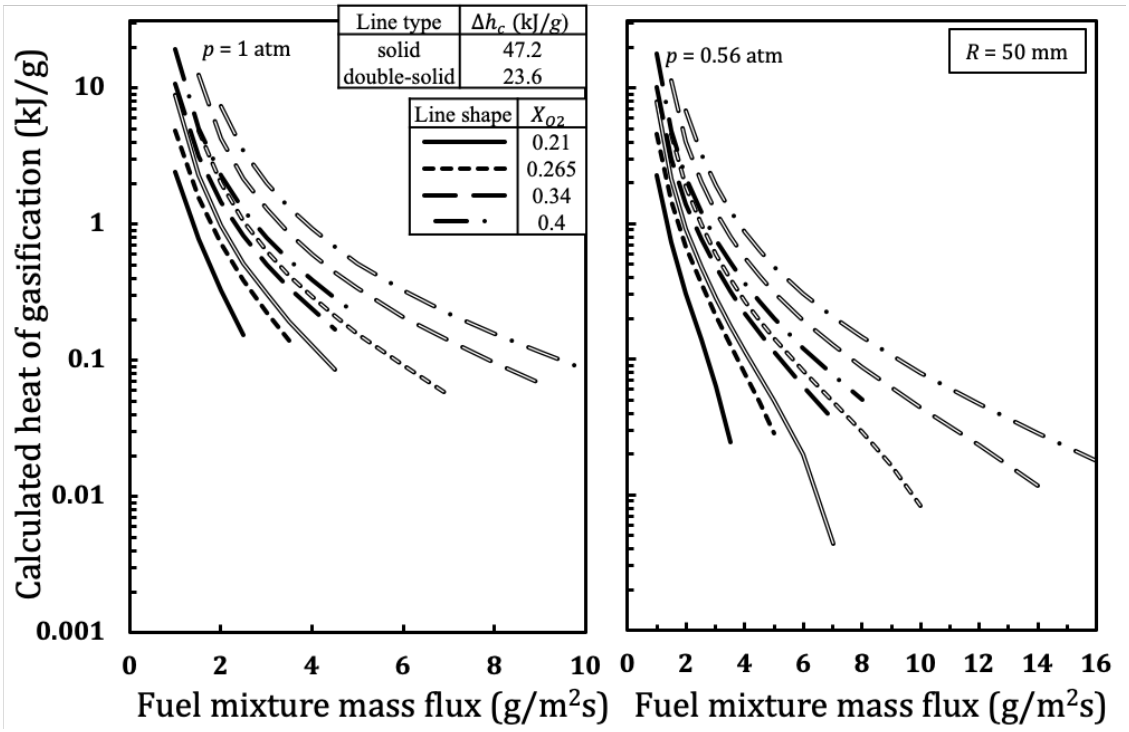

Figure 4.23. Calculated heats of gasification vs. mass flux for different oxygen mole fractions and p = 1 atm (Left) p = 0.5 atm (Right) for a burner of 100 mm in diameter

There is a subtle effect of size. The time to reach steady conditions is much longer as the burning diameter increases. The factor erfc $\left(\frac{\xi}{2\sqrt{\tau}}\right)$ controls the time for the flame to grow to its steady value, with that when erfc $\left(\frac{\xi}{2\sqrt{\tau}}\right) = 1$. If ξ is related to the flame height and considered of the O(1), then erfc (0.01) = 0.99.

$$\frac{1}{2\sqrt{\tau}} = 0.01 \; or \; \tau = 2500$$

$$\tau = \frac{D_\infty t}{R^2} \; , D_\infty = \frac{k}{\rho c_p}$$

$$\frac{D_\infty t}{R^2} = 2500 \, , \qquad D_\infty \; = \; 2.7 \; x \; 10^{-4} \; \mathrm{m^2/s}$$

Time to steady state = $10R^2$(mm)^2 at 99% steady

for R = 12.5 mm steady time is estimated as 1560 s; for 25 mm 6250 s; and for 50 mm 25000 s. These are astounding times, but this is math, and not physics. In practical terms for about 95 % of steady state, the

$$\text{Time to steady state} = 0.4R^2(\text{mm})^2 \text{ at 95 \% steady}$$

gives for R = 12.5 mm an effective estimated steady time of 63 s; for 25 mm 250 s; and for 50 mm 1000 s. In any event, the gas-phase transient in flame size depends strongly on the burning radius. However, the time governing the flame heat flux achieving steady conditions is much shorter. Experimental data is needed here to fully understand the effect of size on burning time.

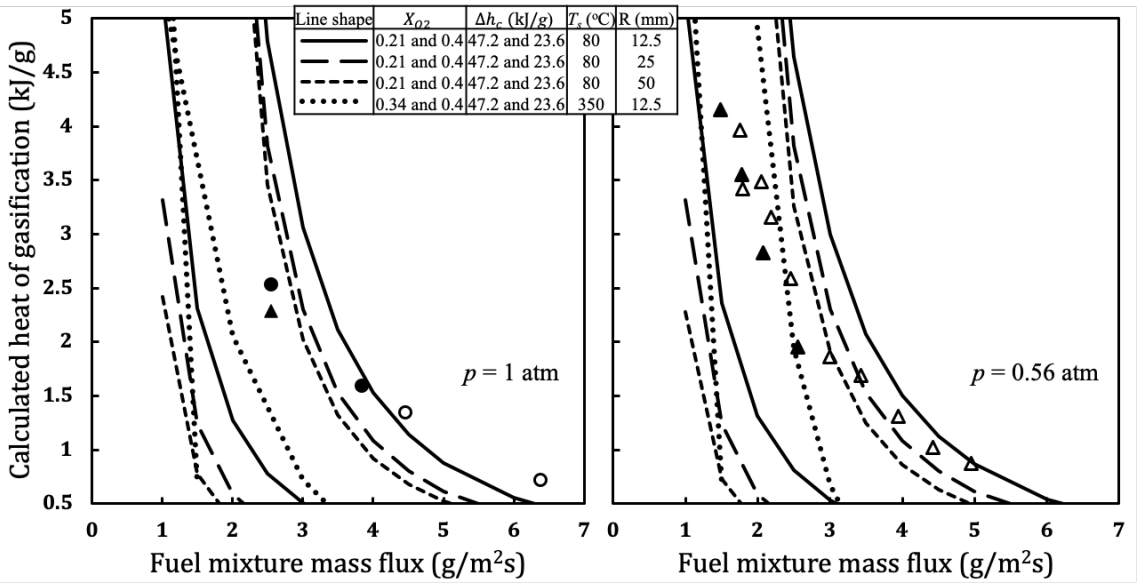

Figure 4.24. Heat of gasification composite for size (25, 50, 100 mm diameter), surface temperature (80 and 350 ºC), heat of combustion (47.2 and 23.6 kJ/g), and ambient conditions (0.56 and 1 bar ambient pressure; 0.21, 0.34 and 0.40 oxygen mole fractions)

A close examination of the theoretical and experimental results for the heat of gasification suggests some similarity for the results, especially over the range of realistic fuels in the range of 1 to 5 kJ/g. Figure 4.24 shows a composite for the extreme (maximum and minimum) curves for each of the three material sizes (12.5, 25 and 50 mm) and surface temperature of 350 ºC to bracket the results and to show this footprint. All the graphs, varying in pressure, oxygen, heat of combustion, surface temperature and size to 100 mm in diameter cover the same portion of the

results with the mass flux varying from about 1 to 5 g/m^{2}s. This is a remarkable result. It says that burning in microgravity for surfaces up to 100 mm in diameter will typically range from about 1 to 5 g/m^{2}s.

4.17 Chapter Summary

An analytical solution, based on classic diffusion flame theory, was used to analyze microgravity flames generated by a gaseous fuel-charged burner that emulates condensed-phase fuels burning. An empirical analysis based on flame radiation theory and measurements allowed us to correlate flame radiative loss fraction with a dimensionless parameter, Ω. The parameter includes the effects of ambient conditions (i.e., ambient pressure, oxygen mole fraction), fuel heat of combustion, surface temperature, and flame emissivity. (See Eqns. (4,18,32-36).) Since BRE flames in microgravity do not contain soot, it is assumed that flame emissivity only depends on carbon dioxide and water vapor. However, the empirical parameter Ω does depend on the fuel, and here only ethylene-nitrogen mixtures were examined. RADCAL was used at a nominal flame temperature (1400 K) to determine the emissivity for a given path length taken as the center flame height. It was shown that if the RADCAL output absorption coefficients is divided by sum of the partial pressures of radiating component combustion products, all data will collapse on an empirical curve that suggests it only varies with path length. The path length is taken as the center flame height calculated analytically. Being able to calculate radiation fraction allows us to compute flame temperature in which 1100 K is taken as a criterion for flame extinction [10–14]. It also allows calculation of convective heat flux with a radiation correction on the heat of combustion. The radiation heat flux is computed based on geometrical view factor analysis along with Xr to give the available radiant heat flux that impinges on the surface. The net heat flux composed of the algebraic sum of convective, radiative and re-radiation from surface allows the heat of gasification to be computed for a specified fuel-mixture mass flux. The effect of burner size and surface temperature (350 ºC that represents real fuels burning) are also investigated. It is shown that as burner diameter is increased, flame radiant fraction is increased and heats of gasification are decreased in an asymptotic-like behavior. Surface temperature introduces substantial change in heat of gasification in which re-radiation heat loss decreases the burning rates, i.e., Figures 19

and 21. However, external radiation can offset this effect, and increase the mass flux. As in Earth-based fires, external radiation is the key to massive fire growth; it is likely this can be an issue in microgravity as well. The analytical algorithm given in this paper has been shown to accurately predict steady conditions of burning for a surface of 25 mm diameter and has been examined for larger diameters. This analysis gives one a powerful analytical tool to predict the steady burning in microgravity as a function of fuel properties and ambient conditions.

Let us examine the trends suggested by the theoretical results in terms of ambient conditions, fuel properties, and surface diameter. Table 1 shows the increase (+) and decrease (-) trends for the key parameters of burning as a function of specified burning rate, pressure, oxygen atmosphere, and heat of combustion. Ambient pressure effects are minor, and it affects the range of burning conditions, but not the overall burning rate. The effect of dropping the atmospheric pressure tends to expand the range of burning to higher burning rates. This is significant, as NASA seeks to provide habitable atmospheres of lower pressure and higher oxygen levels. Such a move will enhance the burning conditions.

The purpose of this burner emulation approach was to exploit an efficient way to study burning in a quiescent microgravity atmosphere. We already knew that materials would burn with a directed oxygen flow, so an examination of quiescent conditions under pure diffusion flame conditions was thought to be essential. While steady burning might be thought as an ideal state, it is the end state for many material fires. The key representative property of the steady state is the heat of gasification. This is exact for vaporizing solids and approximant under real pyrolysis conditions. In any case, the heat of gasification gives an indication of the energy needed to form a fuel gas for burning. In the burning emulation, the mass flux was specified, and the heat of gasification was derived, in the real problem, the heat of gasification is given and the question of burning arises. This question is resolved by use of the empirical flame extinction temperature. Indeed, the flame temperature is independent of the heat of gasification in the solution used herein but depends on the mass flux instead.

The mass flux does depend on L, as well as the flame temperature, surface re-radiation, and external radiant heat fluxes. Hence radiant heat transfer as the flame grows controls burning and

extinction. Therefore, the algorithm should be cast in terms of the ambient conditions, including external radiation, and fuel properties to determine if burning is possible and at what rate. Although It is not straightforward to invert this process, the final results presented herein can be inverted into a flammability map that would give the burning conditions for a given fuel in terms of its

Heat of combustion
Heat of gasification
Burning temperature

and for given ambient oxygen mole fraction and pressure with also consideration of external radiant heat flux. NASA Flammability Test 2, the Cone Calorimeter or equivalent, has the means to classify materials into these properties. This is a pathway for establishing a science-based fire safety evaluation methodology for materials used in spacecraft. A follow up analysis to this paper should investigate these fire conditions and safety implications for space flight materials.

5. Analysis of the steadiness of the flames

The likelihood of steady burning in microgravity is examined with Burning Rate Emulation (BRE) using a gas burner with a flat 25 mm diameter porous surface with two embedded heat flux sensors. The data are greatly expanded from a previous work. The fuel mixture used in this analysis are ethylene and ethylene diluted with nitrogen resulting in a range of heats of combustion from 12 to 47.2 kJ/g. An analytical solution of these flames was utilized to compute their steadiness, temperatures at flame sheet, and sizes. 103 flames were ignited in an ambient with nominal oxygen mole fractions of 0.21, 0.265, 0.34 and 0.40. 49 of those flames burned for the entire duration of the test before the fuel supply was terminated, while the remainder self-extinguished. The flames attained at least 90% of their asymptotic heights for all 49 fuel terminated flames. An estimated critical steady flame temperature ranging from 1100 to 1200 K was observed segregating the sustained and self-extinguished flames. Flame temperatures for the 49 terminated flames were above the critical temperature range indicating sustained steady burning, whereas below they self-extinguished. The measured flame sizes, and radiative loss fractions are reported at the endpoint of the terminated tests. An empirical correlation of the radiative loss fraction with Ω, a dimensionless parameter, was obtained that allows prediction for real fuels at steady burning in microgravity. A flammability diagram, as a plot of the emulated fuel heat of gasification with its burning mass flux, for the range of steady data, is presented comparing how real fuels might burn steadily in normal and microgravity conditions. The results suggest that fuel mass flux burning rates would be about 3 to 4-times higher in 1-g. The heats of gasification and combustion of some real fuels are presented and compared against the burner flames.

The steadiness of the flame heights is examined by utilizing the theoretical solution to these flames [49,51]. A critical flame temperature range of 1100 K to 1200 K was found to distinguish between the extinction and the 49 terminated flames becoming steady where the critical temperature in 1-g is 1600 K [75,85–88,91,91].

5.1 Analysis of the steadiness of the flame heights

The theoretical solution to these flames is based on the classical diffusion flames theory and was used to estimate the steadiness of the flame heights [49,51,52]. The 49 fuel terminated flames reached 0.953 of their asymptotic height before fuel termination with standard deviation of 0.019 [49,51,52]. The theoretical steady flame height is consistent with transient data extrapolated by $1/t \sim 0$. It should be noted that the prediction of flame height does not depend on radiation, but other parameters, such as the flame temperature, does depend on flame radiation [52]. In these calculations a specific heat of 1.23 kJ/kg K was used.

5.2-Dimensional analysis of the Radiative loss fraction based on radiation theory

A dimensional analysis of the radiation data of steady flames led to an empirical correlation flame radiation fraction, X_r with Ω, a dimensionless parameter [52]. Since the flames are blue and sootless, the dimensionless parameter depends on the partial pressures of CO_2 and H_2O for complete combustion, flame size, and oxygen. The correlation is used to reduce the heat of combustion term in the theory to account for the flame radiative heat loss in calculation of the flame temperature (see Eq. (5.3)).

The second term in the Ω formula is the flame emissivity and κ represents the absorption coefficient of radiative gasses in the combustion products. Since the flames are sootless, and as pointed out by de Ris [84], for flames without soot, the absorption coefficient depends on path length, approaching the Planck limit at zero path length [74,83].

RADCAL [58,59], a narrow-band model, was used to estimate emissivity and absorption coefficient for combustion products. It was run for stoichiometric combustion of ethylene, shown by Eq. (5.1), that resulted in partial pressures of water vapor and carbon dioxide calculated by Eq. (5.2). The partial pressures resulted from Eq. (5.2) are responsible for flame radiation and thus, are used as the inputs to RADCAL. The emissivity for ethylene is computed as $1 - e^{-\kappa_f x_f}$ where, $\tilde{\kappa}$ is the normalized absorption coefficient (when obtained κ is divided by the sum of partial pressures of H_2O and CO_2) [52]. It was shown in [23] in detail that for sootless BRE flames $\tilde{\kappa}$ depends only on path length (flame height is taken as the path length for BRE flames) given by $\tilde{\kappa} =$

$7.96e^{-9.85x_f}$ for $x_f < 0.1$m. absorption coefficient, κ , required for obtaining the emissivity for ethylene flames is computed from $\kappa = \left\{ \frac{4}{4+3\left(\frac{1-X_{O2}}{X_{O2}}\right)+\frac{1-X_{C_2H_4}}{X_{C_2H_4}}} \right\} p.\tilde{\kappa}$. Figure 3 shows the radiative loss fraction correlation.

The third dimensionless group of Ω is the normalized flame height squared, $(x_f / R)^2$. The last term of Ω is $\left(T_{f,o}/T_\infty\right)^4$ where $T_{f,o}$ is the flame temperature (T_f) given by Eq. (3) without the radiative heat loss term (1 - X_r). One instead could have used T_f (Eq. (3)) in calculation of Ω which makes the X_r correlation an implicit problem ($X_r = f\ (\Omega(X_r))$, and f is the output of the correlation and found by passing the best fit from the data points.] The radiative heat loss term was removed from Ω to define the X_r an explicit function of Ω (i.e., $X_r = f\ (\Omega)$ with known or calculable parameters.

Quantity X_r derived from remote radiometry [51] and Ω are inputs to Fig. 3 to examine a correlation (the output). The relationship between the variables is based on radiation theory and the correlation shown as a power law fit, obtained empirically by the method of least squares) then supplies a general predictive tool. Substitution of Ω into the correlation ($X_r = 0.49\Omega^{0.12}$) leads to prediction of X_r. Fig. 5.1 shows the radiative loss fraction empirical correlation.

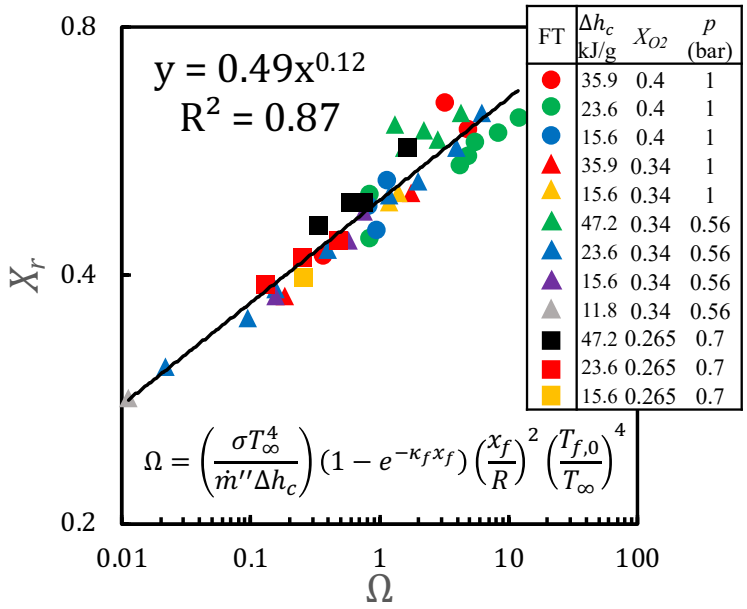

Figure 5.1. Radiative loss fraction empirical correlation resulted from a dimensional analysis of radiometry

$$C_2H_4 + \frac{1 - X_{C_2H_4}}{X_{C_2H_4}} N_2 + 3O_2 + \frac{3 - 3X_{O2}}{X_{O2}} N_2 \rightarrow 2CO_2 + 2H_2O + \frac{3 - 3X_{O2}}{X_{O2}} + \frac{1 - X_{C_2H_4}}{X_{C_2H_4}} N_2 \quad (5.1)$$

$$p_{H_2O} = p_{C_{O_2}} = \frac{2p}{3/X_{O2} + 1/\mathrm{X_{C2H4}}} \quad (5.2)$$

5.3 Calculated temperature at flame sheet

Eq. (5.3) is used to calculate the flame temperature at flame sheet and at steady state. X_r is computed from the correlation of Fig. 5.1, in which Ω is determined using the theoretical steady solution for flame height, the estimated endpoint oxygen concentration, and the prescribed mass flux and heat of combustion [52]. It is observed in Fig. 5.2 that a critical temperature range of 1100 to 1200 K segregates the steady and self-extinguished flames. The extinction data never become steady, as their computed steady state has a temperature below the critical value. The details of each parameter used in Eq. (5.3) is discussed in [49,52].

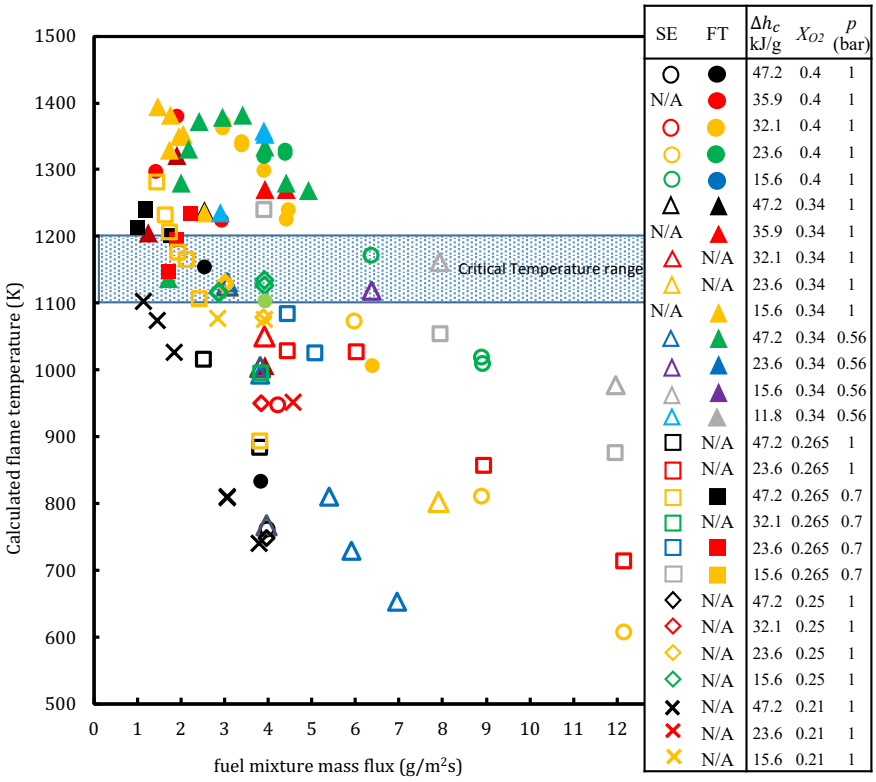

Figure 5.2. Calculated flame temperature at flame sheet, c_p = 1.24 J/g K

$$c_p(T_f - T_\infty) = \frac{1}{\alpha Y_{Fb} + 1\left[c_p(T_s - T_\infty) + Y_{Fb}(1 - X_r)\Delta h_c\right]} \tag{5.3}$$

Fuel mass fraction Y_{Fb} at the burner surface and dimensionless mass flux are found from Eqns. (5.4, 5.5)

$$Y_{Fb} = 1 - e^{-\lambda}(1 + \alpha)/\alpha \tag{5.4}$$

$$\lambda = \frac{\dot{m}''}{4k/(\pi c_p R)} \tag{5.5}$$

Where, $\alpha = S/Y_{O2,\infty}$ and $S = \Delta h_c/\Delta h_{c,O2}$.

5.4 Further analysis of the experimental data

Let us still consider the data set containing the 49 terminated flames as steady and explore the endpoint data. The measured flame height, and aspect ratio (height divided by radius) will be shown and compared to the computed values in the next section and in the end, a flammability diagram (heats of gasification vs. fuel mixture mass flux) is shown that includes micro- and normal gravity data.

5.5 Flame size

The flame heights and radius are measured from the center of the burner to the edge of the flame sheet at the end of each test point. The analytical solution for these flames allowed computation of these dimensions by providing appropriate c_p and k where the properties of nitrogen at 1400 K, that is a representative temperature to these flames, were chosen. Eqns. (5.6, 5.7) were used to

calculate flame height and radius at the endpoints of the tests. The empirical constant c used in Eq.

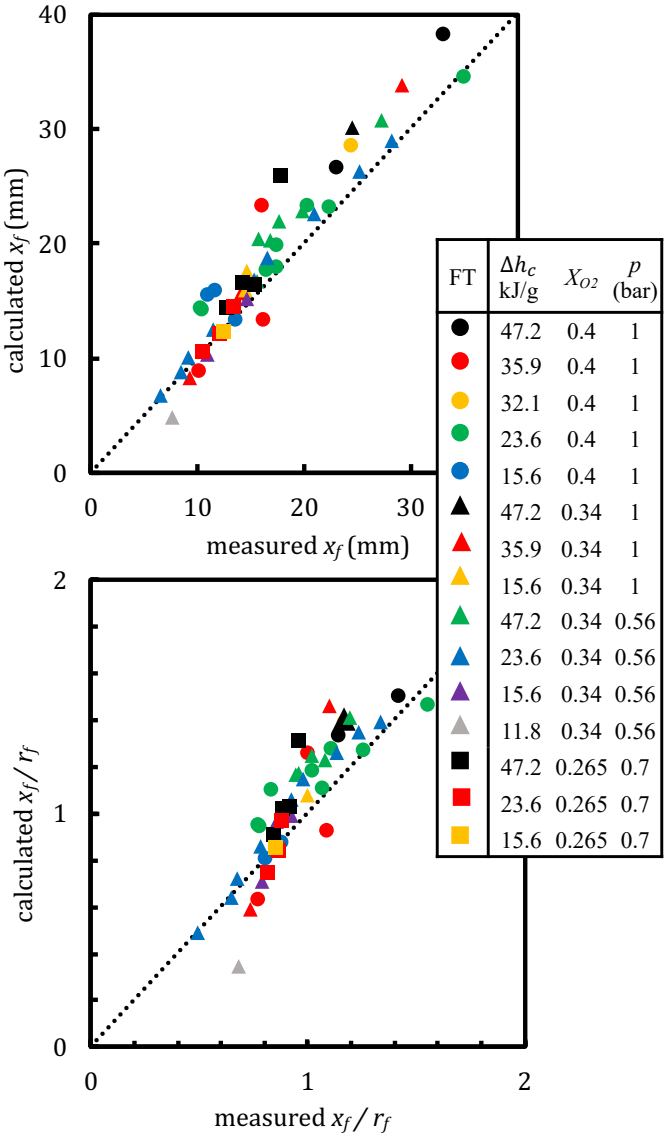

Figure 5.3. Calculated vs. measured, flame heights (top) and flame aspect ratio (bottom)

(5.7) is used to adjust the calculated radius with measured value. The correction is needed because the theoretical model does not allow a flame below the burner surface while in the experiment, the flame could expand on the side of the burner below its surface. Fig. 5.3 show the calculated heights against measured values at the top. The calculated vs. measured aspect ratio, flame heights divided by flame radius, are presented at the bottom of Fig. 5.3. The accuracy of the analytical model

introduced in [49,52] is justified by comparing calculated flame dimensions against those measured in the experiments. The dashed line shown in Fig. 5.3 facilitates this comparison.

$$\frac{x_f}{R} = \tan\left\{\frac{\pi}{2}\left(1 + \frac{\ln(\alpha/(\alpha+1))}{\lambda}\right)\right\} \tag{5.6}$$

$$r_f/R = \sqrt{1 + c\left(x_f/R\right)^2} \tag{5.7}$$

5.6 Surface heat flux

Two heat flux sensors are embedded to the surface of the burner at the center and at an offset location, 9.5 mm from the center. The resulting measured surface heat flux is a summation of convective and radiative heat flux from the flame minus the surface re-radiation (see Eq. (5.10)). Corrections to the sensor measurements were made to account for differences in sensor and burner surface temperatures and have been derived previously and discussed in [10,46–48,55]. The typical transient measured heat fluxes of two tests that led to termination (steady state) and self-extinction are shown and discussed in [51]. The center sensor always measured higher values and the ratio of the center to offset measured values increase with mass flux indicative of radiation dominance over conduction as the flame gets bigger.

5.7 Flammability diagram

An arithmetc average of the measured net heat fluxes at the burner surface, as shown by Eq. (5.8), were used to obtain the heats of gasification.

$$\dot{q}''_{net} = 0.5\ \dot{q}''_{ctr} + 0.5\ \dot{q}''_{r=9.5\ mm} \tag{5.8}$$

In general, Eq. (5.9) is used to calculate heats of gasification

$$\dot{m}'' L = \dot{q}''_{net} \tag{5.9}$$

The heats of gasification reported in Fig. 6 are experimentally obtained by using Eqns. (5.8, 5.9). In general, the net heat flux consists of four terms as shown in Eq.(5.10) and would allow a theoretical [52] derivation of L, not shown in this paper.

$$\dot{q}''_{net} = \dot{q}''_{f,c} + \dot{q}''_{f,r} - \dot{q}''_{rr} + \dot{q}''_{ext,r} \tag{5.10}$$

$\dot{q}''_{f,c}$: Flame convective heat flux

$\dot{q}''_{f,r}$: Flame incident radiative heat flux

$\dot{q}''_{rr}$: Surface radiative loss heat flux

$\dot{q}''_{ext,r}$: Incident external radiative heat flux that is not present in this analysis

The significance of the steady burning data allows for interpreting the heat of gasification corresponding to the steady burning of a real fuel having the associated heats of combustion and gasification. Many real fuels satisfy this theoretical steady burning result, and others approximate it. The flammability diagram shown in ref. [51] is updated with the results obtained in the second round of tests aboard the ISS. The data measured in 1-g and discussed in [55] is added to the plot for comparison between micro- and normal gravity burning. As deducted from Fig. 5.4, the burning rate in normal gravity is about 3 to 4 times higher than microgravity. The figure shows how fuels with a given heat of combustion and gasification would burn for a 25 mm flat disk in an ambient oxygen mole fraction X_{O2} and, pressure, p. The heats of gasification range from fuels associated as liquids (0.5 – 1.5 kJ/g) and solids (greater than 1.5 kJ/g). Liquid fuels burning in microgravity conditions should be absorbed into an inert matrix.

If the small effect of fuel vaporization temperature is neglected, real fuels corresponding to heats of combustion and gasification can be identified among the BRE data of Fig. 5.4. The microgravity steady data are shown on the left of the figure from mass flux of 1 to 6.4 g/m^{2}s and normal gravity trendline is shown on the right of the figure starting from mass flux of 2.1 and up to 30.6 g/m^{2}s. The descending trend of heat of gasification with burner gas flow rate looks similar

for both gravity conditions indicating that increasing mass flow rates results in larger flames where the flame sheet is further from the burner surface and thus, the convective heat flux to the fuel source is decreased which was also discussed in Fig. 9 of [51] (see Eqns. (8) to (10)). It is observed that at a constant heat of gasification (shown by a horizontal line on Fig. 5.4) and heat of

combustion that could represent real material properties, the burning rate in 1-g is approximately 3 to 4 times greater compared to μ-g. The difference is justified by considering the role of gravity in the creation of buoyancy. Buoyancy on the ground causes high radially inward velocities that sweep the flame close to the surface. This causes much higher convective heat fluxes than in the pure conduction of microgravity. In microgravity, natural convection is absent and hot combustion

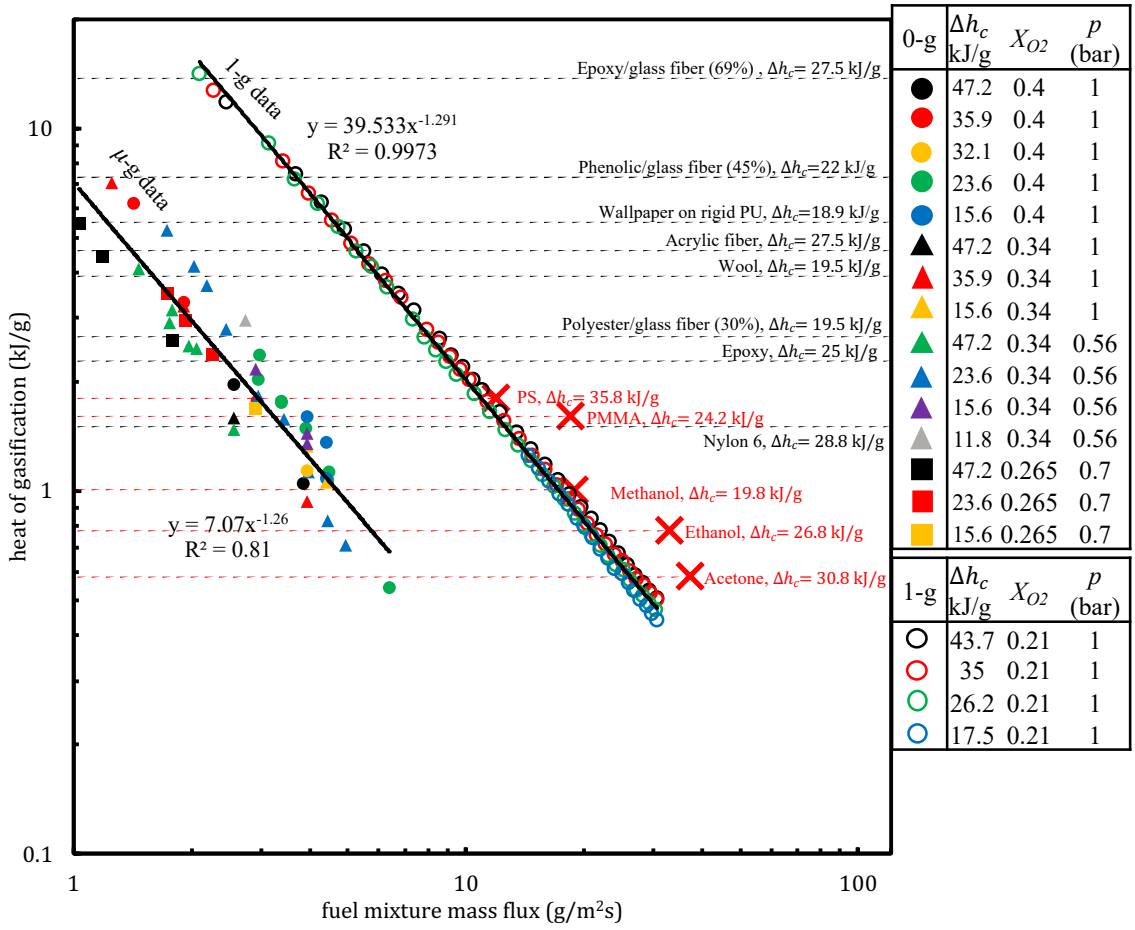

Figure 5.4. Flammability map (heats of gasification vs. fuel mixture mass flux) for micro and normal gravity data for the surface diameter of 25 mm

products move by thermal expansion and diffusion that form hemispherical shaped flames compared to the tall vertical flames in 1-g. Therefore, higher surface heat flux in 1-g, results in higher mass vaporization rate for a given material. The heats of gasification and combustion for some real fuels are taken from [68] and shown as horizontal dashed lines on Fig. 5.4. As the horizontal dashed-lines, indicating real fuel properties, cross the microgravity and 1-g trendlines and if intersecting data point can be found with the same heat of combustion, the two key properties for emulation are matched. Also, shown are some dashed lines ending with red crosses, representing real materials listed in [55,56]. For instance, if one takes the line representing PMMA, the burning rate measured in -1-g is 18.5 g/m^{2}s, the heat of gasification is 1.6 kJ/g and the heat of combustion is 24.2 kJ/g. The green open circle (1-g) and blue triangle (μ-g) are the closest emulated flames to PMMA burning in normal gravity with 21% oxygen and microgravity with 34% oxygen, respectively

It was shown that an increase in the ambient pressure increases the partial pressures of the combustion products and therefore the resulting absorption coefficient, κ, and flame emissivity, ϵ are enhanced. As a result, the radiative heat loss and flame luminosity are increased which causes the flame temperature to decrease. In other words, reduced ambient pressure enhances the fire hazard in microgravity in a quiescent ambient. Quantities D, α, $1/\rho$, ν, and κ are proportional to $1/p$, but ρD is independent of p. In the experimental presentation of this paper, it can be dug out that over 0.56 to 1 atm there appears to be a negligible effect as discussed in [21,23]. For example, in Fig.6 the two points near L=1.6 and $\dot{m}''$= 2.6 correspond to the same conditions but p = 0.56, and 1 atm. In the theoretical analysis [23], little difference was discerned due to the pressure differences, and it was shown that pressure reduction led to expansion of the flammable mass burning rate $\dot{m}''$, i.e., the highest flammable $\dot{m}''$ is increased as p is decreased [23].

An Uncertainty analysis was performed on the microgravity data points of Fig. 6. The sources of uncertainty as given by Eqns. (5.8,5.9) are the measured heat flux and flow rates. The heat flux sensors are manufactured by Medtherm, and the flow meters are made by Teledyne Hastings (model: HFC-302D). The manufacturer's reported uncertainties for the raw measurement

of each instrument were used to obtain the uncertainty of measured heat flux and fuel and nitrogen flow rates. The formulation introduced in [93,94] was utilized to compute the propagation of uncertainties to L and $\dot{m}''$. The normalized uncertainty of the reported heats of gasification ($\delta L/L$) ranged from 4.5% to 17.5% with a mean value of 5.7% and standard deviation of 2.9%. The normalized uncertainty of $\dot{m}''$ ($\delta\dot{m}''/\dot{m}''$) varied from 1.3% to 17% and with a mean value, and standard deviation of 3.1%, and 3.6%, respectively. In short, the representative uncertainty that covers 95% of the errors for all data points would be:

$$\omega\% = \bar{\omega}\% \pm 2\sigma \tag{5.11}$$

Where, ω is the normalized uncertainty of all measurands.

Same approach was performed to obtain uncertainty associated with heats of combustion (varied by changing the fuel-nitrogen mixture dilution) and measured radiative loss fraction X_r. The radiative heat flux was measured by Dexter research 2M wide angle radiometers and the error analysis performed by NASA was used for the uncertainty of the raw radiative heat flux measurements. The resulting uncertainties of X_r, and Δh_c are: $\delta X_r/X_r = 10.11\% \pm 9.6\%$, and $\delta\Delta h_c/\Delta h_c = 3.68\% \pm 6.86\%$

5.8 Chapter Summary

The flammability of 25 mm diameter flat disk-shaped condensed-phase material is examined in microgravity for steady burning. The BRE using a gas fuel supplied burner with two embedded heat flux sensors is an efficient method to study burning in microgravity. The fuel mixture used in this study was ethylene and ethylene diluted with nitrogen to give a range of heats of combustion per unit gram of the fuel mixture of about 12 to 47.2 kJ/g. An analytical solution to these flames was utilized to compute their steadiness, flame temperatures, and heights with good accuracy. 103 flames were successfully ignited in a quiescent ambient with nominal oxygen mole fractions of 0.21, 0.26, 0.34 and 0.40. 49 of those flames burned for the entire duration of the test before the fuel supply was terminated intentionally, while the remainder self-extinguished including all the flames burning in air (i.e., 0.21 nominal oxygen mole fraction). Elevated ambient oxygen concentrations above normal air enhances the flammability of materials while ambient pressure (not discussed here) had a negligible effect [21, 23]. The 49 terminated flames reached 95.3% of

their asymptotic value with a standard deviation of 1.9%. A steady critical flame temperature range of 1100 to 1200 K was observed that segregates the conditions of the steady and self-extinguished flames. Flame temperatures for the 49 terminated flames were above the critical flame temperature range indicating sustained burning. The flame size, and radiative loss fractions are reported at the endpoint of the tests. A dimensional analysis of the radiation data resulted in an empirical correlation of the radiative loss fraction, X_r with, Ω, a radiation dimensionless parameter. Arithmetic average of the two measured surface heat fluxes were used to compute the heats of gasification that resulted in a flammability diagram for microgravity data. The measured heats of gasification in normal gravity were added to the plot. A comparison between flammability of micro- and normal gravity showed that materials burn about 3 to 4 times faster on the ground.

A theoretical methodology used herein could be applied to predict the burning rate of flat surfaces in microgravity. The effect of burning diameter and external radiation can be explored for various real fuels in steady burning under different ambient conditions. We recommend this be done.

6. Flammability Maps for Microgravity Flames on Top of a Flat Disk in a Quiescent Ambient

The current criteria for material selection for use in spacecrafts is based on NASA test 1, an upward flame spread over a real material sample in a controlled environment in 1-g. However, there is no scientific basis to extrapolate the results of this test to microgravity condition. The induced flow because of buoyancy presence in normal gravity flames is in favor of steady flames, a condition that is not applicable to flames in μ-g. The inherent material properties that control flammability should not change with gravity field and this is essential for extrapolation of 1-g test results to μ-g. BRE emulates condensed phase fuels by matching four material properties Δh_c, L, l_s, and T_b. The first two quantities are used for analysis of BRE results in microgravity[50–54,60]. The flames in this study are sootless and laminar smoke point is not applicable to μ-g results. 1-g emulations between the burner and real fuels were very good when matching L, Δh_c, l_s, with T_b not matched [4,10,46,47,55,56]. The T_b is the uncontrolled surface temperature T_s for BRE. Our theory allows for including T_b in predictions [52]. This study provides a flammability map based on Δh_c, and L for each nominal ambient X_{O2}. These properties can be effectively measured by the Cone Calorimeter: NASA Test 2, not currently used to determine flammable hazard in space.

Flammability maps are obtained for each X_{O2} used in this analysis (i.e., 0.4, 0.34, and 0.265). The extinction limits were obtained based on the criteria of setting a critical flame temperature range of 1100 K to 1200 K. The flammable zone will be the area where flames have flame temperatures above this range. Two extinction limits was obtained based on theory [52,60], radiative extinction, and small flame (convective) extinction limit.

6.2 Experimental results

Flame heights and radius, radiative loss fraction correlation and calculated flame temperature for steady flames were reported and discussed in the previous section. Analysis of the measured heat

fluxes by the two-surface embedded heat flux sensors are included in this section. A flammability map (as a plot of Δh_c vs. L) is introduced for each nominal ambient X_{O2}.

6.3 Summary of the endpoint results

The measured values of heat flux, flame height and radius, radiative loss fraction, oscillation onset time for the self-extinguished test points and burn time for all the tests are presented in table 6.1.

Table 6.1. Summary of the endpoint results ordered by X_{O2} for ethylene-nitrogen flames. ordered by X_{O2}, dashes indicate where no radiation data is available, the end conditions are self-Extinguished (SE), Fuel Terminated (FT), and Fuel Terminated with Oscillations (FTO)

test ID	X_{O2} before test	X_{O2} after test	Δh_c kJ/g	p bar	$\dot{m}''$ g/m^2-s	$\dot{q}''_{CTR}$ kW/m^2	$\dot{q}''_{off}$ kW/m^2	y_f mm	r_f mm	X_r before oscillations	Osc. Time s	Ext Time/end time s	end condition
20346L4	0.36	0.3575	16.4	1.055	6.38	4.97	2.45	19.1	16.78	0.539	-	39	SE
20358B1	0.39	0.3771	47.2	1.06	3.99	4.97	2.45	25.56	19.84	-	63.93	113.9	SE
19039A1	0.3972	0.3839	47.2	1.05	3.84	5	3	33	23.3	-	-	123	FT
19039B3	0.3834	0.371	47.2	1.055	2.55	6.52	3.51	22.9	20	-	-	180	FT
20352A8	0.3634	0.3631	35.5	1.06	5.94	4.3	1.5	38.5	28.95	-	40.7	80.13	FTO
20339A0	0.3752	0.3728	35.3	1.055	4.24	8.4	6.47	18.37	16	0.41	13.28	13.51	SE
20352A3	0.381	0.3729	35.7	1.05	2.94	6.68	3.71	15.94	15.91	0.602	-	137.47	FT
20352A5	0.3729	0.3776	36	1.047	1.91	7.93	4.69	16.02	14.75	0.644	-	134.18	FT
20352A6	0.3776	0.3634	36.3	1.04	1.42	10.5	7.04	10	13.02	0.422	-	131.36	FTO
20358B1-1	0.3771	0.3672	32	1.045	3.93	5.8	3.1	24.32	20.8	-	-	135.62	FT
19063C1	0.3618	0.3474	23.6	1.06	12.16	3.17	1.45	80	23.97	-	44.97	147.2	SE
19063B1	0.3786	0.3618	23.6	1.055	8.92	3.73	1.76	62.5	22.25	-	22.4	89	SE
19056A2	0.3881	0.3745	23.6	1.055	6.39	4.54	2.36	34.9	22.5	-	-	180	FT
19063A1	0.3949	0.3739	23.6	1.055	6.00	4.54	2.41	42	21.2	-	106	300	FTO
19056A1	0.398	0.3881	23.6	1.055	4.46	6.27	3.75	22.3	17.7	0.62	-	180	FT
20346A5	0.3809	0.377	23.6	1.05	4.43	6.05	3.43	20.26	18.28	0.595	-	96.53	FT
20358A1	0.3978	0.39	23.7	1.043	3.91	7.24	4.4	17.37	16.97	0.5792	-	132.28	FT
20352A1	0.3943	0.3874	24.7	1.043	3.39	7.52	4.4	16.35	19.71	0.543	-	135.03	FT
20352A2	0.3874	0.381	24.7	1.045	3.39	7.21	4.63	17.37	16.32	0.558	-	133.43	FT
20346A3	0.389	0.3862	23.6	1.045	2.98	8.44	5.65	10.11	13.17	0.501	-	127.8	FT
20346A4	0.3862	0.3809	23.6	1.045	2.95	8.57	3.34	10.32	13.24	0.443	-	64.5	FT
20346L3-1	0.36	0.3575	15.8	1.07	8.94	4	2.3	24.93	18.19	-	47.33	95.23	FTO
20346L3	0.3671	0.36	15.7	1.067	8.91	4.2	2.4	23.81	17.87	-	55.33	95.13	FTO
20346L1	0.377	0.3743	15.8	1.05	4.40	7.22	4.74	10.88	13.48	0.486	-	95.04	FT
20346L2	0.3743	0.3671	15.9	1.05	4.40	6.9	2.61	11.52	13.55	0.453	-	95.21	FT
20358B3	0.3672	0.36193	15.5	1.045	3.92	7.64	4.9	13.42	15.26	0.522	-	157.18	FT
20358B4	0.36193	0.3575	9.3	1.043	3.91	9.5	6.17	8.33	13	0.316	-	122.23	FT

	X_{O2} before test	X_{O2} after test	Δh_c	p	$\dot{m}''$	$\dot{q}''_{CTR}$	$\dot{q}''_{off}$	y_f	r_f	X_r before oscilations	Osc. Time	Ext Time/end time	end condition
20358D2	0.3401	0.3319	47.2	1.05	3.97	4.54	1.58	28.44	22.82	-	41.3	66.5	SE
20352D1	0.3507	0.3404	35.7	1.05	3.94	5.01	2.36	29.15	26.5	-	71.9	121.05	FTO
20352D2	0.3404	0.3346	36	1.04	1.91	7.6	4.68	13.95	15.4	0.503	-	135.33	FT
20352D3	0.3346	0.3307	36.5	1.04	1.25	10.7	6.92	9.21	12.45	0.377	-	120.73	FT
20358D3	0.3319	0.3237	32	1.05	3.93	4.9	2.6	21.77	18.33	-	68.23	132.08	FTO
20358D1	0.3501	0.3401	23.7	1.05	7.92	3.93	2.16	32.58	22.19	-	44.67	76.13	SE
20352F3	0.3306	0.3249	15.4	1.045	4.41	5.86	3.48	14.54	14.57	0.503	-	138.34	FT
20358D5	0.3208	0.3164	15.7	1.045	3.95	6.42	4.04	14.47	15.92	0.4897	-	131.32	FT
21020A1	0.3499	0.3404	15.6	0.595	3.92	6.75	4.5	13.17	15.36	0.44	-	133.64	FT
20358D4	0.3237	0.3208	9.4	1.04	3.91	8.12	4.74	7.44	11.03	0.3278	98.33	111.21	FTO
19094K1	0.3511	0.3495	47.2	0.57	6.96	2.92	1.67	74	34.64	-	20.72	36	SE
19094J1	0.3525	0.3511	47.2	0.57	5.93	2.96	1.62	58.2	35.42	-	29.5	37	SE
19094H1	0.3541	0.3525	47.2	0.57	5.41	3.15	1.66	59.1	34.57	-	37.7	47	SE
19051C3	0.3152	0.3066	47.2	0.57	3.84	4	2.27	41.8	25.71	-	48.5	66	SE
19051G1	0.2979	0.2831	47.2	0.57	3.84	3.64	2.09	42.9	26.6	-	43.8	67	SE
19051B1	0.3262	0.3163	47.2	0.57	3.07	4.79	1.46	28.8	23.42	-	63.5	99	SE
19051F1	0.3178	0.2979	47.2	0.57	3.07	4.08	2.15	37.6	27.95	-	94.8	131	SE
19051A1	0.3391	0.3262	47.2	0.565	2.55	5.18	2.9	24.5	20.9	-	-	180	FT
19051D1	0.3394	0.3178	47.2	0.565	2.55	4.92	2.57	27.2	22.8	-	-	180	FT
20261F2	0.3187	0.3925	47.2	0.604	2.45	4.9	7.6	9.3	11.86	-	-	130.2	FT
19087A1	0.3604	0.3428	47.2	0.604	2.06	6.6	3.58	19.8	19.4	0.63	-	180	FT
20261B1	0.3488	0.3362	47.2	0.604	1.96	6.3	3.5	17.55	16.26	0.584	-	131.03	FT
19087B1	0.3428	0.3276	47.2	0.604	1.78	7.05	4.09	16.8	17.8	0.6	-	180	FT
19087D1	0.315	0.3049	47.2	0.604	1.78	9.27	5.7	10.7	14.5	0.48	-	180	FT
20261D2	0.331	0.3196	47.2	0.606	1.75	6.4	3.75	15.63	16.29	0.571	-	130.37	FT
19087C1	0.3276	0.315	47.2	0.606	1.47	7.51	4.46	15.5	17.3	0.608	-	180	FT
19056D3	0.3282	0.3098	23.6	0.565	6.39	3.32	1.66	42.6	38.6	-	58.5	137	SE
19070D1	0.3598	0.3419	23.6	0.565	4.94	4.48	2.5	28.1	21	-	-	180	FT
19070C1	0.342	0.331	23.6	0.605	4.43	4.61	2.7	25.6	20.4	0.63	-	120	FT
19070B1	0.3524	0.342	23.6	0.605	3.95	5.52	3.35	20.9	18.4	0.57	-	120	FT
19070A1	0.361	0.3524	23.6	0.605	3.43	6.5	4.32	16.5	16.8	0.52	-	114	FT
19066J1	0.3429	0.3324	23.6	0.605	2.95	6.61	4.11	15.2	16.4	0.5	-	180	FT
19066G1	0.3519	0.3429	23.6	0.605	2.44	8.2	5.37	11.4	14.5	0.43	-	180	FT
19066F1	0.3599	0.3519	23.6	0.605	2.18	9.64	6.39	9.1	13.4	0.385	-	180	FT
19066D3	0.3586	0.3503	23.6	0.605	2.02	10.1	6.72	8.4	12.9	0.355	-	180	FT
19066D4	0.3503	0.3436	23.6	0.605	1.80	8.21	5.39	9	14.1	0.6	-	180	FT
19066D5	0.3436	0.3367	23.6	0.605	1.73	11.2	6.81	6.3	13	0.31	-	180	FT
19056D2	0.3448	0.3282	23.6	0.6	4.49	4.54	2.5	41.8	20.19	0.595	-	180	FT
21020B2	0.3316	0.3184	15.7	0.61	11.97	2.75	1.4	40.75	22.1	-	25.83	61.1	
21020C1	0.3118	0.2951	15.6	0.615	7.93	3.3	1.8	32.29	20.77	-	48.9	128.43	
21020B1	0.3404	0.3316	15.7	0.6	3.95	6.4	4.2	14.5	15.67	0.478	-	130.8	FT
21020B3	0.3184	0.3118	15.6	0.6	2.91	7.8	4.8	10.82	13.71	0.377	-	132.7	FT
20261G1	0.3925	0.2978	12.5	0.613	6.63	4.2	2.22			-	118.3	129.9	
20261C1	0.3362	0.331	12.2	0.6	2.73	10.4	5.73	7.5	11	0.284	-	130.7	FT
20261G2	0.2978	0.2917	11.9	0.611	2.66	3.8	2.8	19.77	16.48	0.5417	65.23	65.23	FT
19039C1	0.2607	0.2534	47.2	0.707	3.84	3.2	2.33	38.1	28.46	-	18.4	26	SE
19051K1	0.251	0.244	47.2	0.707	3.84	3.17	2.11	44.6	27.17	-	18.8	25	SE
19039D1	0.2534	0.2488	47.2	1.055	2.55	3.8	2.75	43.5	28.15	0.56	32.2	40.7	SE
20261J1	0.2861	0.2753	47.2	0.741	2.45	4	1.6	23.92	17.98	-	52.7	88.37	SE
19094D1	0.2785	0.2705	47.2	0.74	2.14	4.66	2.62	30.4	23.52	0.59	67.9	78.7	SE
20261J2	0.2686	0.262	47.2	0.741	1.96	4.5	1.5	20.08	19.14	-	74.5	76.53	SE
19087H1	0.2708	0.2605	47.2	0.74	1.78	5.95	3.27	17.7	18.4	0.57	-	180	FT
20261J3	0.262	0.2554	47.2	0.742	1.75	4.68	2.7	23.06	21.82	-	81.4	86	SE

	X_{O2} before test	X_{O2} after test	Δh_c	p	$\dot{m}''$	$\dot{q}''_{CTR}$	$\dot{q}''_{off}$	y_f	r_f	X_r before oscilations	Osc. Time	Ext Time/end time	end condition
19094F1	0.2705	0.2614	47.2	0.707	1.67	5.33	2.95	25.5	20.41	0.56	117.85	133	SE
19087G1	0.2825	0.2708	47.2	0.707	1.47	5.05	2.93	29.9	22.42	0.6	141.63	160	SE
19094G1	0.2614	0.2524	47.2	0.74	1.19	6.7	3.8	15.25	16.6	0.49	-	180	FT
19087J2	0.2602	0.2513	47.2	0.74	1.19	6.63	3.85	14.2	16	0.49	-	180	FT
19087K1	0.2513	0.2433	47.2	0.74	1.03	7.13	4.1	12.6	14.9	0.46	-	180	FT
21020D3	0.2581	0.2542	32	0.74	3.86	3.4	1.8			-	27	31.7	SE
19063G1	0.2585	0.2535	23.6	0.71	12.16	2.92	1.57	72.7	23.4	-	11.8	28	SE
19063F1	0.2628	0.2585	23.6	0.71	8.95	2.88	1.7	59.5	22.76	-	18.4	32	SE
19063D1	0.2662	0.2628	23.6	0.71	6.03	3.41	2.3	44.1	22.03	-	18.7	33	SE
19056G1	0.2431	0.2392	23.6	0.74	5.10	3.11	1.66	28	24.48	0.52	23.45	35	SE
19056B1	0.254	0.2511	23.6	1.055	4.46	3.71	2.58	27.3	21.06	0.5	23.1	38	SE
19056F1	0.2471	0.2431	23.6	0.74	4.46	3.48	1.88	28.9	23.44	0.53	31.85	42	SE
19070K1	0.2782	0.2735	23.6	0.74	2.25	6.52	4.06	13.3	15.1	0.44	-	120	FT
19070H1	0.2735	0.2672	23.6	0.74	1.93	7.22	4.16	11.9	13.8	0.42	-	180	FT
19070L1	0.2672	0.2619	23.6	0.74	1.73	7.5	4.6	10.4	12.7	0.39	-	180	FT
21020F2	0.2648	0.2581	15.7	0.748	11.97	2.4	1.4	42.95	20.42	-	36.57	37.27	SE
21020F1	0.2716	0.2648	15.7	0.743	7.96	2.77	1.73	32.76	20.53	0.544	20.3	57.76	SE
21020D1	0.2796	0.2758	15.5	0.734	3.92	3.8	2.26	24.61	21.36	0.765	62.5	74.34	SE
21020D2	0.2758	0.2716	15.6	0.732	2.91	6	3.76	12.38	14.5	0.397	-	102.7	FT
20261H2	0.2753	0.2686	12.5	0.743	6.63	3.04	1.86	25.5	21.8	0.536	53.4	73.63	SE
20261H1	0.2917	0.2831	11.9	0.73	2.66	8.4	2.6	9.51	12.63	0.221	20.6	83.8	SE
20279J3	0.2467	0.2454		1.033		6.9	4.7	15.73	17.5	0.338	5.77	5.77	SE
20279J4	0.2454	0.2442		1.032		7.8	5	11.79	14.16	0.283	5.57	6.37	SE
20279J5	0.2442	0.2406		1.033		8.2	5.1	12.2	14.29	0.28	5.67	5.83	SE
20358G6	0.2448	0.2416	47.2	1.045	3.97	3.04	2.26	34.27	25.04	-	12.83	17.83	SE
20358G7	0.2416	0.2394	32	1.045	3.86	3.6	2.6	28.44	22.54	-	14.37	18.07	SE
20358G1	0.2508	0.2495	23.7	1.045	3.91	3.25	1.78	32.79	22.3	-	13.9	32.03	SE
20346H1	0.2536	0.2487	23.6	1.04	3.03	3.95	2.44	16.15	17.06	0.483	45.64	55.17	SE
20346H2	0.2487	0.2473	23.6	1.04	3.03	4	2.7	16.01	16.99	0.478	42.67	55.64	SE
20358G4	0.247	0.2455	15.5	1.04	3.92	4.07	3.38	13.13	13.55	0.33	11.1	28.87	SE
20358G2	0.2495	0.2478	15.5	1.04	3.92	4.05	2.93	16.64	17.38	0.476	27.94	32.67	SE
20346H4	0.2458	0.2457	15.5	1.035	2.89	5.3	4.3	10.25	13.24	0.36	29.13	47	SE
20346H3	0.2473	0.2458	15.5	1.035	2.89	5.5	3.9	11.17	14.19	0.368	33.8	49.37	SE
20346H5	0.2457	0.3874	13.2		2.23					not useful			
20358G5	0.2455	0.2448	4.6	1.04	7.95	3.45	2.8	12.71	12.89	0.374	7.8	9.53	
20358G3	0.2478	0.247	9.4	1.04	3.91	4.06	3.16	16.22	16.68	0.675	23.8	40.73	
19039G1	0.1967	0.1904	47.2	1.01	5.13	2.31	1.42	60	27.96	-	-	13	SE
19039F1	0.2009	0.1967	47.2	1.05	3.81	3.07	2.38	33	24.84	-	8.94	16	SE
19039H1	0.1867	0.184	47.2	1.05	3.07	3.9	2.67	25	23.87	0.38	13.21	17	SE
19039H2	0.184	0.1815	47.2	1.05	3.07	4.06	2.7	25.5	24.73	0.38	14.31	17	SE
19094A1	0.2209	0.2179	47.2	1.05	1.86	5.3	3.58	21.6	21.05	0.5	17.1	21	SE
19094A2	0.2179	0.2152	47.2	1.05	1.47	6.33	4.17	16	18.03	0.42	27.3	30	SE
19094A4	0.215	0.2124	47.2	1.05	1.16	6.8	4.58	18.7	15.76	0.37	31.33	37	SE
19056C1	0.2152	0.2133	23.6	1.05	4.58	3.05	2.45	28.1	21.94	0.42	13.42	19	SE
21020G4	0.2195	0.2186	15.6	1.037	3.92	3.85	2.85	20.22	19.12	0.505	13.8	14.84	SE
21020G3	0.2203	0.2195	15.6	1.039	2.86	4.8	3.35	19.04	18.3	0.625	14.94	16.44	SE

6.4 An analysis of the steadiness of flames

The main objective of this analysis is to get a flammability map based on material properties, L and Δh_c. For the problem of burner with constant mass flux, the heat of gasification can only be obtained from steady flames. Therefore, the analytical solution to these flames that is based on classical diffusion flames theory, is used to estimate the steadiness of these flames. Obviously, those flames can only be found from the set of fuel terminated tests. It is shown that the 49 fuel terminated flames reached 0.953 of their asymptotic height before fuel termination with standard deviation of 0.019 and the results are shown in Fig. 6.1. The state of the self-extinguished flames showed that they ranged from about 0.5 to 0.9 of their computed steady value, indicating they were relatively far from being steady at extinguishment.

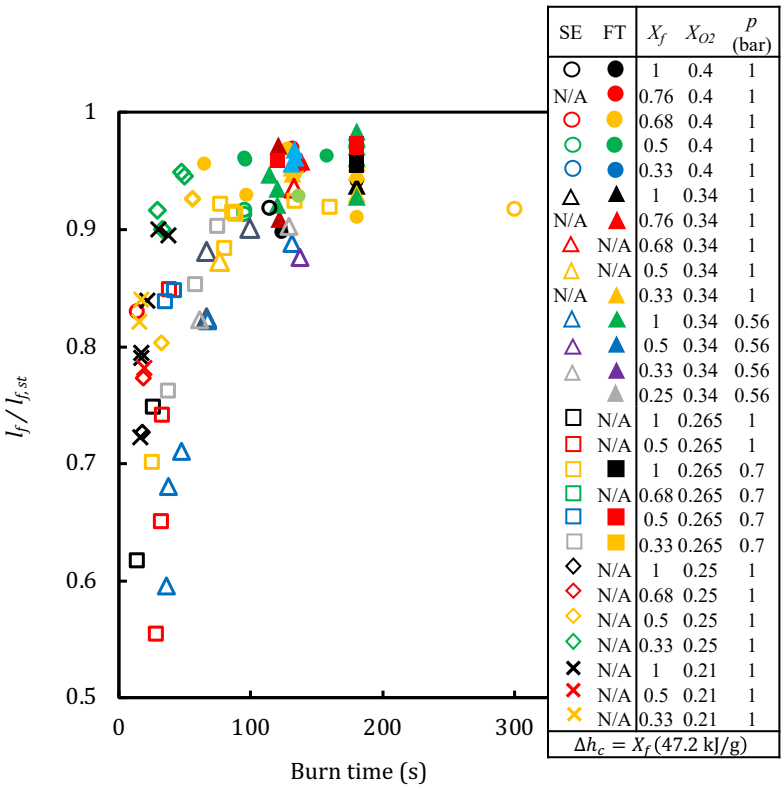

Figure 6.1. Steadiness of flames estimated by the analytical solution to BRE flames generated by the 25 mm BRE burner and ethylene-diluent mixture

6.5 Measured surface heat flux at the r = 0, and 9.5 mm

The heat fluxes at the center and offset location on the burner surface are measured at the end point of steady flames and reported against burner mass flux. The measured heat fluxes are corrected to account for the difference between the sensor and burner surface temperature . It is shown that as the mass flux is increased the flame grows and gets further from the surface and thus the surface heat flux is decreased. The center to offset heat flux ratio is increased as mass flux is increased. It suggests the dominance of surface radiative heat flux as the flames grow. Fig. 6.2 shows the two local net heat flux measurements for all 49 steady flames; this is a complement to the same figure shown in [4,10,30,81,82].

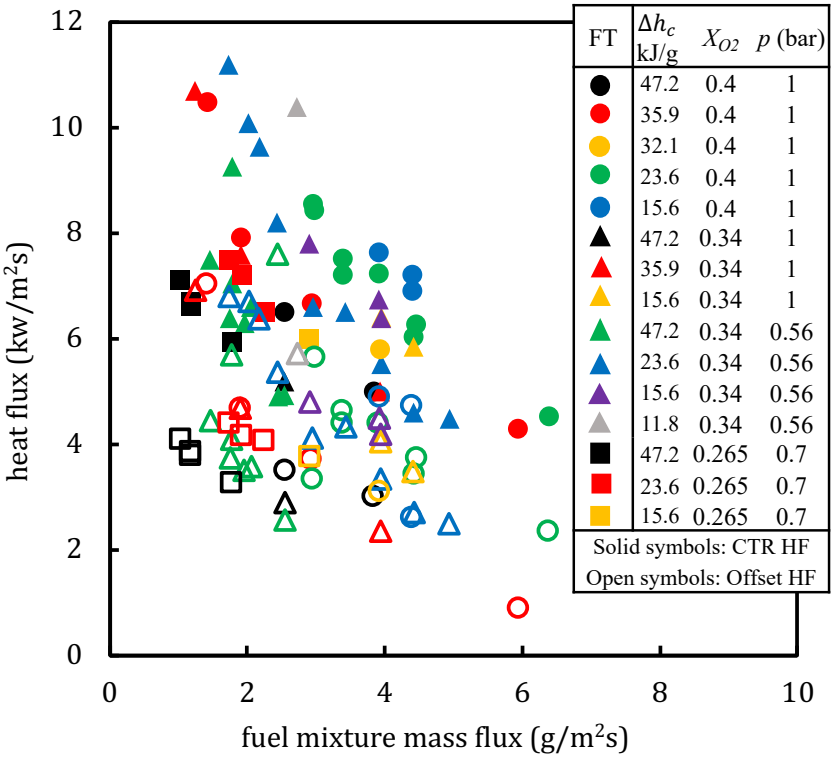

Figure 6.2. Measured heat flux at the center and the offset location on the surface at the endpoints of steady flames generated by the 25 mm BRE burner and ethylene-diluent mixture

6.6 Heats of gasification

The heat of gasification, L, is obtained by dividing the arithmetic average of the two measured net heat flux at the surface (Fig. 6.2) by fuel mixture mass flux (See Eqn. (6.1)) Eqn. (6.2) elaborates the surface net heat flux, $\dot{q}''_{net}$, components that can be calculated. The computation algorithm first introduced in [52] allows computation of heat of gasification by calculating the heat flux components shown by Eqns. (6.2 to 6.5).

$$L = \frac{\dot{q}''_{net}}{\dot{m}''} \tag{6.1}$$

where the RHS consists of four terms (see Eq. (6.2))

$$\dot{q}''_{net} = \dot{q}''_{f,c} + \dot{q}''_{f,r} - \dot{q}''_{rr} + \dot{q}''_{ext,r} \tag{6.2}$$

$\dot{q}''_{f,c}$: Flame convective heat flux

$\dot{q}''_{f,r}$: Flame incident radiative heat flux

$\dot{q}''_{rr}$: Surface radiative loss heat flux

$\dot{q}''_{ext,r}$: Incident external radiative heat flux that is not present in this analysis

The average of each component can be calculated by Eqns. (6.3 to 6.5)

$$\overline{\dot{q}_c''} = \left(\frac{4k}{\pi R c_p}\right)\left\{\frac{\lambda}{e^{\lambda}-1}\right\}\left[\frac{\Delta h_c(1-X_r)Y_{O,\infty}}{S} - c_p(T_s - T_\infty)\right] \tag{6.3}$$

$$\overline{\dot{q}_{f,r}''} = \frac{F_{f\to s}\dot{Q}_r/2}{\pi R^2} = \frac{F_{f\to s}X_r\dot{m}''\Delta h_c}{2} \tag{6.4}$$

$$\dot{q}_{rr}'' = \varepsilon_s\sigma(T_s^4 - T_\infty^4) \tag{6.5}$$

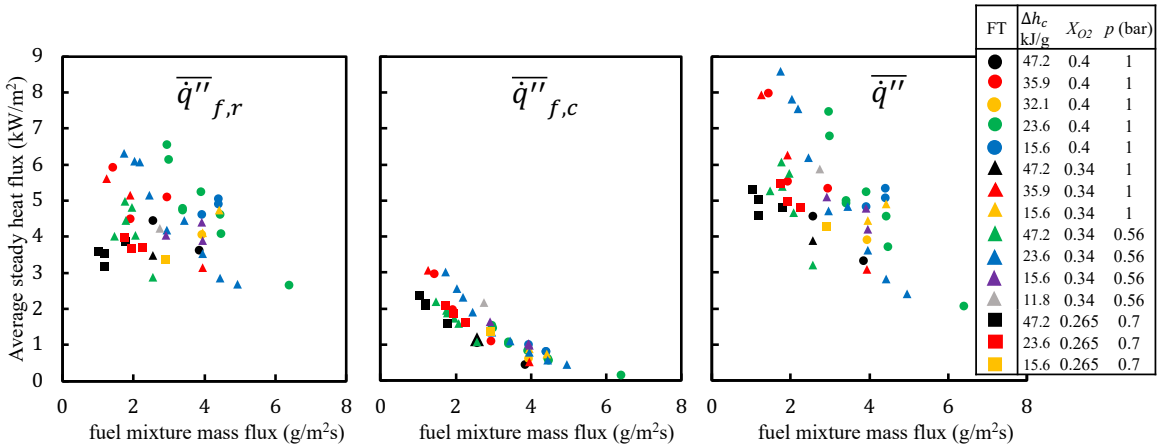

Figure 6.3. Calculated radiative and convective heat flux for steady flames generated by the 25 mm BRE burner and ethylene-diluent mixture

where $S = \frac{\Delta h_c}{\Delta h_{O2}}$, and $F_{f\to s}$ is the geometrical view factor of the burner surface (subscript *s*) with respect to the flame sheet (subscript *f*).

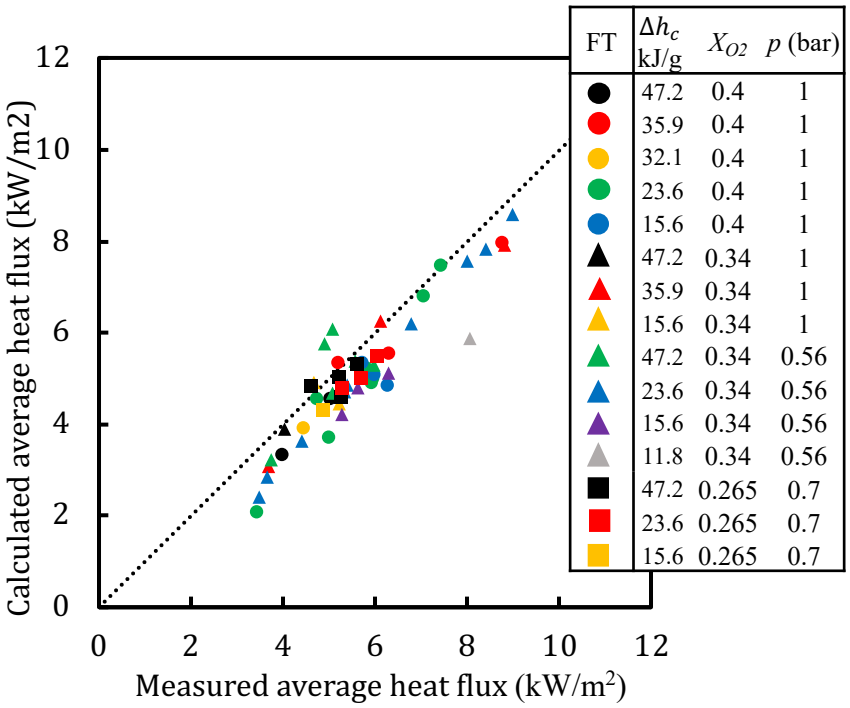

Figure 6.4. Calculated vs. measured average heat flux for steady flames generated by the 25 mm BRE burner and ethylene-diluent mixture

The average flame convective heat flux is calculated by using the analytical solution introduced in [10,46–48,55]. Total radiative heat loss is measured by remote radiometers and the radiative loss fraction is correlated with a dimensionless parameter, Ω, and it is used to estimate the average radiative heat flux to the surface [52]. The average radiative heat flux is estimated by using the geometrical view factor of the fuel source with respect to the flame sheet, a quantity that determines the ratio of the total flame radiation impinging the surface. The re-radiation from the surface is calculated by using Eq. (6.5) with surface emissivity of unity. The trends of calculated average radiative, and convective heat flux against mass flux are presented and compared with the trend of average heat flux vs. mass flux in Fig. (6.3). It is shown that as mass flux is increased, the flame size gets larger and in general, the portion of total radiative heat that impinges the surface is increased. It explains the reason for the radiative heat flux becoming dominant over the surface as mass flux is increased. Accuracy of computation algorithm is supported by comparing the calculated, and measured heats of gasification, shown in Fig. (6.4).

Now, the heat flux components presented in Fig. (6.3) are divided by mass flux to present their contribution to the L. The results are shown in Fig. (6.5) and the computed heats of gasification are compared with measured counterparts in Fig. (6.6) to show the accuracy of the computation algorithm [52]. The scatter of radiative heat flux against mass flux is reduced significantly because of dividing by mass flux. Variations in Δh_c among the steady data causes the scatter of radiative heat flux when shown just against mass flux (Fig. (6.3)). There is a descending trendline for each Δh_c when surface heat flux is analyzed. As heat flux is divided by fuel mixture mass flux (as shown

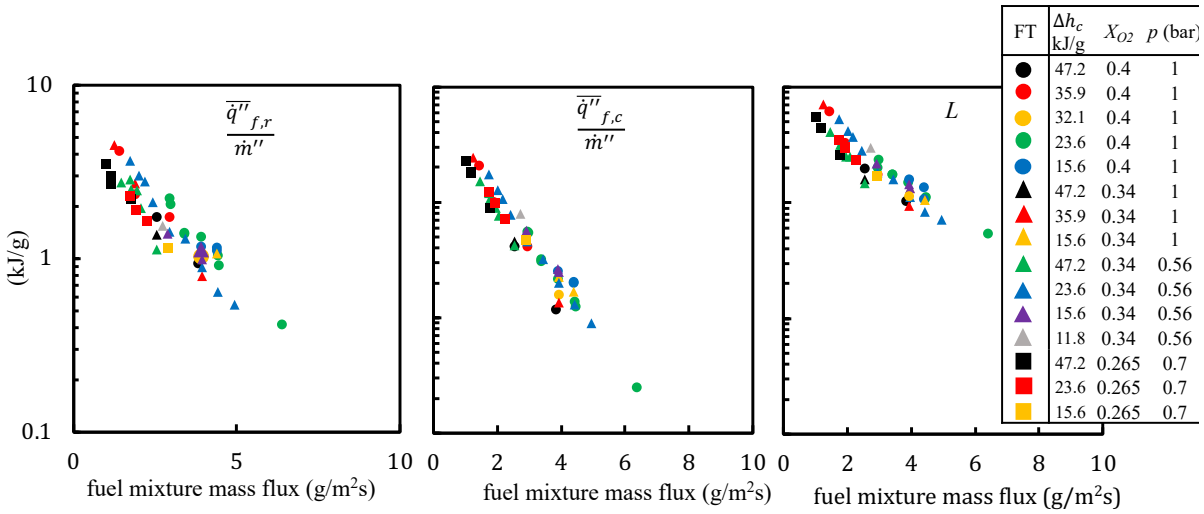

Figure 6.5. Contribution of heat flux components to calculated heat of gasification for steady flames generated by the 25 mm BRE burner and ethylene-diluent mixture

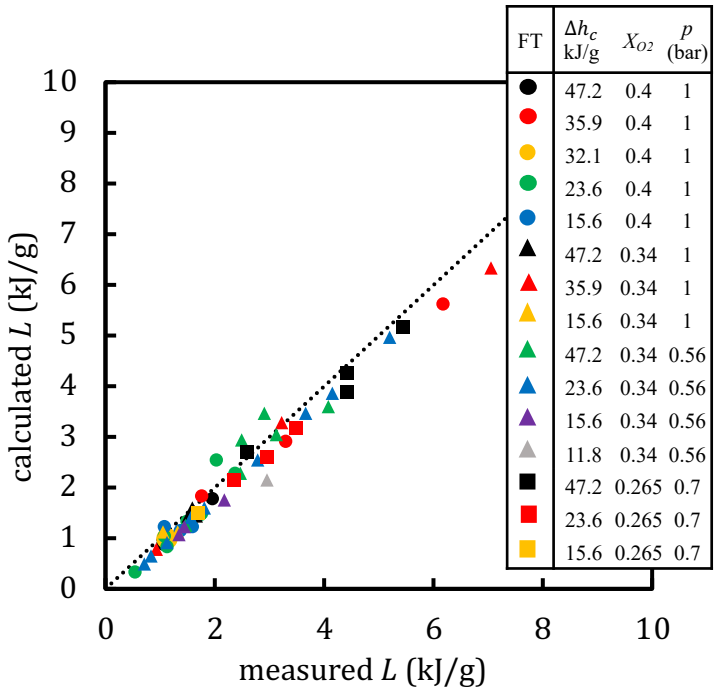

Figure 6.6. Calculated vs. measured heats of gasification for steady flames generated by the 25 mm BRE burner and ethylene-diluent mixture

in Fig. 6.5), the effect of Δh_c is removed and the data collapse into a finer region. However, in addition to Δh_c, X_{O2}, and X_r (and slightly p) are still affecting the trends shown in Fig. (6.5)

6.7 The flammability maps

Two of the key material properties that are used to emulate condensed phase burning are heat of combustion and heat of gasification. In diagrams that were shown in previous chapters [51], the heat of gasification was plotted against fuel mixture mass flux. The heat of combustion was found from the legend of the plot and emulation was performed by drawing horizontal lines (to match the heat of gasification) through the diagram and matching the real fuel properties with a data point with similar heat of combustion at the crossing location. This was shown and explained in the previous chapter. In this chapter, both material properties are presented as the axis of the plot enabling one to place real material properties as "points" on the plot and emulation is performed

when a burner generated flame data point and the real material data point fall reasonably close to each other on the plot.

Before addition of real material properties to the flammability maps, the trends observed in the plots are discussed (See Fig. 6.7 to 6.9). The flammability map is obtained for each ambient nominal X_{O2}. The data points fall in between two extinction limits:

1. Radiative extinction limit: It is observed for large flames where the mass flux is increased and radiative heat loss increases [51], or the radiative fraction increases with mass flux, the flame grows until the chemical reaction stops (see Figs. 6.9 to 6.11, middle plot, where moving to the left of the plots is equivalent to increase in mass flux). The red curves shown on each flammability map indicate the radiative extinction limit and shown as a range that correspond to critical temperature range of 1100 to 1200 K [60]. The curves have a theoretical basis that is discussed in [52] and briefly explained herein:

The Δh_c, and Y_{O2} are given and varied through the range corresponding to the experiments. The Flame height and radius are computed by using Eqns. (6.6, 6.7). Parameter "c" in Eq. (6.7) is used to correct the computed flame radius to match the measurement [34].

$$\frac{x_f}{R} = \tan\left\{\frac{\pi}{2}\left(1 + \frac{\ln\left(\frac{\alpha}{\alpha+1}\right)}{\lambda}\right)\right\} \tag{6.6}$$

$$\frac{r_f}{R} = \sqrt{1 + c\left(\frac{x_f}{R}\right)^2} \tag{6.7}$$

Where $\lambda = \dot{m}''/4k/(\pi c_p \text{ R})$, and $\alpha = \Delta h_c/\Delta h_{c,O2} Y_{O,\infty}$. Radiative loss fraction, X_r, was obtained based on the steady data points at their end points. The steady data was correlated with a dimensionless parameter, shown by Eq. (6.8), which is based on radiation theory. A power function fit was passed through the data points when X_r was plotted against Ω based on the method of least squares. κ_f is found from [52], flame height are computed from Eq. (6.6), and (6.7), and $T_{f,o}$ is the

calculated flame temperature assuming no radiative heat loss and is given by: $c_p\left(T_{f,o} - T_\infty\right) = 1/1 + aY_{Fb}\left[c_p(T_s - T_\infty) - Y_{Fb}\Delta h_c\right]$.

$$\Omega = (\sigma T_\infty^4/\dot{m}''\Delta h_c)(1 - e^{-\kappa_f x_f})\left(x_f/R\right)^2\left(T_{f,o}/T_\infty\right)^4 \tag{6.8}$$

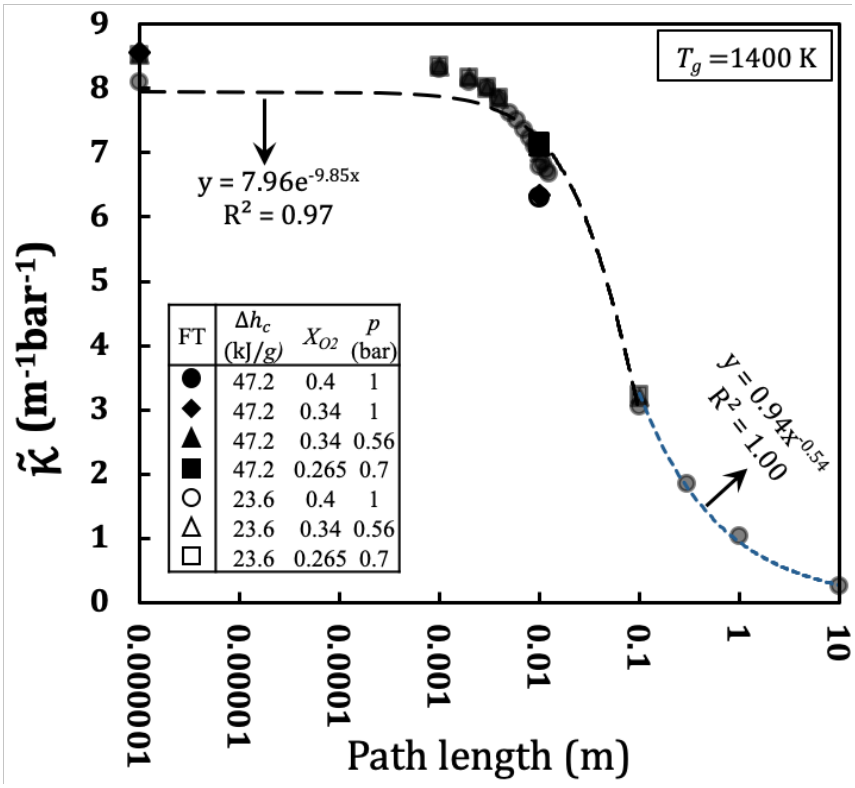

Figure 6.7. Absorption coefficients normalized by partial pressures of combustion products of ethylene

From Figure 6.7 one can find the absorption coefficient, and then the emissivity term in Ω. It should be pointed out that the path length shown on the absicissa, is flame height. It varies for the BRE data from about 5 to 50 mm, indicating a modified absorption coefficient of about 7.5 to 4.5 (m-bar)$^{-1}$, respectively. This corresponds to emissivity in the range of 0.01 to 0.1.

The absorption coefficient can be computed from the fitted Eqns. (6.9 and 6.10). where the Eq. (6.10) includes the sum of partial pressures of water vapor and carbon dioxide, $p_{H_2O} = p_{C_{O_2}} = \left\{ {2}\Big/{2 + 2 + 3\left(1 - X_{O_2}/X_{O_2}\right) + 1 - X_{C_2H_4}/X_{C_2H_4}} \right\} p.$

$$\begin{cases} \tilde{\kappa}(\mathrm{m^{-1}bar^{-1}}) = 7.96e^{-9.85x_f}\ for\ x_f \le 0.1\ \mathrm{m} \\ \tilde{\kappa}(\mathrm{m^{-1}bar^{-1}}) = 0.94x_f^{-0.54}\ for\ x_f > 0.1\ \mathrm{m} \end{cases} \tag{6.9}$$

$$\kappa(m^{-1}) = \left\{ \frac{4}{2 + 2 + 3\left(\frac{1 - X_O}{X_O}\right) + \frac{1 - X_{C_2H_4}}{X_{C_2H_4}}} \right\} p(bar).\tilde{\kappa}(m^{-1}bar^{-1}) \tag{6.10}$$

And Radiative loss fraction is found from Fig. 6.8, and Eq. (6.11)

$$X_r = 0.49\Omega^{0.12} \tag{6.11}$$

Now one can compute the components of surface heat flux, the quantities required for computation of *L*. The heat flux components were initially introduced in Eqns. (6.2-6.5) but are presented here for convenience in following the concept. The net heat flux contains four components where external radiation is not present in these experiments (See Eq. (6.12)).

$$\dot{q}''_{net} = \dot{q}''_{f,c} + \dot{q}''_{f,r} - \dot{q}''_{rr} + \dot{q}''_{ext,r} \tag{6.12}$$

The average convective heat flux is computed by using the analytical solution to these flames [49,52] shown by Eq. (6.13).

$$\overline{\dot{q}''_c} = \left(\frac{4k}{\pi R c_p}\right)\left\{\frac{\lambda}{e^{\lambda} - 1}\right\}\left[\frac{\Delta h_c(1 - X_r)Y_{O,\infty}}{S} - c_p(T_s - T_\infty)\right] \tag{6.13}$$

Where heat conductivity, k, and specific heat, c_p, are those of Nitrogen at 1400 K. Average radiative heat flux is computed using a geometrical model based on radiation view factor of the burner surface with respect to the flame sheet, $F_{f\to s}$ (See Eq. (6.15)), that leads to calculation of the portion of total radiative heat loss that impinges the surface, which is given by Eq. (6.14)

$$\overline{\dot{q}''_{f,r}} = \frac{F_{f\to s}\dot{Q}_r/2}{\pi R^2} = \frac{F_{f\to s}X_r\dot{m}''\Delta h_c}{2} \tag{6.14}$$

Where

$$F_{f\to s} = \frac{F_{s\to f}\,A_s}{A_f} \tag{6.15}$$

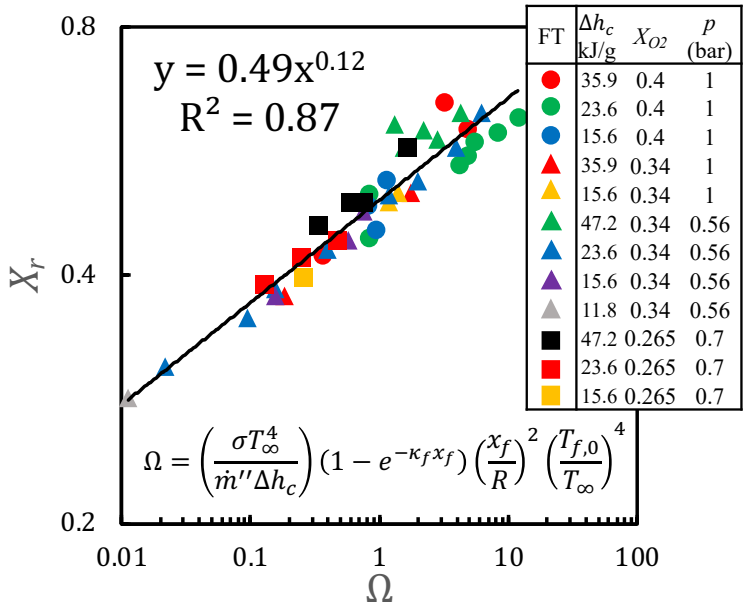

Figure 6.8. Radiative loss fraction empirical correlation resulted from a dimensional analysis of radiometry

The $F_{s\to f} = 1$, and the flame sheet surface area, A_f, is estimated by assuming a half ellipsoid shape for the flame and that area is calculated by Eq. (6.16).

$$A_f = \left(\frac{2\pi\left(r_f^{3.2} + 2\left(r_f x_f\right)^{1.6}\right)}{3}\right)^{\frac{1}{1.6}} \tag{6.16}$$

The re-radiative heat flux is calculated from Eq. (6.17), where surface emissivity is unity, and surface temperature is assumed to be 353.15 K, a representative surface temperature.

$$\dot{q}''_{rr} = \varepsilon_s \sigma (T_s^4 - T_\infty^4) \tag{6.17}$$

Where $a = \Delta h_c / \Delta h_{c,o} Y_{o,\infty}$, and c is a correction factor that makes the predicted flame radius equal to measured counterparts and is found to be 0.35. Now we apply the extinction criteria to the steady flame temperature formula (Eq. (6.18)). The T_f is set to the critical value of 1100, or 1200 K, and one solves for the corresponding L and Δh_c, for a given Y_{O2}. But Eqns. (6.6 to 6.18) are a set of implicit equations that should be solved numerically and by substituting values. The steady mass flux, $\dot{m}''$at the extinction point defined by a critical flame temperature of 1100 or 1200 K. The equations are solved numerically to obtain the radiative extinction limit. The procedure starts by setting Y_{O2}, substituting a range of Δh_c (0 to 47.2 kJ/g), and finding the mass flux that leads to $T_f = T_{cr}$ = 1100, or 1200 K.

In order to find the mass flux, the Microsoft Excel built-in optimizer toolkit, *solver* is utilized to minimize the resulting T_f difference with the critical temperature (i.e., minimizing $\left(T_f - T_{cr}\right)^2$).

$$c_p\left(T_f - T_\infty\right) = \frac{1}{1 + aY_{Fb}} \left[c_p(T_s - T_\infty) - Y_{Fb} \Delta h_c (1 - X_r)\right] \tag{6.18}$$

Now, a radiative extinction limit range is found for each X_{O2}.

The procedure to compute the extinction limits is summarized here. Assuming steady state, we iterate mass flux and calculate L that corresponds to high mass flux, or radiative extinction limit.

- Given parameters: X_{O2}, p, T_s, and Δh_c.
- Thirteen Equations: Flame height, X_r, T_f, $\overline{\dot{q}''_{f,c}}$, $\overline{\dot{q}''_{f,r}}$, $\dot{q}''_{rr}$, L with T_f chosen as 1100 K or 1200 K
- The number of unknowns is thirteen ($x_f, r_f, \kappa, F_{f\to s}, \Omega, A_f, X_r, T_f, \overline{\dot{q}''_{f,c}}, \overline{\dot{q}''_{f,r}}, \dot{q}''_{rr}, \dot{m}'', L,$) The Eqns. (6.6 to 6.18) have enough information to solve for mass fluxes that satisfy the nonlinear algebraic set.
- Excel solver is utilized to guess mass flux and converge to a value that corresponds to the critical T_f (1100 K or 1200 K); It results in the points on the radiative limit.

2. Small flame extinction limit range is obtained by following the same procedure for the radiative extinction limit, i.e., through Eqns. (6.6 to 6.17). As will be shown in the Figs. 6.9 to 6.11, middle plot, flames can be extinguished from radiative heat loss and heat loss to the burner surface. Both extinction limits correspond to flame cooling down to the mentioned critical flame temperature range. Therefore, the optimizer outputs are two mass fluxes, the maximum $\dot{m}''$ that corresponds to radiative extinction limit, and the minimum $\dot{m}''$that corresponds to small flames extinction limit.

3. Pure convective extinction limit is a hypothetical ideal case, obtained based on refs. [67,76]where small flames are assumed to have no radiative heat loss (and thus no radiative heat flux to the fuel source) and the conductive heat loss to the fuel source causes the flame temperature to drop down and chemical reaction stops. The convective extinction limit is found by plugging in the critical flame temperature of 1100 K in the analytic solution for flame temperature and neglecting X_r, $\dot{q}''_{rr}$, and $c_p(T_s - T_\infty)$. The formulation is shown in Eqns. 6.19 to 6.21.

$$L_m = L + \frac{\dot{q}''_{rr}}{\dot{m}''} \tag{6.19}$$

$$c_p\left(T_f - T_\infty\right) = \frac{\Delta h_c - L_m - c_p(T_s - T_\infty)}{1 + \frac{\Delta h_c}{\mathrm{Y_{O2}}\Delta h_{c,O2}}} \tag{6.20}$$

$$\Delta h_c = \frac{c_p\left(T_f - T_\infty\right) + L}{1 - \frac{c_p\left(T_f - T_\infty\right)}{\mathrm{Y_{O2}}\Delta h_{c,O2}}} \tag{6.21}$$

On each flammability map shown in Figs. 6.9 to 6.12, two red curves indicate radiative extinction limit range for 1100 and 1200 K, and the two light blue curves correspond to small flame extinction limit range, accordingly. The pure convective extinction limit shows an ideal case where flames are so small that negligible radiative heat loss is emitted from the flames. The critical flame temperature of 1100 K, results in a larger flammable zone, i.e., the zone in between the two outer extinction limits, and the 1200 K results in a smaller flammable zone. As the ambient X_{O2} is

decreased the flammable zone area is decreased and the critical extinction range is increased. This shows

Where $\Delta h_{c,O2} = \Delta h_c/S = 13.76\, kJ/g$. There are also theoretically prediction curves shown on each plot shown by either dashed or solid-colored lines indicating the general trend. For the theoretical lines, the calculated L introduced in previous section are used.

Figs. (6.9 to 6.11) presents three flammability maps for ambient nominal X_{O2} of 0.4, 0.34 and 0.265 shown in the top. The p was shown to have minimal effect on burning conditions [51,52]. The three ambient conditions are chosen to match the conditions where, steady flames were observed in the experiments. The dashed horizontal lines shown on the plots indicate theoretical predictions for the range of flammability for each heat of combustion. The criterial for identifying steady flames were like that shown in the previous chapters, using a critical temperature range of 1100 to 1200 K. The radiative extinction limit shifts to the higher L, that is equivalent to lower mass burning rate, as heat of combustion is increased resulting in a slopped line shown on the flammability maps. The reason is that as heat of combustion is increased the flame size gets larger for the same mass burning rate. Therefore, the radiative extinction limit occurs at higher heats of gasification as heat of combustion is increased.

The radiative loss fraction, X_r, can be predicted by using the correlation introduced in [52] that was adjusted by adding more data [60]. The trends of X_r against L are shown for each Δh_cintroduced in the flammability maps (The middle plot of Figs. 6.9 to 6.11). It illustrates the trend of X_r for each horizontal line on the flammability maps (indicating constant heat of combustion). At low L as expected, the self-extinguished data points are observed until the first steady flames are observed at X_r of ~ 0.65 for X_{O2} of 0.4, ~ 0.6 for X_{O2} of 0.34 and ~ 0.55 for X_{O2} of 0.265. X_r is decreased monotonically with L and is increased with Δh_c. The modeled X_r shown by colored lines confirms these trends.

The flame temperatures at flame sheet, T_f ,assuming complete reaction are calculated [49,52] and shown on the bottom plots of Figs. 6.9 to 6.11. The trends shown by calculated T_f, are accompanied by more scatter that reveals the limitations of using a theoretical model that uses constant properties (i.e., c_p and k for Nitrogen at 1400 K) to estimate flame properties. However, it gives valuable information of how flame temperature behaves by changing heats of combustion and heats of gasification, as the two key material properties used for burning emulations. Calculated T_f is increased by heat of combustion but first increases by heat of gasification until it reaches to its peak and then starts to decrease suggesting a parabolic shaped curves when plotted against heat of gasification. The reason for having a dome shaped curve is that there is a tradeoff between the sources of flame heat loss. For low heats of gasification, the flames are closer to their radiative extinction limit and cool down due to radiative heat loss compared to the small flames with higher heats of gasification, where heat loss to the fuel source is dominant and causes flame cooling down. At some point, the two sources of heat loss provide a situation in favor of T_f and thus, steady burning. The peak temperature moves to the right of the plots as heat of combustion is increased. By comparing the plots presented in the bottom of Figs. 6.9 to 6.11, one finds out that decreasing the ambient nominal X_{O2} decreases the steady flame temperature. Theoretical predictions shown by solid-colored lines confirm such a trend.

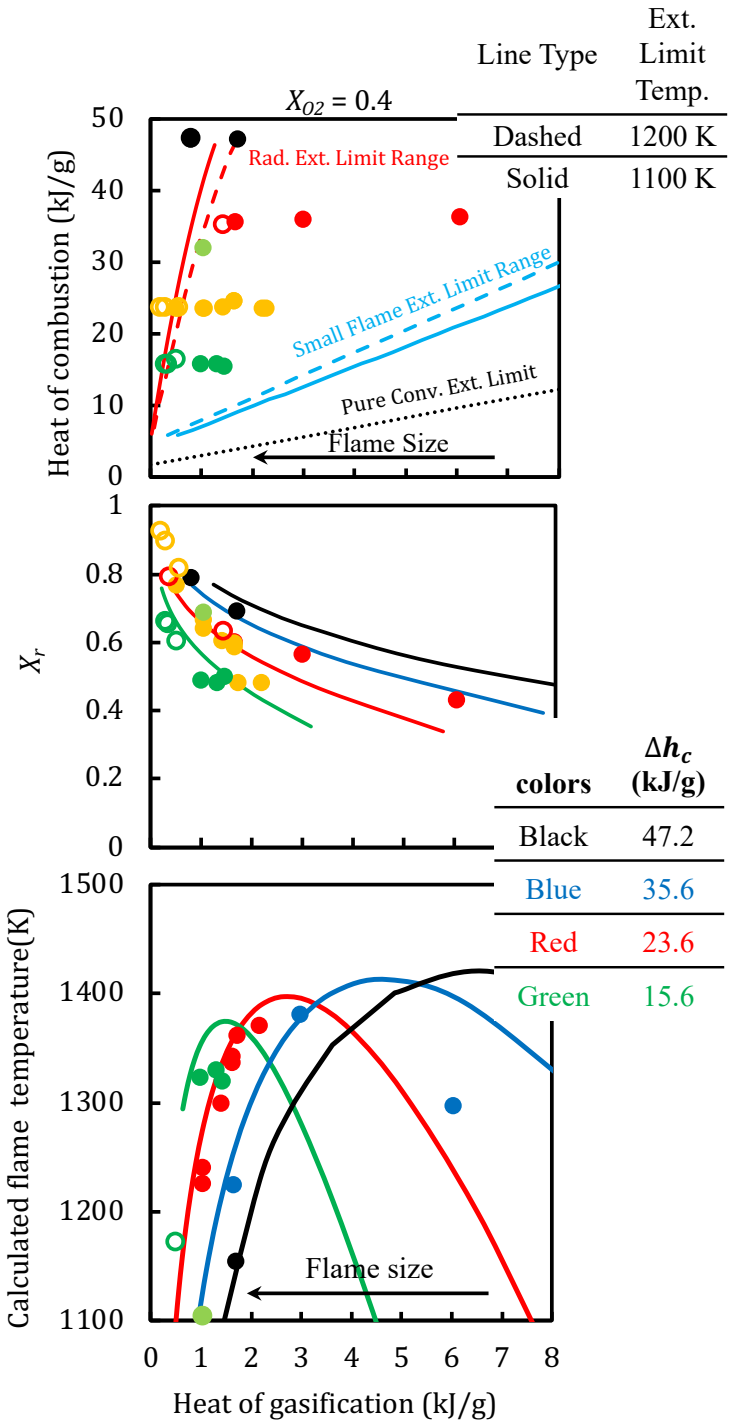

Figure 6.9. The flammability map for nominal X_{O2} of 0.4 along with trends of calculated X_r, and calculated T_f at flame sheet for steady flames generated by ethylene-diluent mixture and 25 mm burner.

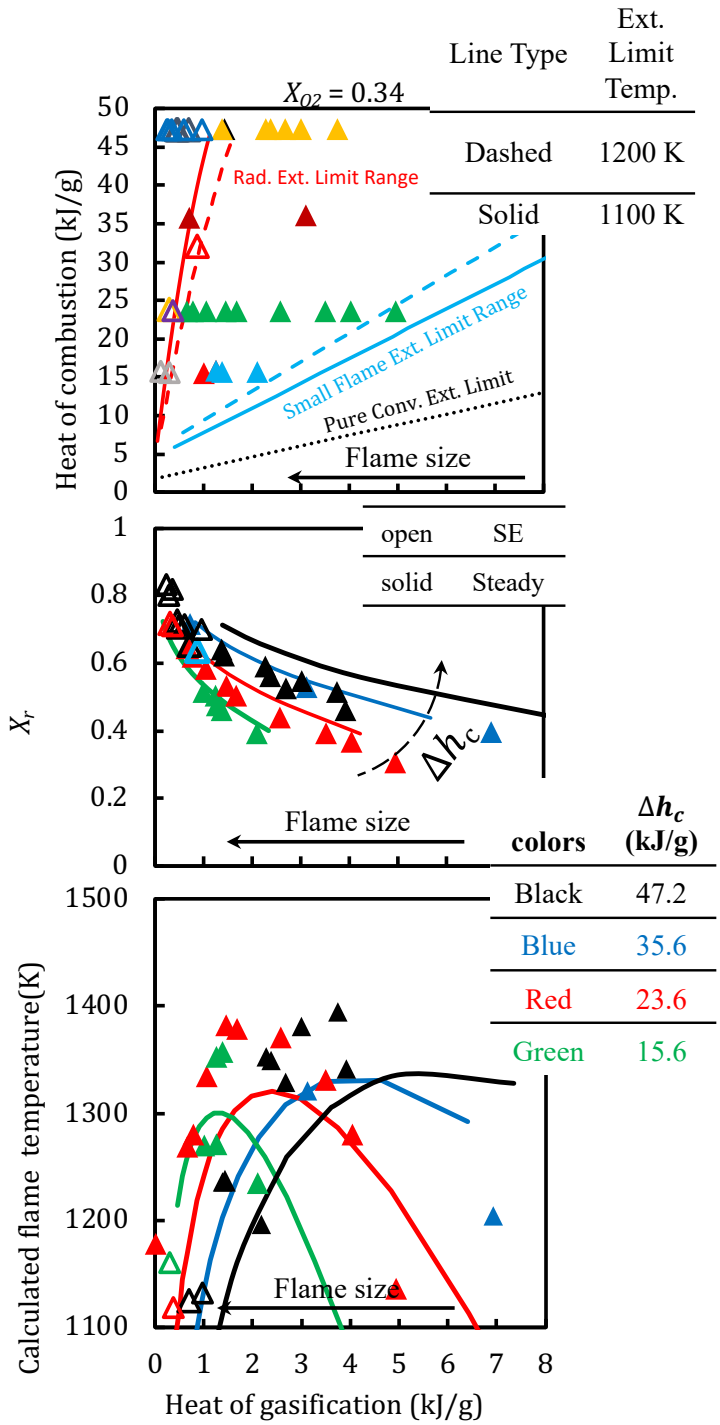

Figure 6.10. The flammability map for nominal X_{O2} of 0.34 along with trends of calculated X_r, and calculated T_f at flame sheet for steady flames generated by ethylene-diluent mixture and 25 mm burner.

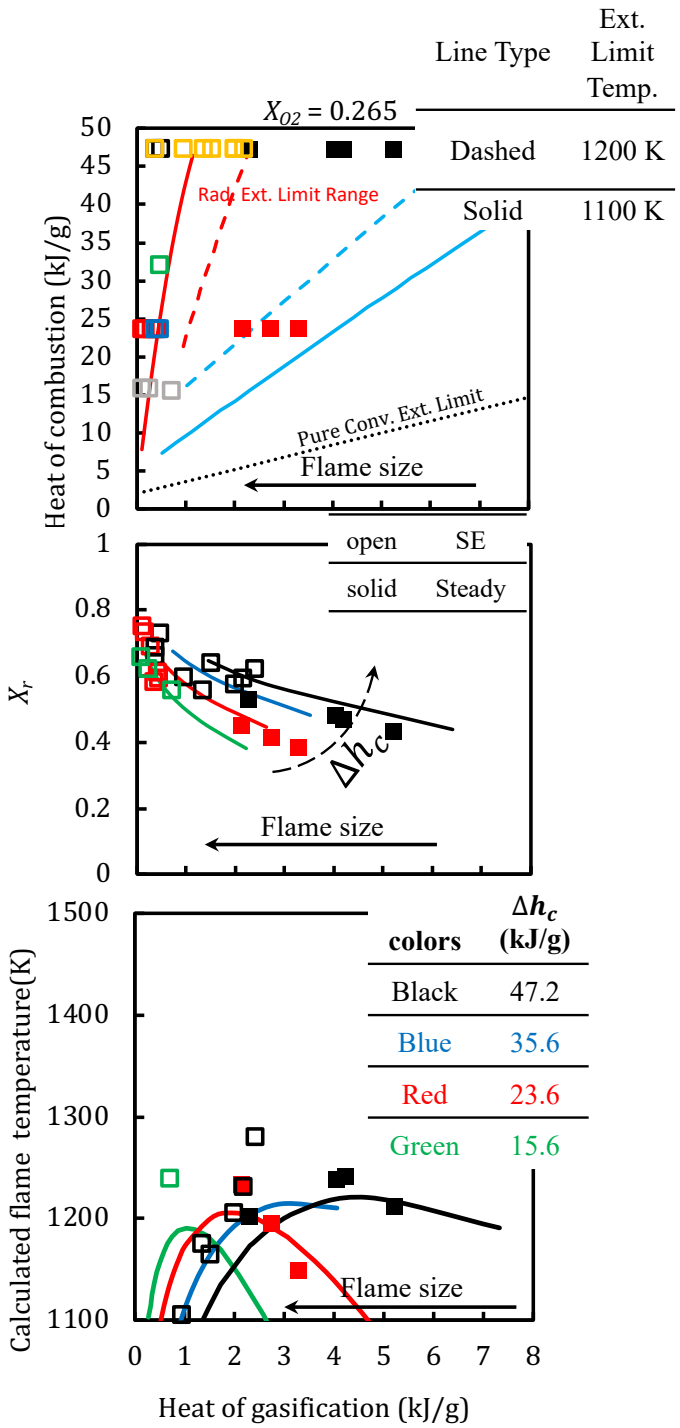

Figure 6.11. The flammability map for nominal X_{O2} of 0.265 along with trends of calculated X_r, and calculated T_f at flame sheet for steady flames generated by ethylene-diluent mixture and 25 mm burner

Figs. 6.9 to 6.11 elaborated the trends of T_f and X_r for each X_{O2} and Δh_c. Now, the effect of X_{O2} on the T_f is shown in Fig. 6.10. As expected, oxygen enriched environments, generally increase the flame temperature which is more hazardous. To minimize the effect of Δh_c, and see the effect of X_{O2} more clearly, the abscissa of the plots shown in Fig. 6.12, is chosen to be $L/\Delta h_c$ which resulted in collapsing the T_f curves in a narrower range. However, Δh_c still affects these curves through changing the X_r which explains the small horizontal displacement of these curves.

Table 6.2 shows some of the widely used material L and Δh_c. These quantities are material properties and thus can be obtained by cone calorimeter in normal gravity as explained in the introduction. The BRE experiments are focused on emulating such material generated flames by matching L, Δh_c, T_b, *and* l_s (laminar smoke point). Again, T_b is the material burning temperature that is related to the un-controlled burner surface temperature. It was shown that the normal gravity emulations were successful without matching T_b. Smoke point was not applicable to microgravity flames because no soot was observed at steady state and emulation was performed by matching the two significant material properties, L and Δh_c, that are used as the axis of the flammability maps for X_{O2} of 0.265, 0.34, and 0.4. This allows showing material properties as "crosses" on the flammability maps while the other colored symbols are burner generated flames, all shown in Fig. 6.13. For example, let us take PMMA that is close to a yellow circle (X_{O2} of 0.4), a green triangle (X_{O2} of 0.34), and a red square (X_{O2} of 0.265). For the first two case, the corresponding test is the

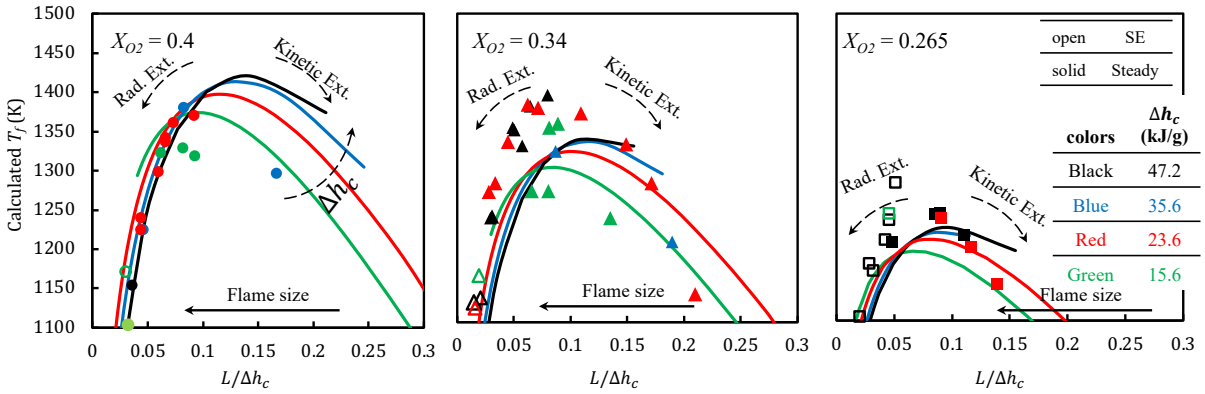

Figure 6.12. The calculated flame temperature plotted against $L/\Delta h_c$ for nominal X_{O2} of 0.4, 0.34, and 0.265

PMMA emulated flame and since it falls in the flammable zone, the region in between the radiative and pure convective extinction limits shown by slopped lines, it suggests that PMMA burns steadily at X_{O2} of 0.4, and 0.34. But, for the last case, X_{O2} of 0.265, since the PMMA point falls in the extinction zone, the region to the left of radiative extinction limit.

In general, materials that fall in the flammable region identified in Figure 6.13, that have high Δh_c and low *L,* such as PE and PP impose more risk to the fire-safety of spacecrafts because of higher heat release rate, and larger size that can better reach the surrounding and have more radiation emittance, an important factor for fire growth and spread.

The radiative, small flame, and pure convective extinction limits are based on theory [52], and there are some steady flames in the extinction region. Also, the horizontal double solid line indicates the minimum Δh_c, required for ignition that was observed in the experiments. It shown that the minimum Δh_c, required for ignition increases slightly from 10 to 12, and 13 when X_{O2} is decreased from 0.4, to 0.34, and 0.265, respectively. This limitation is due to the approximate nature of the calculated values, especially, average surface radiative heat flux. Also, the Y_{O2} are assumed to be constant and at their nominal values of 0.43, 27, and 29 compared to the actual experimental values that deviate up to 10% from their nominal value at the end of each test. This explains the inaccuracy observed in the flammability maps related to the extinction limits.

Table 6.2. Some of the commonly used materials heats of combustion and heats of gasification [67,74]

Materials	Δh_c kJ/g	L kJ/g
Liquids		
Acetone	30.8	0.63
Ethanol	26.8	1.00
Methanol	19.8	0.74
Ordinary Polymers		
Epoxy	25	2.3
PE, Polyethylene	43.4	1.9
HDPE, High density polyethylene	40	2.0, 2.2
PP, Polypropylene	44	2.0
Nylon 6	28.8	1.4
PMMA	24.2	1.6
Textiles		
Acrylic fiber	27.5	4.6
Wool	19.5	3.9

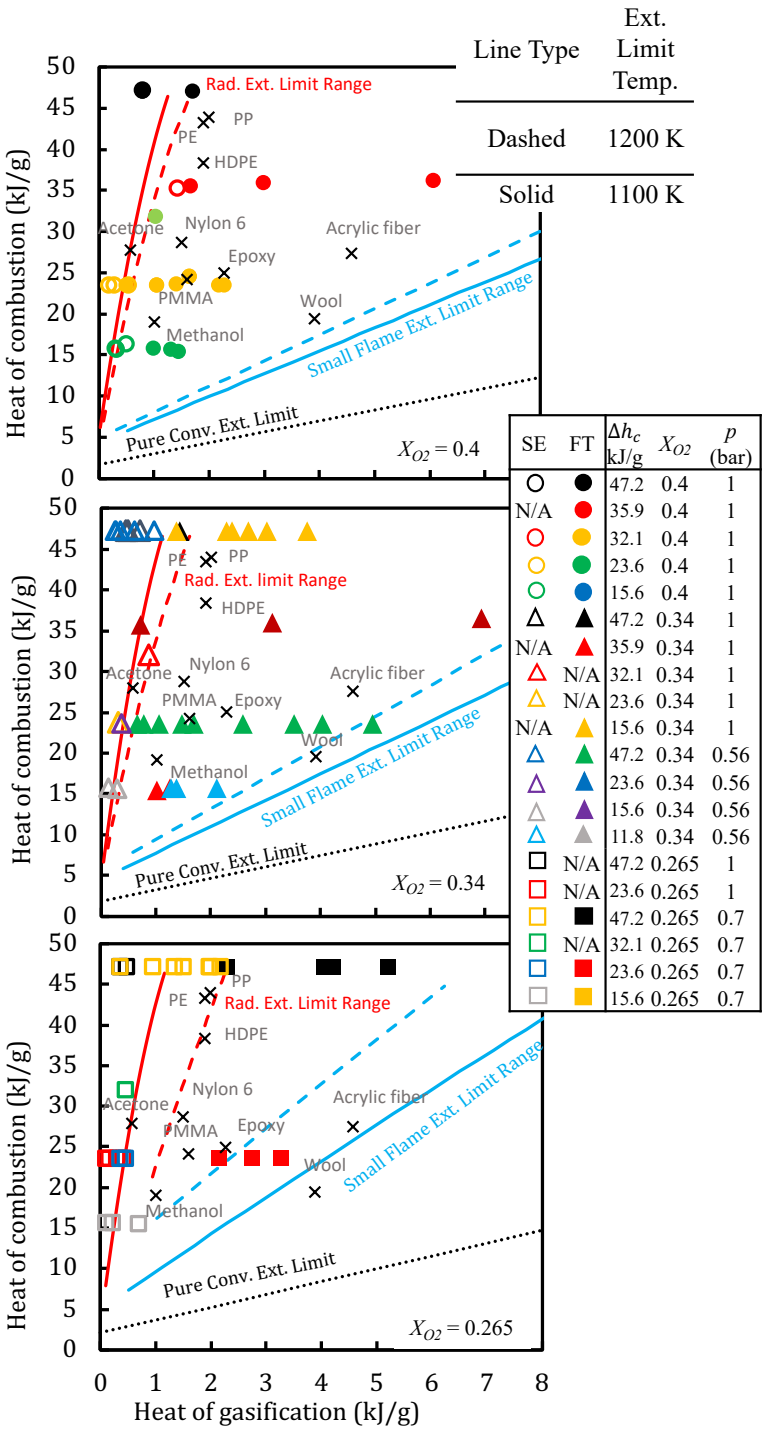

Figure 6.13. The flammability map for nominal X_{O2} fractions of 0.4, 0.34, and 0.265 along with real material properties shown as colored crosses.

Now, all the extinction limits for each X_{O2}, and for the critical flame temperatures of 1100 K, and

1200 K are shown in Fig. 6.14. First, generally the flammability region is decreased when the X_{O2} is decreased, i.e., the extinction limits get closer to each other as oxygen concentration is reduced. The radiative extinction limit does not change much when the T_{cr} = 1100 K but it changes significantly when T_{cr} = 1200 K, and for the lowest X_{O2}. On the other hand, the small flame extinction limit always tends to narrow down the flammability region as X_{O2} is reduced which suggests the higher dependency of this limit to the ambient oxygen. The same approach was used to plot the extinction limits and thus, a theoretical flammability region for X_{O2} = 0.15, which confirmed that there is no flammable region for that ambient condition.

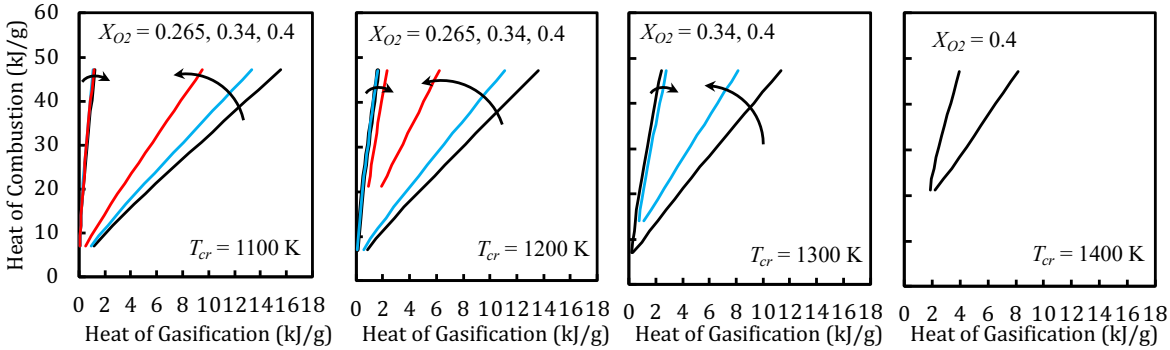

Figure 6.14. Flammability regions dependency on the nominal X_{O2}, shown for the critical flame temperatures of 1100 K, to 1400 K

The choice of critical temperature affects the flammability region. The widely used range as discussed herein is 1100 to 1200 K. However, the computation algorithm allows obtaining a flammability region based on the given critical temperature. The flammability map was shown for critical temperatures of 1100, 1200, 1300, and 1400 K. The extinction limits get closer to each other as the critical temperature is increased. For the T_{cr} = 1300, and 1400 K, no flammable zone was found at X_{O2} = 0.265, and X_{O2} = 0.265, and 0.34, respectively. The maximum achievable flame temperature in an ambient with X_{O2} = 0.4, was found to be 1420 K. In other words, for the ambient conditions considered in this study, the flame temperatures did not exceed 1420 K. The effect of

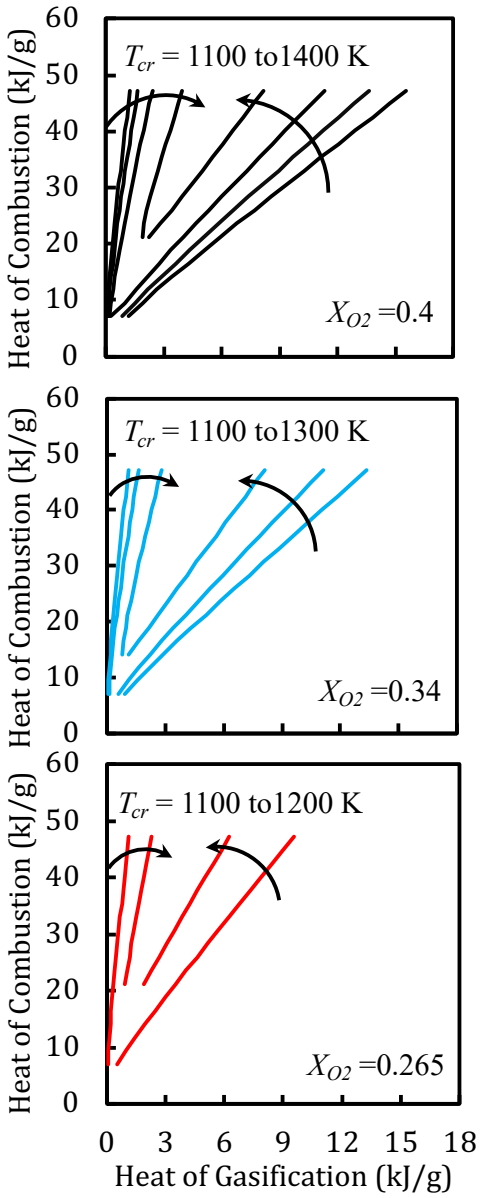

Figure 6.15. The effect of T_{cr} on flammability maps for X_{O2}= 0.265, 0.34, and 0.4 (shown for the critical flame temperatures of 1100 K, to 1400 K)

critical temperature on the flammability maps for ambient with X_{O2} = 0.265, 0.34, and 0.4 are shown in the Fig. 6.15.

6.8 Critical heat release rate, and mass flux at extinction limits

The critical heat release rate, $\dot{m}''\Delta h_c$, corresponding to the critical flame temperatures (1100 K or 1200K) used in this analysis is plotted against heat of combustion. It is observed that for the small flame extinction limit, the critical heat release rate corresponding to both critical temperatures approaches ~40 kW/m^2. Critical HRR at extinction was also observed in [75,95]. However, for the radiative extinction limit the critical heat release rates increase significantly with X_{O2} (See Fig. 6.16).

Critical mass flux at the extinction limits is plotted and shown in Fig. 6.17. At the small flame extinction limit, the critical mass flux does not change with X_{O2} except that as X_{O2} is decreased the combustible range for heat of combustion decreases. In other words, higher oxygen concentration allows for materials with lower heats of combustion burn. Therefore, the critical mass flux as a function of Δh_c for the small flame extinction limit can be defined with a single power-law fit as shown in the Fig. 6.17, similar to what was obtained in [75]. At the radiative extinction limit, the critical mass flux, increase with oxygen for a given Δh_c. Also, the flammable range of Δh_c is increased with X_{O2}.

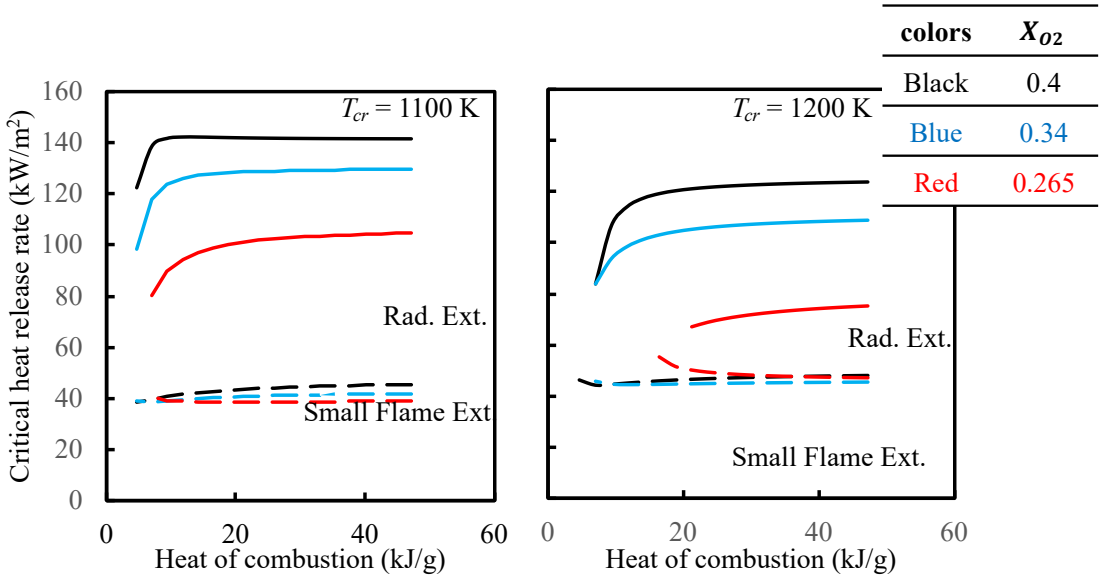

Figure 6.16. Critical heat release rate as a function of heat of combustion shown for different X_{O2} for the two extinction limits (radiative extinction, and small flame extinction limit).

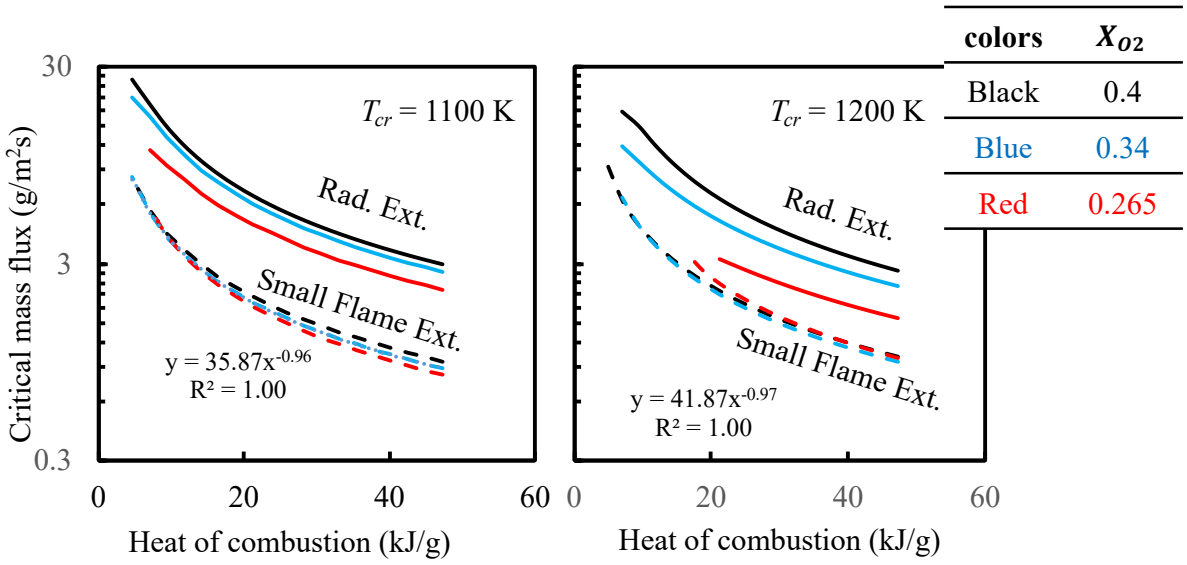

Figure 6.17. Critical burner mass flux as a function of heat of combustion shown for different X_{O2} for the two extinction limits (radiative extinction, and small flame extinction limit). The fit shown corresponds to the small flame limit

6.9 Chapter summary

A gas fuel supplied burner (BRE) was used to emulate burning of real solid and liquid fuels in microgravity to address the concerns regarding fire safety of spacecrafts. The burner had a porous surface that allowed gas mixture flowing which represents real material gasification. The gaseous fuel used in this study were ethylene and ethylene diluted with nitrogen to generate a range of heat of combustion (*LHV*) from 10 kJ/g to 47.2 kJ/g. The BRE was installed inside a chamber that allowed ignition of flames in a controlled environment. The oxygen mole fraction and pressure were varied to study its effect on the flammability of the fuel mixture flow. The nominal ambient oxygen mole fractions used in this study were 0.4, 0.34, 0.265, 0.25, and 0.21 with ambient pressures of 1, 0.7, and 0.56 bar. Three of the atmospheres used were conditions that NASA is considering for human habitat in space crafts. Several cameras recorded still images and videos of the tests. Two heat flux sensors and two K-type thermocouples embedded to the burner surface were used to measure surface heat flux and temperature at the center and approximately 10 mm from the center of the burner. Several remote radiometers measured radiative heat flux from the flames that led to computation of radiative loss fractions, a quantity that was used to correct the

heat of combustion in the analytical solution to the BRE flames. A critical temperature range of 1100 to 1200 K, was chosen to distinguish between self-extinguished and steady flames. 146 flames were ignited aboard the international space station. All flames that were ignited at nominal X_{O2} of 0.25, and 0.21 self-extinguished within 90 seconds. 46 flames burned for the entire duration, three minutes for most of the cases, before the fuel supply was terminated intentionally. These flames were close to their steady state value, and it was shown by the analytical solution, with their size being 94% of their steady state value on average and standard deviation of 1.9%. Average measured heat flux was used to obtain heats of gasification, a key parameter for fuel emulation. A dimensional analysis of the radiative loss fraction X_r based on radiation theory led to an empirical correlation. A geometrical model was used to estimate surface average radiative heat flux that resulted in computation of heat of gasification when added to the calculated convective and re-radiative surface heat flux. The computed heats of gasification were compared with measured counterparts for the steady flames indicating good accuracy of the model used. Finally, a flammability map, as a plot of Δh_c vs. L (the two key properties of materials that are used for emulation) was obtained for each nominal oxygen mole fraction, based on the experimental data and the theoretical predicted trends were shown for elaboration. Two extinction limits were introduced that identifies the flammability region. The radiative extinction limit was obtained empirically, by passing a line through a range that segregates self-extinguished and steady flames. The kinetic extinction limit was obtained theoretically for small flames, having small radiative heat loss. The properties of some of the real solids and liquids were shown on the flammability maps to study their flammability.

7. Conclusions

Burning emulation in microgravity is investigated through a series of tests aboard the International Space Station to study flammability of condensed phase materials in quiescent atmosphere to improve safety of spacecrafts against fire hazard. Two sizes of the Burning Rate Emulator (BRE) were utilized to emulate burning of condensed phase materials with porous flat surfaces of 25 mm and 50 mm in diameter. Ethylene, and a diluted mixture of these fuels with nitrogen at different concentrations were used to achieve a range of heats of combustion of up to *LHV* of 50 kJ/g. The fuel mixture mass flux, ambient mixture and ambient pressure were among the design parameters. Radiation measurements were performed to obtain flame radiative loss fractions. A dimensional analysis of radiation fraction led to an empirical correlation. RADCAL, a narrow band radiation model, was utilized to obtain flame emissivity by executing the code with partial pressures of products, flame length, flame temperature and ambient pressure being input parameters. The correlation allowed correction of total heat release rate from the flames due to radiative loss and when combined with the analytical solution to these flames, allowed prediction of flame heights, radius, average convective and radiative heat flux that were used to calculate heats of gasification. In the burning emulation, the mass flux was specified, and the heat of gasification was derived, in the real problem, the heat of gasification is given and the question of burning arises. This question is resolved by assuming a flame extinction temperature.

More than half of the tests resulted in long burns of at least 2 and as long as 5 minutes. Generally, it has been found that nominal oxygen mole fractions of 26 % and above can lead to steady flames which are thin blue in color and grow slowly over time for minutes. Theoretical analysis showed the shutdown flames were effectively steady in size, and all of the test endpoints were more than 94 % of steady state in flame heat flux based on theoretical estimation of flame steadiness. The key representative property of the steady state is the heat of gasification. This is exact for vaporizing solids and approximant under real pyrolysis conditions. Surface heat flux for set mass flux allowed the estimation of heats of gasification to relate to steady solid materials that might burn in microgravity. PMMA and POM were successfully emulated based on the flammability map achieved. Radiometers allowed the computation of flame radiative fraction that

appeared to correlate well with the measured flame height which led to a more accurate correlation based on dimensional analysis by also taking into account the effect of fuel and ambient mixture and ambient pressure. Heat flux, flame height and base radius, radiative fraction as a function of fuel mixture mass flux, and several ambient mixtures and pressures are presented as experimental findings.

It is observed that for all steady flames, radiation fractions remained below 0.6 for the steady flames and correlate with the flame height. The dimensional analysis on the radiation parameter Ω confirms that it does depend on the fuel, and here only ethylene-nitrogen mixtures were examined. It is shown that if the RADCAL output absorption coefficients are divided by sum of partial pressures of water vapor and carbon dioxide, all data will collapse on an empirical curve that suggests it only depends on path length for a given hydrocarbon. Being able to calculate radiation fraction led to computation of flame temperature in which 1100 K is taken as a criterion for flame extinction. The radiation heat flux to the surface is computed based on a geometrical view factor analysis performed on calculated flame size along with the correlated X_r to calculate radiant heat flux to the surface. The net heat flux is composed of the algebraic sum of convective, radiative and re-radiation from surface which allows computation of heats of gasification. Burner size, surface temperature (350 ºC that represents real fuels burning) effects on the theoretical flammability map ($L \ vs \ \dot{m}''_{mix}$) are also investigated. It is shown that as burner diameter is increased, flame radiant fraction is increased, and heats of gasification are decreased. Surface temperature introduces substantial change in heat of gasification in which re-radiation heat loss decreases the burning rates. However, external radiation can offset this effect, and increase the mass flux. As in Earth-based fires, external radiation is the key to massive fire growth; it is likely this can be an issue in microgravity as well. The analytical algorithm given in this thesis has been shown to predict steady conditions of burning for a surface of 25 mm diameter and has been examined for larger diameters. This analysis gives one a powerful analytical tool to predict the steady burning in microgravity as a function of fuel properties and ambient conditions.

The trends suggested by the theoretical predictions in terms of ambient conditions, fuel properties, and surface diameter are presented in Table 6.1 that shows
the increase (+) and decrease (-) trends for the key parameters of burning as a function of specified burning rate, pressure, oxygen concentration, and heat of combustion. The effect of dropping the atmospheric pressure tends to expand the range of burning to higher burning rates. As NASA seeks

Table 7.1 Effect of atmosphere, heat of combustion and mass flux on burning parameters

Parameters	Pressure	Ambient Oxygen mole fraction	Fuel Heat of Combustion	Burning mass flux
Flame radiation fraction	+ and expands	+	+	+
Flame size	expands	-	+	+
Convective heat flux	expands	+	-	-
Radiation heat flux	expands	+	-	-
Heat of gasification	expands	+	-	-

to provide habitable atmospheres of lower pressure and higher oxygen levels. Such a move will exacerbate the burning conditions. The steady flame temperature is independent of the heat of gasification as given herein but depends on the mass flux. The mass flux does depend on L, as well as the steady flame temperature, surface radiative and convective heat flux, re-radiation, and external radiant heat flux. Surface radiative heat flux is inversely proportional to the mass flux (and thus, flame size) but it is decreased at a higher rate compared to convection and re-radiation. Furthermore, it is the only heat flux component that is affected by ambient mixture and pressure as well as hydrocarbon properties. Hence, radiative heat transfer is responsible for determining extinction and in case of sustained burning, the mass flux. Therefore, the algorithm should be cast in terms of the ambient conditions, including external radiation, and hydrocarbon properties to determine if burning is possible and at what rate. The significant result of theoretical aspect of this study is presented herein as a flammability map that would give burning conditions for a given fuel in terms of its heat of combustion, heat of gasification and burning temperature.

A flammability map as a plot of heat of gasification vs. heat of combustion was developed based on the measurement and theory for nominal ambient oxygen mole fractions of 0.265, 0.34, and 0.4. The flammability maps were bounded by two extinction limits, radiative, and small flame

extinction limits. The extinction limits were theoretically obtained by applying critical flame temperature of 1100 K or 1200 K. The flammable zone consists of flames with temperatures higher than these values. Several real materials were emulated by matching their properties with the flammability maps. The development of flammability maps based on Δh_c, and L, properties that can be effectively measured by the Cone Calorimeter, suggests NASA to use Test 2 to determine flammable hazard in space. Also, the effects of external radiation, and real material chemistry are suggested as subjects for future studies.

Appendix A. Corrections to the Calorimeter Heat Flux

The exposed side of the copper burner top provided an unwanted heat flux surface. It should have been insulated. The calorimeter can only successfully provide an average surface heat flux to the top flat flow area of the copper by eliminating the edge heating. This is done by the following analysis. It has been done for all the steady endpoints by utilizing the radiative fraction as predicted by the correlation in Figure 3.7b. This allowed for using all of the steady data, and not just where radiometers worked. Table 3.1 shows that there is very good agreement between the measured radiation fractions and those predicted by the correlation.

The radiation is analyzed in terms of view factors with the flame treated as a surface, 2, as shown in Figure A.1. Two cases need to be investigated in this analysis: (a) the flame extends below the flow area, surface 1; and (b) the flames standoff surface 1. Video images of the flames allowed measurements for the dimensions *a* and *b* along with the flame height and radius are given in Table 3.1.

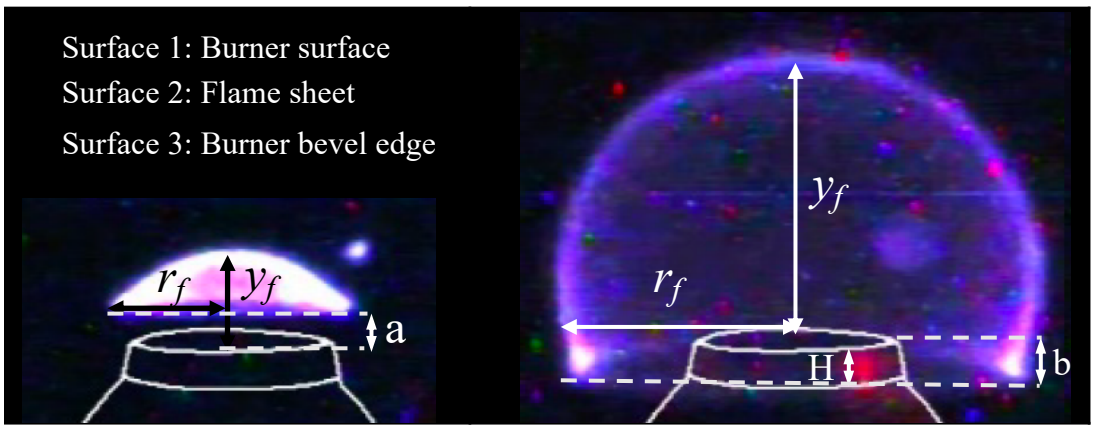

Figure A.1. Flame configurations for analyzing heat flux from 2 to 1 and 3

The analysis proceeds in several steps. (See nomenclature for guidance). Dependence of convective flame heat flux to surfaces 1 and 3 is inversely related to distance from the flame:

$$\overline{\dot{q}''}_{1,c} \propto \frac{1}{y_f}\left(\frac{\lambda}{e^{\lambda}-1}\right) \qquad (A.1)$$

Flame below (adjusted for not full coverage over *H*)

$$\overline{\dot{q}''}_{3,c} \propto \frac{\frac{b}{H}}{(r_f - R)} \tag{A.2}$$

Flame above (considering the average distance 3 is from the flame)

$$\overline{\dot{q}''}_{3,c} \propto \frac{1}{a + \left(\frac{H}{2}\right)} \tag{A.3}$$

Flame radiant heat rate and heat flux to surface 3

$$\dot{q}''_3 = \frac{X_r \dot{Q}_c}{2} F_{23} \tag{A.4}$$

$$F_{23} = \frac{A_3}{A_2} F_{32} \tag{A.5}$$

$$\dot{q}''_{3,r} = \frac{X_r \dot{Q}_c}{2A_2} F_{32} \tag{A.6}$$

$$F_{32} \approx 1 - \frac{R}{r_f} < 1 \tag{A.7}$$

Ratio of radiation heat flux to convection heat flux for surface 1 Theoretical convection is given as

$$\overline{\dot{q}''_{1,c}} = \left(\frac{4k}{\pi R c_p}\right)\left(\frac{\lambda}{e^{\lambda} - 1}\right)\left[\frac{\Delta h_c (1 - X_r) Y_{O,\infty}}{S - c_p (T_s - T_\infty)}\right] \tag{A.8}$$

Theoretical radiation is given as

$$\dot{q}''_{1,r} = \frac{X_r \dot{Q}_c}{2A_2} F_{12} \tag{A.9}$$

where A_2 is the flame area based on the surface of a semi-ellipse defined by semi-major axis y_f and semi-minor axis, r_f. If the flame resides above the burner surface, Eq. A.10 is used to obtain the view factor

$$F_{12} \approx 1 - \frac{\arctan\left(\frac{a}{r_f}\right)}{\pi} \tag{A.10}$$

And when the flame is below the surface,

$$F_{12} = 1 \tag{A.11}$$

For the following, define

$$\mu = \frac{\dot{q}''_{1,r}}{\dot{q}''_{1,c}} \tag{A.12}$$

The correction algorithm is given as follows:

$$\dot{q}''_1 = \delta \dot{q}''_{cal} \tag{A.13}$$

$$\delta = \frac{(1+\ \mu)(A_1 + A_3)}{(A_1 + \alpha A_3) + \mu(A_1 + \beta A_3)} \tag{A.14}$$

For the flames above the burner, we use eq. A.15

$$\alpha = \frac{\dot{q}''_{3,c}}{\dot{q}''_{1,c}} = \left[\frac{1}{\alpha + \left(\frac{H}{2}\right)}\right] / \left[\frac{1}{y_f}\left(\frac{\lambda}{e^{\lambda} - 1}\right)\right] \tag{A.15}$$

And for the flames below the burner, we use eq. A.16

$$\alpha = \frac{\dot{q}''_{3,c}}{\dot{q}''_{1,c}} = \left[\frac{\frac{b}{H}}{r_f - R}\right] / \left[\frac{1}{y_f}\left(\frac{\lambda}{e^{\lambda} - 1}\right)\right] \tag{A.16}$$

$$\beta = \frac{\dot{q}''_{3,r}}{\dot{q}''_{1,r}} \tag{A.17}$$

$$\mu = \left(\frac{\dot{q}''_{1,r}}{\dot{q}''_{1,c}}\right)_{theory} \tag{A.18}$$

The results for the heat flux to surface 1 alone (corrected calorimeter heat flux), $\dot{q}''_{cal,crc}$, and the original calorimeter heat flux, $\dot{q}''_{cal}$.are presented in table 3.1. Also, calorimeter data are shown in figure A.2 for those tests that radiation measurements were available.

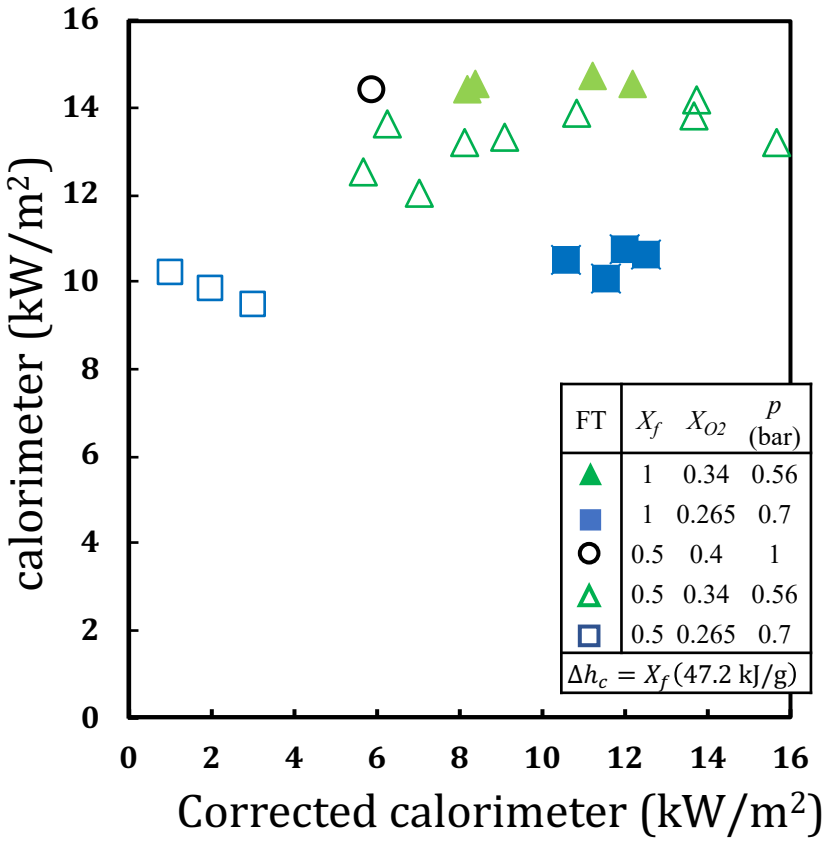

Figure A.2. Calorimeter vs. corrected calorimeter

Appendix B. Transient Flame Size and PMT with OH* Filter Assembly

In-order to illustrate the asymptotic behavior of BRE microgravity steady flames, the transient plots of flame length, base radius and PMT with OH* filter assembly (that represents flame luminosity) of test point 66D5 are presented in Figure B.1. The details of PMT calibration and schematic is presented in ref [55].

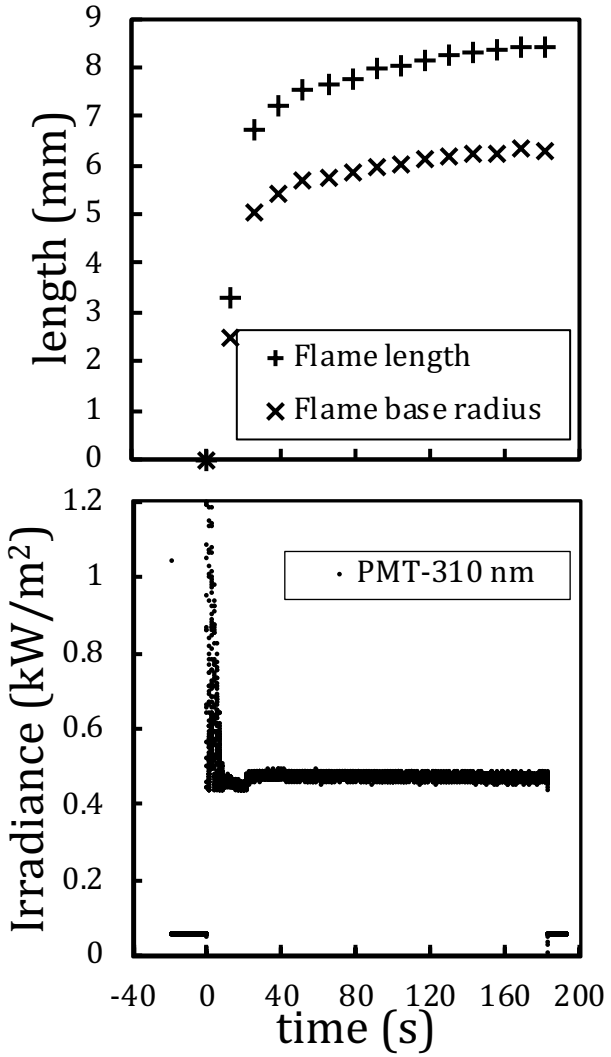

Figure B.1 Transient flame length, base radius and PMT heat flux with OH* assembly

Appendix C. Transient results, use of theory and example predictions

In this chapter, the theory introduced in is used to predict transient flame height, X_r, calculated T_f, and surface heat flux components.

C.1 Flame Height

The analytic theory, that was used to obtain the closeness of the flame size to its asymptotic value, can predict transient flame height. The results of two tests are shown in Figure 1. Initially the size deviate from measured values but as the flames grow, the calculated value becomes more accurate. At the endpoint of all steady tests the predicted flame heights matched measured counterparts.

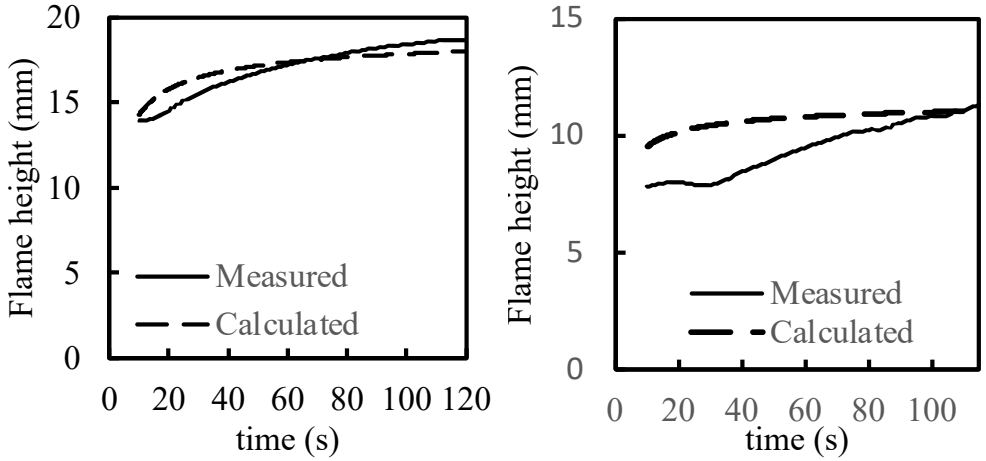

Figure C.1. Calculated vs. measured transient flame heights of 19070C1 and 20352A2

C.2 Transient radiation fraction, and calculated flame temperature

The analytical solution for the steady flame temperature was combined with transient radiation fraction and flame height to estimate the transient flame temperature at flame sheet.

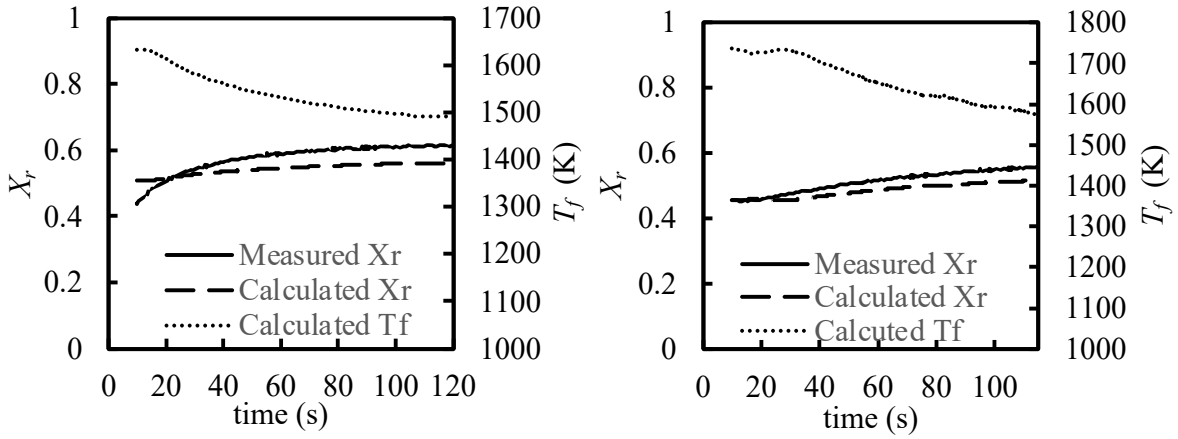

Figure C.2. Radiative loss fraction empirical correlation for steady flames generated by the 25 mm BRE burner and ethylene-diluent mixture

C.3 Transient surface heat flux components:

The surface net heat flux was measured by two het flux sensors, and the analytical solution algorithm was used to compute surface average convective, radiative, and re-radiation heat flux. The results are shown for two tests in Fig. 3.

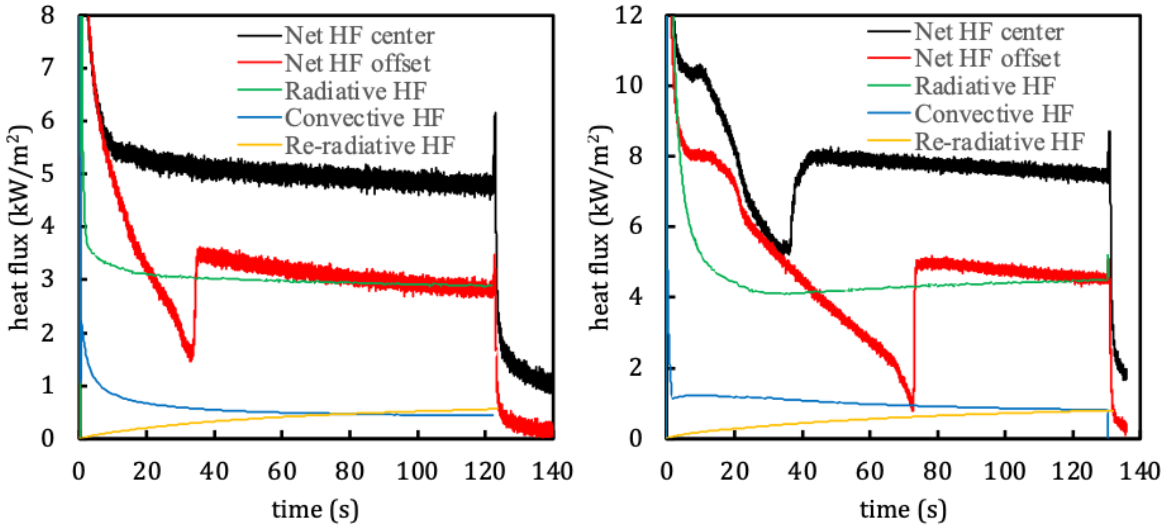

Figure C.3. Surface measured heat flux at r = 0 and 9.5 mm from center, and transient average heat flux components

Appendix D: The parameters spreadsheet submitted to NASA operations team

The parameters spreadsheet submitted to NASA operations team three business days before each test point day is presented in the table D.1 with each parameter's meaning explained in the table D.2.

Table D.1. An example of the patameters table submitted to NASA operations team before each test point day. Only two test points parameters are shown.

Parameter Name	1st test point	2nd test point
testpointName	21028A1	21028B1
preIgnitionDataTimeSec	0	0
postFlameDataTimeSec	15	15
useIPSUs	TRUE	TRUE
ipsuTimeoutSec	40	40
useAcmeCamera	TRUE	TRUE
useIntensifiedCamera	TRUE	TRUE
ipsu1ArchiveRate	2	2
dataCameraPreIgnitionExposureUs	1000000	1000000
dataCameraTestExposureUs	50000	50000
analogCameraPreIgnitionShutter	2	2
analogCameraTestShutter	2	2
intensifierGainAmplitude	50000	50000
preIgnitionImageTimeSec	0	0
postFlameImagingTimeSec	3	3
useBracketedExposures	FALSE	TRUE
bracketingImagesPerExposure	1	1
bracketingNumberOfExposures	4	4
bracketingExposureStartUsec	5000	5000
bracketingExposureMultiplierTimes100	200	200
igniterIgnitionPosition	2300	2300
igniterPreheatPowerV	3	3
igniterPreheatTimeMs	2000	2000
igniterIgnitionPowerV	3.75	3.75
igniterIgnitionDurationMs	3000	3000
igniterDelayBeforeRetractMs	3000	3000

igniterRetractVelocityCountsPerSec	3000	3000
useIgnitionDetection	TRUE	TRUE
extinctionDetectionStopsTest	TRUE	TRUE
pmt1Gain	6	6
pmt2Gain	6.25	6.25
pmt3Gain	6.25	6.25
fiberIgnitionPosition	0	10000
fiberTestPosition	0	18500
fiberMoveDuringTest	FALSE	FALSE
fiberSegmentDistance	100	100
fiberVelocity	3000	3000
fiberAcceleration	1000	1000
fiberDeceleration	0	0
fiberHoldDurationSec	1	1
fiberCycles	100	100
useFoma	TRUE	TRUE
flowTimeoutSec	160	160
nitrogenPriming1DurationSec	0	0
nitrogenPriming2DurationSec	0	0
fuelFlowIgnitionDeltaMs	26000	40000
stabilizationTime1Sec	4	4
stabilizationTime2Sec	4	4
fuelBottleIgnitionFlowRateN2Slpm	0.077	0.0513
nitrogenIgnitionFlowRateN2Slpm	0.0947	0.0632
fuelBottleTestFlowRateN2Slpm	0.077	0.0513
nitrogenTestFlowRateN2Slpm	0.0947	0.0632
ignitionToTestRampTimeSec	1	1
constantFlowTimeSec	90	90
numberOfRampHolds	0	0
rampSizePercent	-20	-20
rampDurationSec	2	2
holdDurationSec	10	10
temperatureLimitCriticalC	300	300
temperatureLimitC	250	250
useCenterThermocouple	TRUE	TRUE
useOffsetThermocouple	TRUE	TRUE
useCenterFluxThermocouple	TRUE	TRUE
useOffsetFluxThermocouple	TRUE	TRUE

preflowFlowDurationSecs	0	5
preflowFuelRateSlpm	0	0
preflowNitrogenRateSlpm	0	0.16
preflowWaitDurationSecs	0	300
Additional Required Information (hover over cells for instructions)		
Estimated Burn Time (sec)	90	90
Additional Parameters (hover over cells for instructions and options for completing these parameters)		
Chamber & GC Operations		
chamber fill pressure (psia)	14.7	
chamber fill O2%	40	
chamber fill N2%	60	
GC Sample (Before, After or No)	No	No
GC Sample Method (O2, Byproducts or Both)	N/A	N/A
Recirculation (After or No)	No	No
HiBMS Camera		
use HiBMS Camera?	no	no
HiBMS Exposure (ms)	33	33
HiBMS Illumination (backlight)	65	65
HiBMS Gain (V)	1	1
HiBMS Binning	1x1	1x1
ACME Data Camera		
dataCamera Gain	16	0
dataCamera Zoom	30000	30000
dataCamera Focus	13750	13750
dataCamera Iris	0	0
dataCamera Filter	FS	FS
Intensified Camera		
Intensified Camera Frame Rate	23	23

ACME Analog Camera (downlink video)		
Analog Camera Gain	31 dB	31 dB
Estimated Flow Calculations		
Valve Timer Time (seconds)	128	142
Est. Nitrogen Flow (liters)	0.2020	0.1629
Est. Fuel Flow Using All Parameters (liters)	0.1643	0.1214
Est. Fuel Flow Using Est. Burn Time (liters)	0.1155	0.0770

Table D.2. Explanation of the parameters used in the parameters spreadsheet (table D.1)

Parameter Name	Default Value	Typical Value	Limits on Value	Relation to Other Parameters	Meaning of Parameter
testpointName	NONE	YYGMTxx	must be 7 characters (even if not using IPSU1)		test point name that will be used by the IPSUs and ACME Data File (in the image and data file names and directories) YY = last 2 digits of year, GMT = GMT day, xx = A1, B1, C1, etc.
preIgnitionDataTimeSec	0	0			time (in seconds) ACME Data File records data before IPSUs open test point and start archiving images
postFlameDataTimeSec	15				time (in seconds) ACME Data File records data after the postFlameImagingTimeSec has elapsed which occurs after command sent to close manifolds (i.e., stop gas flow)
useIPSUs	true	true	true or false		indicates if IPSUs will be used (images archived) for the test point
ipsuTimeoutSec	40	40		useIPSUs must be true	time (in seconds) to wait for command responses from IPSUs and IPSUG when opening and starting test points
useAcmeCamera	true	true	true or false	useIPSUs & useAcmeCamera must both be true to use the ACME Camera	indicates if the ACME Camera will be used for the test point
useIntensifiedCamera	true	true	true or false	useIPSUs & useIntensifiedCamera must both be true to use	indicates if the CIR Intensified Camera will be used for the test point

			the CIR Intensified Camera	
ipsu1ArchiveRate	2	cannot be 0, must be a whole number	useIPSUs must be true	indicates that every nth HiBMS Camera (IPSU1) image is saved (archived) (e.g., 10 indicates every 10th image)
dataCameraPreIgnitionExposureUs	100000	10-60,000,000	useIPSUs & useAcmeCamera must both be true	exposure (in microseconds) of the ACME Camera prior to ignition and igniter retraction (set for imaging the igniter and ignition event)
dataCameraTestExposureUs	650000	10-60,000,000	useIPSUs & useAcmeCamera must both be true	exposure (in microseconds) of the ACME Camera after igniter retraction (set for imaging the flame)
analogCameraPreIgnitionShutter	2	see Notes for acceptable values		shutter speed of the ACME Chamber Insert Camera (ops camera - no IPSU data recorded for this camera) prior to ignition and igniter retraction (set for imaging the igniter and ignition event)
analogCameraTestShutter	2	see Notes for acceptable values		shutter speed of the ACME Chamber Insert Camera (ops camera - no IPSU data recorded for this camera) after igniter retraction (set for imaging the flame)
intensifierGainAmplitude	50000	between 2500 - 80000		CIR Intensified Camera intensifier gain setting; commanded to this value after turning off chamber LED lights; this is the actual gain value; the script will convert to counts when sending the command

preIgnitionImageTimeSec	0	0		useIPSUs must be true	time (in seconds) IPSUs record images before the CIR fuel manifold is commanded open
postFlameImagingTimeSec	3			useIPSUs must be true	time (in seconds) IPSUs record images after flow stops
useBracketedExposures	false		true or false		indicates if bracketed exposures on the ACME Camera will be used for the test point; if true, replaces dataCameraTestExposureUs
bracketingImagesPerExposure	1			useBracketedExposures must be true; when useBracketedExposures is false, parameter should be default value	number of images at each exposure before moving on to the next exposure when using bracketed exposure
bracketingNumberOfExposures	4			useBracketedExposures must be true; when useBracketedExposures is false, parameter should be default value	number of exposures when using bracketed exposure
bracketingExposureStartUsec	5000			useBracketedExposures must be true; when useBracketedExposures is false, parameter should be default value	initial exposure (in microseconds) for the ACME Camera when using bracketed exposure
bracketingExposureMultiplierTimes100	1000			useBracketedExposures must be true; when useBracketedExposures is false, parameter should be default value	value, divided by 100, that will get multiplied to the current exposure to determine the next exposure, when using bracketed exposure
igniterIgnitionPosition	0		0 - 2400 for 25mm burner 0 - 2325 for 50mm burner (Igniter Arm 1)		position (in counts) of the igniter for preheat and ignition
igniterPreheatPowerV	0		0.46 - 4.5 V		igniter power (in volts) during preheat (igniterPreheatDurationMs)
igniterPreheatTimeMs	0			time is before igniterIgnitionDurationMs	time (in milliseconds) the igniter is powered during the preheat
igniterIgnitionPowerV	3.75		0.46 - 4.5 V		igniter power (in volts) during ignition (igniterIgnitionDurationMs)
igniterIgnitionDurationMs	2000			starts relative to fuelFlowIgnitionDeltaMs; if fuelFlowIgnitionDeltaMs is positive, time starts after fuel flow starts, if fuelFlowIgnitionDeltaMs is negative, time starts before fuel flow starts	time (in milliseconds) the igniter is powered for ignition; ends early if ignition is detected
igniterDelayBeforeRetractMs	1500			time starts at the start of igniterIgnitionDurationMs	time (in milliseconds) the igniter stays in igniterIgnitionPosition before retracting

igniterRetractVelocityCountsPerSec	2000				velocity (in counts/second) used when the igniter retracts if ignition is not detected
useIgnitionDetection	true	true	true or false		indicates if Ignition Detection will be used; when ignition is detected (per the specified values), the igniter turns off and retracts
extinctionDetectionStopsTest	true	true	true or false		indicates if Extinction Detection will be used to detect flame extinction; when extinction is detected (per the specified values or when commanded by operators), the script ends the gas flow and IPSUs recording of images and continues to the end of the script
pmt1Gain	6.25		0 - 10 V		PMT1 gain during the script; set to 0 at end of script; PMT1 = 310nm, OH*
pmt2Gain	6.5		0 - 10 V		PMT2 gain during the script; set to 0 at end of script; PMT2 = Broadband
pmt3Gain	6.5		0 - 10 V		PMT3 gain during the script; set to 0 at end of script; PMT3 = 430nm, CH*
fiberIgnitionPosition	0		0 - 10000 (recommended limit)	will go to this position even if fiberMoveDuringTest is false	position (in counts) the fiber moves to prior to ignition (pre-positions the fiber so it can reach fiberTestPosition more quickly)
fiberTestPosition	0		0 - 17700 (for 25mm burner) 0 - 17500 (for 50mm burner)	will go to this position even if fiberMoveDuringTest is false	position (in counts) the fiber moves to during test point (after stabalizationTime2Sec), starting position for fiber movement
fiberMoveDuringTest	false		true or false		indicates if fiber will move back and forth during test; if true, fiber will move back and forth during the test; starts after fiberTestPosition is reached; if false, fiber will still go into test position (fiberTestPosition) but not move back and forth
fiberSegmentDistance	100		maximum value is 17700 (for 25mm burner) or 17500 (for 50mm burner) minus fiberTestPosition	fiberMoveDuringTest must be true for this value to be used	distance (in counts) the fiber moves towards the burner from the fiberTestPosition and back

fiberVelocity	3000	3000	0-3000 (recommended limit)	fiberMoveDuringTest must be true for this value to be used	velocity (in counts/second) of fiber when moving during test
fiberAcceleration	1000			fiberMoveDuringTest must be true for this value to be used	acceleration (in counts/second squared) of fiber when moving during test
fiberDeceleration	0	0		fiberMoveDuringTest must be true for this value to be used	deceleration (in counts/second squared) of fiber when moving during test
fiberHoldDurationSec	1			fiberMoveDuringTest must be true for this value to be used	time (in seconds) to hold at the innermost and outermost positions of the fiber movement
fiberCycles	100	100		fiberMoveDuringTest must be true for this value to be used	number of cycles the fiber moves; one cycle is towards the burner (number of counts in fiberSegmentDistance) and back (to fiberTestPosition)
useFoma	true	true	true or false		indicates if gas flow will be used for test points
flowTimeoutSec	120			starts when fuel flow starts (fuelFlowIgnitionDeltaMS)	total time (in seconds) gas flows during script, starting when the fuel flow starts; gas flow stops after this time if not at end of script
nitrogenPriming1DurationSec	0		if using this N2 priming, minimum value is 1; whole second resolution; if not using this N2 priming, value is 0	flows at rate specified in nitrogenIgnitionFlowRateN2Slpm; if no rate specified, this time is not included in the script	time (in seconds) for nitrogen to flow prior to the start of fuel flow; time is before IPSUs start archiving, before opening CIR fuel manifold, and before nitrogenPriming2DurationSec
nitrogenPriming2DurationSec	0		if using this N2 priming, minimum value is 0.1; tenth of a second resolution; if not using this N2 priming, value is 0	flows at rate specified in nitrogenIgnitionFlowRateN2Slpm; if no rate specified, time is included in the script	time (in seconds) for nitrogen to flow prior to the start of fuel flow; time starts after CIR fuel manifold has been opened
fuelFlowIgnitionDeltaMs	1000		positive or negative value, increments of 100 ms		time (in milliseconds) fuel (and nitrogen) flows before or after start of igniterIgnitionDurationMs

stabilizationTime1Sec	4			time (in seconds) to wait after igniter starts retracting, before increasing fuel (and nitrogen) to test flow rates
stabilizationTime2Sec	4			time (in seconds) to wait after ignitionToTestRampTimeSec, before the fiber moves into test position (fiberTestPosition)
fuelBottleIgnitionFlowRateN2Slpm	1.2	must be less than or equal to the fuel mass flow controller installed		initial fuel bottle flow rate (SLPM N2 basis) through stabilizationTime1Sec
nitrogenIgnitionFlowRateN2Slpm	0	must be less than or equal to the bypass mass flow controller installed		initial nitrogen flow rate (SLPM N2 basis) through stabilizationTime1Sec
fuelBottleTestFlowRateN2Slpm	1.2	must be less than or equal to the fuel mass flow controller installed		fuel bottle flow rate (SLPM N2 basis) after ignitionToTestRampTimeSec through the end of constantFlowTimeSec
nitrogenTestFlowRateN2Slpm	0	must be less than or equal to the bypass mass flow controller installed		nitrogen flow rate (SLPM N2 basis) after ignitionToTestRampTimeSec through the end of constantFlowTimeSec
ignitionToTestRampTimeSec	5	if ramping from IgnitionFlowRate to TestFlowRate, minimum value is 1; if flow rates are the same, value is 0	if fuelBottleIgnitionFlowRateN2Slpm and fuelBottleTestFlowRateN2Slpm are the same AND nitrogenIgnitionFlowRateN2Slpm and nitrogenTestFlowRateN2Slpm are the same, then this time is skipped	time (in seconds) it takes to ramp from fuelBottleIgnitionFlowRateN2Slpm to fuelBottleTestFlowRateN2Slpm and nitrogenIgnitionFlowRateN2Slpm to nitrogenTestFlowRateN2Slpm after stabilizationTime1Sec
constantFlowTimeSec	30	effectively whole second resolution (parameter can be decimal but script only checks timing once per second)	if using fiber and fiber movement, this time starts after fiber movement start; if using fiber but not fiber movement, this time starts after fiber starts moving into position; if not using fiber, this time starts after stabilizationTime2Sec	time (in seconds) to wait at a constant flow before continuing script

numberOfRampHolds	0			number of times gas flow will ramp and hold following constantFlowTimeSec
rampSizePercent	-20	positive or negative value	numberOfRampHolds must be greater than 0 for this value to be used, use default when numberOfRampHolds is 0	percentage amount the flow rate changes the per ramp, based on fuelBottleTestFlowRateN2Slpm and nitrogenTestFlowRateN2Slpm
rampDurationSec	2	tenth of a second resolution; minimum value is 1	numberOfRampHolds must be greater than 0 for this value to be used, use default when numberOfRampHolds is 0	time (in seconds) to ramp to next flow rate
holdDurationSec	10		numberOfRampHolds must be greater than 0 for this value to be used, use default when numberOfRampHolds is 0	time (in seconds) to hold at the flow rate after each ramp
temperatureLimitCriticalC	300		if any (useCenterThermocouple, useOffsetThermocuople, useCenterFluxThermocouple, useOffsetFluxThermocouple) parameter marked true is over the limit, takes action	temperature limit (in degrees C) that ends the test point (stops all flows; script still performs post-flame data and imaging collection, and then closes the test point nicely)
temperatureLimitC	250		if any (useCenterThermocouple, useOffsetThermocuople, useCenterFluxThermocouple, useOffsetFluxThermocouple) parameter marked true is over the limit, takes action	temperature limit (in degrees C) that ends the constantFlowTimeSec and causes the script to moves on to ramping
useCenterThermocouple	true	true or false		indicates if Center Thermocouple will be used in temperature limit checks
useOffsetThermocouple	true	true or false		indicates if Offset Thermocouple will be used in temperature limit checks
useCenterFluxThermocouple	true	true or false		indicates if Center Flux Thermocouple will be used in temperature limit checks
useOffsetFluxThermocouple	true	true or false		indicates if Offset Flux Thermocouple will be used in temperature limit checks
preflowFlowDurationSecs	0	if using preflow, must be greater than 5; if not using preflow, value is 0		time in seconds to flow from fuel bottle and/or nitrogen prior to starting gas flow for ignition

preflowFuelRateSlpm	0	must be less than or equal to the fuel mass flow controller installed	preflowFlowDurationSecs must be greater than 0 for this value to be used, use default when preflowFlowDurationSecs is 0	fuel bottle flow rate (SLPM N2 basis) during preflowDurationSecs
preflowNitrogenSlpm	0	must be less than or equal to the bypass mass flow controller installed	preflowFlowDurationSecs must be greater than 0 for this value to be used, use default when preflowFlowDurationSecs is 0	nitrogen flow rate (SLPM N2 basis) during preflowDurationSecs
preflowWaitDurationSecs	300	if using preflow, must be greater than 50	preflowFlowDurationSecs must be greater than 0 for this value to be used, use default when preflowFlowDurationSecs is 0	time in seconds to wait after preflowFlowDurationSecs is complete before starting gas flow for ignition

Appendix E: Results obtained from Methane-Nitrogen

Methane was used for some of the tests aboard the ISS and with the 25 mm burner. All flames self-extinguished within 45 seconds.

Table E.1. Test results obtained from Methane-Nitrogen mixture and 25 mm burner

	Δh_c	X_{O2} Bef test	X_{O2} After test	p	$\dot{m}''$	Osc Time	Ext Time	End cond	$\dot{q}''_{CTR}$	$\dot{q}''_{off}$	T_s	Calorimeter	Xr	h_f
test ID	kJ/g			bar	g/m^2-s	s	s		kW/m^2	kW/m^2	^{0}C	kW/m^2		mm
20279B7	50	0.36	0.35	1.06	5.98	7.70	14.93	SE	5.00	3.90	47.90	9.60	x	30.40
20279B5	50	0.37	0.37	1.06	4.98	7.80	42.30	SE	6.00	4.40	59.00	6.30	x	25.53
20279B8	50	0.35	0.35	1.06	4.49	9.43	42.70	SE	5.80	4.40	60.00	6.70	x	29.76
20279B6	50	0.37	0.36	1.05	3.98	7.83	18.43	SE	7.70	5.10	53.50	10.00	x	22.83
20279A2	50	0.39	0.39	1.05	2.97	15.13	23.43	SE	8.25	6.36			0.53	20.98
20279B4	50	0.38	0.37	1.05	2.46	17.17	24.10	SE	9.00	6.00	61.00	10.80	0.52	19.17
20279B1	50	0.39	0.38	1.05	1.97	22.47	25.60	SE	10.80	8.40	63.00	10.50	0.50	14.81
20279B2	50	0.38	0.38	1.05	1.76	27.23	30.60	SE	10.60	8.22	64.00	9.80	-	14.39
20339L3	35	0.37	0.36	1.06	7.92	6.76	8.13	SE	3.99	3.44	45.00	10.30	x	26.47
20339L2	35	0.37	0.37	1.06	5.22	8.73	13.23	SE	6.34	4.77	52.00	10.90	x	21.35
20339A0	35	0.38	0.37	1.06	4.24	13.28	13.51	SE	8.40	6.47	56.40	11.06	0.41	18.37
20339L1	35	0.37	0.37	1.06	3.49	14.50	17.27	SE	8.38	6.44	56.90	10.60	0.55	19.80
20339A3	25	0.39	0.39	1.05	11.90	7.20	10.87	SE	4.20	3.01	46.00	9.10	x	28.16
20339A7	25	0.38	0.38	1.06	10.41	6.71	11.48	SE	4.30	3.50	46.20	9.80	x	
20339A4	25	0.39	0.39	1.06	8.94	7.50	15.00	SE	3.63	3.30	51.00	9.80	x	22.33
20339A6	25	0.39	0.38	1.06	7.46	9.23	23.10	SE	5.23	4.70	56.10	9.50	x	21.35
20339A8	25	0.38	0.38	1.06	6.42	10.87	24.27	SE	6.30	5.00	53.00	10.40	0.51	18.26
20339A9	25	0.38	0.38	1.06	6.40	18.53	25.30	SE	4.40	4.30	60.00	9.83	0.47	20.37
20339A2	25	0.40	0.39	1.05	5.96	16.33	19.20	SE	6.75	5.80	54.70	9.90	0.35	17.63
20279D4	50	0.34	0.33	1.04	5.97	6.23	7.30	SE	4.40	3.50	41.00	10.90	x	27.41
20279D3	50	0.34	0.34	1.04	5.00	7.70	9.73	SE	5.30	3.60	43.70	9.80	x	28.39
20279D7	50	0.33	0.25	1.04	4.49	6.53	9.10	SE	5.95	4.00	44.00	9.80	x	25.90
20279D2	50	0.34	0.34	1.04	3.98	6.93	10.63	SE	6.40	4.00	46.65	10.00	x	24.56
20279D1	50	0.35	0.34	1.04	2.97	8.43	11.37	SE	7.60	5.00	48.50	11.70	x	21.15
20279D6	50	0.33	0.33	1.04	2.46	11.10	13.37	SE	8.25	5.75	49.25	12.00	0.51	18.33
20279D5	50	0.33	0.33	1.04	1.97	14.93	16.47	SE	9.47	6.00	53.00	10.80	x	16.01
20279J6	50	0.24	0.40	1.04	3.98	6.97	21.43	SE	2.50	2.40	41.80	4.30	x	
20279J1	50	0.25	0.25	1.03	1.99	6.10	6.67	SE	6.61	4.50	36.00	10.00	0.37	17.36
20279J2	50	0.25	0.25	1.03	1.76	5.87	5.87	SE	7.00	4.50	36.00	9.98	0.35	14.92
20339J3	25	0.25	0.25	1.04	5.86	5.44	5.50	SE	3.40	3.20	36.00	8.15	0.25	20.93

Appendix F: Results obtained by the 50 mm burner and Ethylene-Nitrogen mixture

Part of the BRE experiments aboard the ISS was performed by using the 50 mm burner and Ethylene Nitrogen mixture. There were several tests that burned for the entire duration of the test but with oscillations started before fuel termination.

Table F.1. Test results obtained by the 50 mm burner and ethylene-nitrogen mixture.

	Δh_c	X_{O2} Bef. test	X_{O2} After test	p	$\dot{m}''$	Osc Time	Ext Time	End cond	$\dot{q}''_{CTR}$	$\dot{q}''_{off}$	T_s	Calorimeter	Xr	h_f
test ID	kJ/g			bar	g/m^2-s	s	s		kW/m^2	kW/m^2	^{0}C	kW/m^2		mm
20247A1	47.20	0.40	0.38	1.07	1.51	24.90	150.93	FTO			79.04	10.60	-	39.73
20247C1	47.20	0.37	0.35	1.08	1.49	24.07	77.60	FTO			73.80	11.35	-	37.35
20247B1	47.20	0.38	0.37	1.07	1.07	36.83	95.47	FTO			81.00	12.70	-	30.53
21028B1	23.60	0.38	0.36	1.07	3.00	20.93	76.83	FTO	2.90	1.10	67.50	9.20	-	
21028C1	23.70	0.39	0.38	1.07	2.98	32.30	91.30	FTO	2.70	1.50	71.30	10.50	-	
21028B2	15.60	0.36	0.35	1.07	2.98	26.67	74.93	FTO	2.80	1.30	67.00	9.30	-	
20247D1	47.20	0.35	0.34	1.06	1.50	36.80	74.97	FTO	5.20	3.00	71.50	10.30	-	37.69
20247G1	47.20	0.32	0.31	1.07	1.49	25.37	63.67	SE	4.90	2.90	65.30	8.62	-	41.88
20247P1	47.20	0.31	0.30	1.07	1.49	23.50	60.50	SE	4.72	2.52	64.04	8.60	-	42.19
20247F1	47.20	0.33	0.32	1.08	1.48	28.30	124.13	FTO	5.20	2.90	71.63	7.70	-	35.57
20247L2	47.20	0.35	0.34	1.08	1.48	38.60	136.97	FTO	5.50	3.25	72.70	11.07	-	34.46
21028D5	47.20	0.31	0.30	1.07	1.24	24.97	52.67	SE	3.30	1.70	63.00	9.10	-	35.08
21028D4	36.00	0.32	0.31	1.06	1.73	25.50	49.53	SE	2.90	1.70	59.70	9.30	-	30.61
21028D3	31.30	0.33	0.32	1.06	1.98	25.37	48.40	SE	2.70	1.60	60.00	9.10	-	33.73
21028D2	23.60	0.34	0.33	1.06	2.48	22.43	49.40	SE	3.30	1.70	59.00	8.50	-	37.86
20247N1	23.00	0.34	0.33	1.08	2.05	15.37	62.77	SE	5.60	3.30	64.55	10.40	-	28.81
20247M1	23.00	0.34	0.33	1.06	2.05	33.60	132.40	FTO	4.80	3.10	75.20	8.45	-	28.40
21028D1	15.60	0.35	0.34	1.05	2.98	25.37	65.33	SE	4.00	2.10	60.00	9.60	-	31.20
20247H2	47.20	0.27	0.26	1.07	1.50	17.23	40.53	SE	3.90	2.03	51.66	8.49	-	41.06
20247J1	47.20	0.26	0.26	1.05	1.49	11.57	20.80	SE	4.20	2.30	48.40	8.00	-	35.86
20247K1	47.20	0.26	0.25	1.05	1.49	12.13	21.53	SE	3.90	2.26	48.20	8.30	-	34.33
21028G4	47.20	0.24	0.24	1.05	1.24	12.63	18.60	SE	4.30	2.50	41.60	9.00	-	28.33
21028G1	15.60	0.24	0.24	1.04	2.98	9.63	18.07	SE	2.83	1.43	39.20	7.20	-	32.04
21028G5	15.40	0.24	0.23	1.05	1.97	10.13	17.30	SE	3.90	2.10	38.30	8.30	0.48	21.42

The radiative loss fraction was calculated using the correlation introduced in [52,60]. It was used along with the Eq. (6.17) to estimate the flame temperature and determine if these flames could reach steady state. It was shown that all flame temperatures were below the critical temperature range of 1100 K to 1200 K.

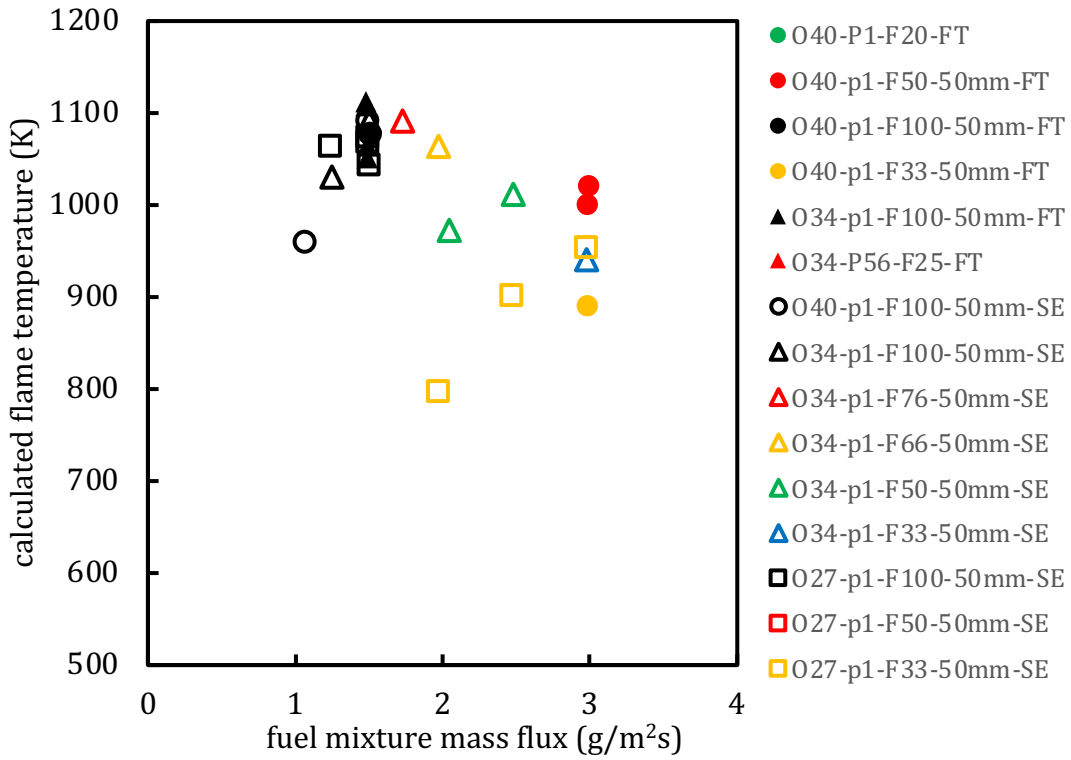

Figure F.1. Preliminary examination of calculated flame temperatures obtained by the 50 mm burner

Bibliography

[1] Ross HD Editor and Gollahalli SR Reviewer, Microgravity Combustion: Fire in Free Fall, Applied Mechanics Reviews, 55(6), 2002, pp. B116–B117.

[2] B. Burrough, Dragonfly: NASA and the Crisis Aboard the MIR. Harper Collins.

[3] J.M. Linenger, Off the Planet: Surviving Five Perilous Months Aboard the Space Station Mir. McGraw-Hill, 2000.

[4] Markan, A., Development and Analysis of a Burning Rate Emulator (BRE) for Study in Microgravity, PhD Thesis, UMCP.

[5] Sacksteder, K. R., Greenberg, P. S., Pettegrew, R. D., Tien, J. S., Ferkul, P. V., and Shih, H.-Y., Forced Flow Flame Spreading Test: Preliminary Findings From the USMP-3 Shuttle Mission, Third United States Microgravity Payload: One Year Report"; p. 83-96; NASA/CP-1998-207891, Washington D.C.

[6] P.V. Ferkul, S.L. Olson, M.C. Johnston, and J.S. T'ien., Flammability Aspects of Fabric in Opposed and Concurrent Air Flow in Microgravity. In 8th US National Combustion Meeting, 8 Th U. S. National Combustion Meeting Organized by the Western States Section of the Combustion Institute, pp. 19–22.

[7] J.H. Kimzey, Skylab Results: Proceedings of the 3rd Space Processing Symposium, Vol. 1. Technical Report, NASA TM-X-70752: Marshall Space Flight Center.

[8] Ivanov, A. V., Balashov, Y. V., Andreeva, T. V., and Melikhov, A. S., Experimental Verification of Material Flammability in Space.

[9] Bhattacharjee, S., and Altenkirch, R. A., Radiation-Controlled, Opposed-Flow Flame Spread in a Microgravity Environment, Symposium (International) on Combustion, 23(1), 1991, pp. 1627–1633.

[10] Markan, A., Sunderland, P. B., Quintiere, J. G., de Ris, J. L., Stocker, D. P., and Baum, H. R., A Burning Rate Emulator (BRE) for Study of Condensed Fuel Burning in Microgravity, Combustion and Flame, 192, 2018, pp. 272–282.

[11] Sacksteder, K. R., Greenberg, P. S., Pettegrew, R. D., Tien, J. S., Ferkul, P. V., and Shih, H.-Y., Forced Flow Flame Spreading Test: Preliminary Findings From the USMP-3 Shuttle Mission, Washington D.C.

[12] Jomaas, G., Torero, J. L., Eigenbrod, C., Niehaus, J., Olson, S. L., Ferkul, P. V., Legros, G., Fernandez-Pello, A. C., Cowlard, A. J., Rouvreau, S., Smirnov, N., Fujita, O., T′ien, J. S., Ruff, G. A., and Urban, D. L., Fire Safety in Space – beyond Flammability Testing of Small Samples, Acta Astronautica, 109, 2015, pp. 208–216.

[13] T'ien, J. S., The Possibility of a Reversal of Material Flammability Ranking from Normal Gravity to Microgravity, Combustion and Flame, 80(3), 1990, pp. 355–357.

[14] Matalon, M., and Law, C. K., Gas-Phase Transient Diffusion in Droplet Vaporization and Combustion, Combustion and Flame, 59(2), 1985, pp. 213–215.

[15] FERNANDEZ-PELLO, A. C., and HIRANO, T., Controlling Mechanisms of Flame Spread, Combustion Science and Technology, 32(1–4), 1983, pp. 1–31.

[16] Ferkul, P., Urban, D. L., Olson, S., Ruff, G. A., Easton, J., T'ien, J. S., Liao, Y.-T. T., Fernandez-Pello, A. C., Torero, J. L., and Legros, G., The Saffire Experiment: Large-Scale

Combustion Aboard Spacecraft, 10th US National Combustion Meeting, Combustion Institute.
[17] Link, S., Huang, X., Olson, S., Ferkul, P., and Fernandez-Pello, C., The Effect of Gravity on Flame Spread over PMMA Cylinders in Opposed Flow with Variable Oxygen Concentration., 46th International Conference on Environmental Systems.
[18] Osorio, A. F., Mizutani, K., Fernandez-Pello, C., and Fujita, O., Microgravity Flammability Limits of ETFE Insulated Wires Exposed to External Radiation, Proceedings of the Combustion Institute, 35(3), 2015, pp. 2683–2689.
[19] Fernandez-Pello, A. C., Ray, S. R., and Glassman, I., Flame Spread in an Opposed Forced Flow: The Effect of Ambient Oxygen Concentration, Symposium (International) on Combustion, 18(1), 1981, pp. 579–589.
[20] Torero, J. L., and Fernandez-Pello, A. C., Forward Smolder of Polyurethane Foam in a Forced Air Flow, Combustion and Flame, 106(1), 1996, pp. 89–109.
[21] Fernandez-Pello, A., and Williams, F. A., Laminar Flame Spread over PMMA Surfaces, Symposium (International) on Combustion, 15(1), 1975, pp. 217–231.
[22] Dosanjh, S. S., Pagni, P. J., and Fernandez-Pello, A. C., Forced Cocurrent Smoldering Combustion, Combustion and Flame, 68(2), 1987, pp. 131–142.
[23] Fernandez—Pello, A. C., Flame Spread Modeling, Combustion Science and Technology, 39(1–6), 1984, pp. 119–134.
[24] Thomsen, M., Carmignani, L., Rodriguez, A., Scudiere, C., Liveretou, C., Fernandez-Pello, C., Gollner, M., Olson, S., and Ferkul, P., Downward Flame Spread Rate Over PMMA Rods Under External Radiant Heating, Fire Technology, 2022.
[25] Xiong, C., Fan, H., Huang, X., and Fernandez-Pello, C., Evaluation of Burning Rate in Microgravity Based on the Fuel Regression, Flame Area, and Spread Rate, Combustion and Flame, 237, 2022, p. 111846.
[26] Thomsen, M., Fernandez-Pello, C., Olson, S. L., and Ferkul, P. V., Downward Burning of PMMA Cylinders: The Effect of Pressure and Oxygen, Proceedings of the Combustion Institute, 38(3), 2021, pp. 4837–4844.
[27] Thomsen, M., Fernandez-Pello, C., Huang, X., Olson, S., and Ferkul, P., Buoyancy Effect on Downward Flame Spread Over PMMA Cylinders, Fire Technology, 56(1), 2020, pp. 247–269.
[28] Urban, D. L., Ferkul, P., Olson, S., Ruff, G. A., Easton, J., T'ien, J. S., Liao, Y.-T. T., Li, C., Fernandez-Pello, C., Torero, J. L., Legros, G., Eigenbrod, C., Smirnov, N., Fujita, O., Rouvreau, S., Toth, B., and Jomaas, G., Flame Spread: Effects of Microgravity and Scale, Combustion and Flame, 199, 2019, pp. 168–182.
[29] Thomsen, M., Fernandez-Pello, C., Urban, D., Ruff, G., and Olson, S., Upward Flame Spread over a Thin Composite Fabric: The Effect of Pressure and Microgravity, 48th International Conference on Environmental Systems.
[30] Link, S., Huang, X., Fernandez-Pello, C., Olson, S., and Ferkul, P., The Effect of Gravity on Flame Spread over PMMA Cylinders, Scientific Reports, 8(1), 2018, p. 120.
[31] Olson, S. L., Ferkul, P. V., and T'ien, J. S., Near-Limit Flame Spread over a Thin Solid Fuel in Microgravity, Symposium (International) on Combustion, 22(1), 1989, pp. 1213–1222.

[32] Olson, S. L., Kashiwagi, T., Fujita, O., Kikuchi, M., and Ito, K., Experimental Observations of Spot Radiative Ignition and Subsequent Three-Dimensional Flame Spread over Thin Cellulose Fuels, Combustion and Flame, 125(1–2), 2001, pp. 852–864.
[33] Thomsen, M., Fernandez-Pello, C., Urban, D. L., Ruff, G. A., and Olson, S. L., On Simulating Concurrent Flame Spread in Reduced Gravity by Reducing Ambient Pressure, Proceedings of the Combustion Institute, 37(3), 2019, pp. 3793–3800.
[34] Dietrich, D., Ross, H., and T'ien, J., Candle Flames in Non-Buoyant and Weakly Buoyant Atmospheres, 32nd Aerospace Sciences Meeting and Exhibit, American Institute of Aeronautics and Astronautics.
[35] DIETRICH, D. L., ROSS, H. D., SHU, Y., CHANG, P., and T'IEN, J. S., Candle Flames in Non-Buoyant Atmospheres, Combustion Science and Technology, 156(1), 2000, pp. 1–24.
[36] Matalon, M., and Law, C. K., Gas-Phase Transient Diffusion in Droplet Vaporization and Combustion, Combustion and Flame, 59(2), 1985, pp. 213–215.
[37] Nayagam V, Microgravity N-Heptane Droplet Combustion in Oxygen-Helium Mixtures at Atmospheric Pressure, AIAA Journal, 36(8), 1998, p. 1369.
[38] Nayagam, V., Dietrich, D. L., Ferkul, P. V, Hicks, M. C., and Williams, F. A., Can Cool Flames Support Quasi-Steady Alkane Droplet Burning?, Combustion and Flame, 159(12), 2012, pp. 3583–3588.
[39] Nayagam, V., Dietrich, D. L., Hicks, M. C., and Williams, F. A., Cool-Flame Extinction during n-Alkane Droplet Combustion in Microgravity, Combustion and Flame, 162(5), 2015, pp. 2140–2147.
[40] Nayagam, V., Dietrich, D. L., Hicks, M. C., and Williams, F. A., Radiative Extinction of Large N-Alkane Droplets in Oxygen-Inert Mixtures in Microgravity, Combustion and Flame, 194, 2018, pp. 107–114.
[41] Kumagai, S., Sakai, T., and Okajima, S., Combustion of Free Fuel Droplets in a Freely Falling Chamber, Symposium (International) on Combustion, 13(1), 1971, pp. 779–785.
[42] Hajilou, M., Brown, M. Q., Brown, M. C., and Belmont, E., Investigation of the Structure and Propagation Speeds of N-Heptane Cool Flames, Combustion and Flame, 208, 2019, pp. 99–109.
[43] Hajilou, M., and Belmont, E., Characterization of Ozone-Enhanced Propane Cool Flames at Sub-Atmospheric Pressures, Combustion and Flame, 196, 2018, pp. 416–423.
[44] NASA-STD-6001B. Flammability, Offgassing, and Compatibility Requirements and Test Procedures.
[45] ISO, I. S. O., 5660-1:" Reaction-to-Fire Tests-Heat Release, Smoke Production and Mass Loss Rate-Part 1:(Cone Calorimeter Method)", International Organization for Standardization, International Standard Organization, 2002.
[46] Zhang, Y., Kim, M., Guo, H., Sunderland, P. B., Quintiere, J. G., deRis, J., and Stocker, D. P., Emulation of Condensed Fuel Flames with Gases in Microgravity, Combustion and Flame, 162(10), 2015, pp. 3449–3455.
[47] Zhang, Y., Kim, M., Sunderland, P. B., Quintiere, J. G., and de Ris, J., A Burner to Emulate Condensed Phase Fuels, Experimental Thermal and Fluid Science, 73, 2016, pp. 87–93.
[48] Markan, A., Sunderland, P. B., Quintiere, J. G., de Ris, J. L., and Baum, H. R., Measuring Heat Flux to a Porous Burner in Microgravity, Proceedings of the Combustion Institute, 37(3), 2019, pp. 4137–4144.

[49] Markan, A., Baum, H. R., Sunderland, P. B., Quintiere, J. G., and de Ris, J. L., Transient Ellipsoidal Combustion Model for a Porous Burner in Microgravity, Combustion and Flame, 212, 2020, pp. 93–106.
[50] Snegirev, A., Kuznetsov, E., Markus, E., Dehghani, P., and Sunderland, P., Transient Dynamics of Radiative Extinction in Low-Momentum Microgravity Diffusion Flames, Proceedings of the Combustion Institute, 38(3), 2021, pp. 4815–4823.
[51] Dehghani, P., Sunderland, P. B., Quintiere, J. G., and deRis, J. L., Burning in Microgravity: Experimental Results and Analysis, Combustion and Flame, 228, 2021, pp. 315–330.
[52] Dehghani, P., and Quintiere, J. G., Theoretical Analysis and Predictions of Burning in Microgravity Using a Burning Emulator, Combustion and Flame, 233, 2021, p. 111572.
[53] Dehghani, P. and Peter B. Sunderland, Burning Emulation in Microgravity: Experimental Results and Analysis, ASGSR.
[54] Dehghani, P., Auth, E., Cui, C., Stocker, D. P., de Ris, J. L., Sunderland, P. B., and Quintiere, J. G., Microgravity Observations of a Burnig Emulator to Investigate Material Flammability, ESSCI, Columbia.
[55] Auth, E., Using a Burning Rate Emulator (BRE) to Emulate Condensed Fuels and Study Pool Fire Behaviour in 1g, M. Sc. Thesis, University of Maryland.
[56] Auth, E., Quintiere, J. G., and Sunderland, P. B., Emulation of Condensed Fuel Flames with Gaseous Fuels Supplied through a Porous Copper Calorimeter, Fire and Materials, 44(7), 2020, pp. 935–942.
[57] Kuznetsov, E. A., Snegirev, A. Yu., and Markus, E. S., Radiative Extinction of Laminar Diffusion Flame above the Flat Porous Burner in Microgravity: A Computational Study, Combustion, Explosion, and Shock Waves, 56(4), 2020, pp. 394–411.
[58] Grosshandler, W., RadCal: A Narrow Band Model for Radiation Calculations in a Combustion Environment, NIST Technical Note 1402, National Institute of Standards and Technology136, Gaithersburg, Maryland.
[59] Vivien R. Lecoustre, RadCal Improvements to the Narrow-Band Model for Radiation Calculations in a Combustion Environment, NIST Special Publication 1402, 2nd ed., Gaithersburg, Maryland.
[60] Dehghani, P., Quintiere, J. G., and de Ris, J., Burning Emulation of Solids and Liquids in Microgravity, Proc. Combust. Inst., 2022.
[61] Kim, H., Procedures to Obtain Accurate Measurement from a Gas Fueled Burner.
[62] Stephen J. Lawn, ACME-RPT-012: Advanced Combustion via Microgravity Experiments (ACME) BRE Radiometer Characterization Report.
[63] Michael W. Medved, ACME-DOC-010 Rev D: Advanced Combustion via Microgravity Experiments (ACME) Software Interface Design Description Contract NNC09BA02B, DO-110.
[64] TELEDYNE HASTINGS INSTRUMENTS INSTRUCTION MANUAL HFM-300 FLOW METER, HFC-302 FLOW CONTROLLER Document Number 151-032015.
[65] McPherson, K., Hrovat, K., Kelly, E., and Keller, J., A Researcher's Guide To International Space Station Acceleration Environment.
[66] DiNenno, P. J., Association, N. F. P., and Engineers, S. of F. P., SFPE Handbook of Fire Protection Engineering, National Fire Protection Association.
[67] Quintiere, J. G., Fundamentals of Fire Phenomena, John Wiley.

[68] Quintiere, J. G., Principles of Fire Behavior, CRC Press.
[69] Advanced Combustion via Microgravity Experiments Integrated Science Requirements.
[70] Ban, H., Venkatesh, S., and Saito, K., Convection-Diffusion Controlled Laminar Micro Flames, 1994.
[71] ACME-RPT-0013- PMT Characterization Report Rev. - October 2016.
[72] R. Siegel, and J. R. Howell, Thermal Radiation Heat Transfer, Hemisphere, New York.
[73] M. Q. Brewster, Thermal Radiative Transfer and Properties, Wiley, New York.
[74] Tewarson, A., Generation of Heat and Chemical Compounds in Fires," The SFPE Handbook of Fire Protection Engineering (3rd Ed), National Fire Protection Association, Quincy, MA.
[75] Vermina Plathner, F., Quintiere, J. G., and van Hees, P., Analysis of Extinction and Sustained Ignition, Fire Safety Journal, 105, 2019, pp. 51–61.
[76] Lundström, F. V., Sunderland, P. B., Quintiere, J. G., van Hees, P., and de Ris, J. L., Study of Ignition and Extinction of Small-Scale Fires in Experiments with an Emulating Gas Burner, Fire Safety Journal, 87, 2017, pp. 18–24.
[77] ISO 5660-1:2015 Reaction-to-Fire Tests — Heat Release, Smoke Production and Mass Loss Rate — Part 1: Heat Release Rate (Cone Calorimeter Method) and Smoke Production Rate (Dynamic Measurement).
[78] ISO 5660-1:2015/AMD 1:2019 Reaction-to-Fire Tests — Heat Release, Smoke Production and Mass Loss Rate — Part 1: Heat Release Rate (Cone Calorimeter Method) and Smoke Production Rate (Dynamic Measurement) — Amendment 1.
[79] Jiang, F., Qi, H., de Ris, J. L., and Khan, M. M., Radiation Enhanced B-Number, Combustion and Flame, 160(8), 2013, pp. 1510–1518.
[80] Perry, R. H., Green, D. W., and Maloney, J. O., Perry's Chemical Engineers' Handbook, McGraw-Hill, New York.
[81] Lide, D. R., Handbook of Chemistry and Physics, CRC Press, Boca Raton.
[82] Howell, J. R., Menguc, M. P., and Siegel, R., Thermal Radiation Heat Transfer, CRC press.
[83] Modest, M., Radiative Heat Transfer.
[84] de Ris, J., Fire Radiation—A Review, Symposium (International) on Combustion, 17(1), 1979, pp. 1003–1016.
[85] Yu. Snegirev, A., Perfectly Stirred Reactor Model to Evaluate Extinction of Diffusion Flame, Combustion and Flame, 162(10), 2015, pp. 3622–3631.
[86] Irace, P. H., Lee, H. J., Waddell, K., Tan, L., Stocker, D. P., Sunderland, P. B., and Axelbaum, R. L., Observations of Long Duration Microgravity Spherical Diffusion Flames Aboard the International Space Station, Combustion and Flame, 229, 2021, p. 111373.
[87] Tang, S., Im, H. G., and Atreya, A., A Computational Study of Spherical Diffusion Flames in Microgravity with Gas Radiation. Part II: Parametric Studies of the Diluent Effects on Flame Extinction, Combustion and Flame, 157(1), 2010, pp. 127–136.
[88] Santa, K. J., Chao, B. H., Sunderland, P. B., Urban, D. L., Stocker, D. P., and Axelbaum, R. L., Radiative Extinction of Gaseous Spherical Diffusion Flames in Microgravity, Combustion and Flame, 151(4), 2007, pp. 665–675.
[89] Lecoustre, V. R., Sunderland, P. B., Chao, B. H., and Axelbaum, R. L., Numerical Investigation of Spherical Diffusion Flames at Their Sooting Limits, Combustion and Flame, 159(1), 2012, pp. 194–199.

[90] Lecoustre, V., Narayanan, P., Baum, H., and Trouve, A., Local Extinction of Diffusion Flames in Fires, Fire Safety Science, 10, 2011, pp. 583–595.
[91] Narayanan, P., Baum, H. R., and Trouvé, A., Effect of Soot Addition on Extinction Limits of Luminous Laminar Counterflow Diffusion Flames, Proceedings of the Combustion Institute, 33(2), 2011, pp. 2539–2546.
[92] Science Requirements Document for Burning Rate Emulator (BRE): Material Burning and Extinction in Microgravity Version 2.11.
[93] Kline, S. J., Describing Uncertainty in Single Sample Experiments, Mech. Engineering, 75, 1953, pp. 3–8.
[94] Moffat, R. J., Using Uncertainty Analysis in the Planning of an Experiment, 1985.
[95] Lyon, R. E., and Quintiere, J. G., Criteria for Piloted Ignition of Combustible Solids, Combustion and Flame, 151(4), 2007, pp. 551–559.